Design and Control of a Micro Ultrasonic Motor-Based Insect-Scale Robot for Inspection Purposes

(検査を目的としたマイクロ超音波モータベースの
インセクトスケールロボットの設計と制御)

July, 2023

Doctor of Philosophy (Engineering)

Mohamed Mostafa Abdelaziem Khalil
モハメッド モスタファ アブデラジエム キャリル

Toyohashi University of Technology

Declaration

This thesis is submitted as a partial fulfillment of the Doctor of Philosophy degree (Ph.D.) in Mechanical Engineering at Toyohashi University of Technology.

I hereby certify that the content of this thesis is original and that I carried out all of the research work included. I also certify that no part of the thesis has been submitted for a degree or a qualification at any other scientific entity.

Mohamed Mostafa Abdelaziem Khalil
Date: July, 2023

Acknowledgment

I would like to thank my supervisors Prof. Tomoaki Mashimo and Prof. Kotaro Takayama for their continuous and endless support in every moment of my research journey, their encouragement and precious help were always a motivation for me in my studies. I could not imagine having better advisors and mentors for completing my research and education.

I would also like to thank Prof. Naoki Uchiyama and Prof. Kentaro Takagi for their helpful comments and remarks on my thesis in the examination stage.

I am also very grateful to all of my lab staff; Prof. Takuma Akiduki, Prof. Toda, and Oba-san, their help in my research studies is very appreciated.

I would like to thank all of my lab members and ex-lab members for their help and joyful moments every day. You treat me all as one of your family members and I will never forget that ever in my life. A special greeting for Yoga, Eric, Izuhara, Iwama, Fujimura, Baba, Kikuchi, Masuda, and Ito.

I would also like to thank all of my family members for their endless support during my research in Japan.

To my lovely wife, my daughter, and my newly born son, your presence in my life means a lot to me, thank you for being always there whenever needed.

To my beloved father, we started this trip together but you left me suddenly one day, I just wish you are here now with me, I am sure you would be the happiest and proudest man as you were always in all of my previous life steps. I miss you !!

Abstract

The inspection and monitoring of industrial sites, machines, and infrastructure are important issues for their sustainability and further maintenance. Although these tasks are repetitive and time-consuming, and some of these environments may be characterized by dust, humidity, or the absence of natural light, the classical approach relies on large human activities. A major problem always exists in civil structures and industrial sites is that they are rarely uniform in shape and are not typically designed with considerations for easy inspection access. The same problem is associated with machines, where inspection of complicated machines like turbine engines requires the disassembly of a lot of components which can be costly and time-consuming. Automatic or robotic solutions can be considered useful tools for inspection because they can be effective in exploring dangerous or inaccessible sites, at a relatively low-cost and reducing the time required for the relief. An intelligent bionic robot device also increases working safety if operated at high-elevated sites while performing some dangerous operations instead of inspection personnel.

A common element that exists in all industrial sites, civil structures, and machines is the countless number of tubes and pipelines to transport all kinds of fluidic materials, such as water, petroleum, natural gas, and oxygen. We consider these tubes and pipelines as direct routes to the core of an inspection site or a complicated machine. We currently take advantage of these pipes and tubes to explore inaccessible structures and the core of complicated machines by the borescopes. Although it provides crucial information, it is extrinsically manually actuated by an operator which makes it hard to point it to a specific spot. One of the main reasons is the absence of a powerful actuator in a micro-scale to be fitted in the borescope tip. It is time to think then of the next generation of borescope as a miniature robot intrinsically actuated and capable of navigating inside narrow tubes and pipelines efficiently. We think that a combination of a miniature robot with high accessibility features can result in incredible capabilities for locomotion and manipulation in complex inspection tasks. This thesis introduces the concept of an insect-scale robot that is inspired by biological creatures for inspection purposes. This research addresses different challenges of scaling down robots, that require the significant integration of component technologies such as actuators, fabrication techniques, and sensing machines.

The first challenge is the driving mechanism, downsizing an actuator to a micro size comes with a lot of problems. For example, electromagnetic actuators that dominate at the macro-scale diminish their power at the micro-scale due to their scaling law. Furthermore, several technical manufacturing problems are involved in miniaturizing the components, such as coils, permanent magnets, and bearings. Instead, piezoelectric ultrasonic motors perform at such a scale as the most prominent microactuator because of their high-power density and good machinability. However, despite their great scalability, they have obvious nonlinear and time-varying characteristics that deteriorate their performance in prolonged operations. We investigated that problem by studying the effectiveness of the motor's internal parameter changes, such as a temperature rise and the resonant frequency variation. For that, a mathematical model was derived from scratch to model the non-linear temperature-dependent characteristics of ultrasonic motors followed by several experiments to verify the hypothesis experimentally. The model and the experiments confirmed that the internal losses of the motor could rises the temperature of the motor which results in some deviation in the motor's parameters such as the natural frequency. The experiments also prove that such deviation affected the motor performance by enlarging its steady-state error with time. To solve this dilemma, we introduced a model-free, real-time-adaptive extremum-seeking controller (ESC) that can coop with the non-linear characteristics of the motor. To build the control structure, we constructed the smallest rotary actuator-sensor system in the world that consists of a micro-ultrasonic motor, a tiny tunneling magneto resistance (TMR) sensor, and a tiny magnet. The resulting system was assembled into a size with a height of 3.2 mm, a width of 3.2 mm, and a length of 5 mm. Several experiments that involve constant and variable speed commands show that the controller succeeded to drive the motor at the desired angular velocity with a minimum steady-state error by continuously tracking and localizing the optimum driving frequency.

The second challenge is the design itself of the robot. An inspection robot is expected to reach inaccessible areas by navigation in confined places including inside narrow tubes and pipelines in harsh working environments. To fulfill these requirements, we have taken design principles adapted from the caterpillar. The caterpillar's prowess is due to a combination of design features that work together to permit rapid and smooth locomotion. The alternation of fastening between the front and rear legs generates linear locomotion. This functionality is achieved by the proposed robot by a light rigid structure made of 2 links connected by an active pivot joint that allows the climbing robot to extend and flex. The robot has six wheels in total, a pair of active wheels at each end to drive the robot, while two passive wheels are attached to the pivot joint. The pivot joint enables the robot to navigate inside a wide range of pipelines from 12 to 25 mm by changing its height. The joint also allows the robot to exert a force against the upper walls for holding the robot inside the pipes, which can be treated as an integrated holding force mechanism. Two locomotion modes to propel inside pipelines are presented, and a proposed motion strategy to navigate complex pipe configurations, including vertical and bent pipes, is presented and validated by a series of experiments.

To extend the working domain of the inspection robot, we study the possibility of merging the robot with an adhesion mechanism to perform more challenging tasks such as replacing manual inspection at heights. For that, numerous adhesion methods were investigated until we come up with an approach of using low-cost dry adhesive materials to address climbing challenges, including surface-to-surface transitions, and vertical and inverted locomotion with high payload capacity. This idea was inspired by the climbing action of caterpillars on vertical surfaces as stationary legs provide anchoring force to hold their weight. In addition, different dry adhesive materials were analyzed and the selection criteria for the appropriate adhesive material to cover the full range of motion were also demonstrated. Final experiments prove the viability of the insect-scale robot to navigate complex structures (vertically and invertedly) while performing different cases of surface-to-surface transitions. A payload-mass ratio of 120% was also achieved while climbing on a vertical surface.

The findings of this thesis prove the functionality of the insect-scale robot as the future replacement of the borescope to perform various maintenance tasks. It also demonstrates the potential of low-cost dry adhesive materials in the field of miniature climbing robots. It seems that using the concept of mimicking the locomotion pattern of biological creatures can result in an unprecedented mobility performance for an insect-scale robot in a lot of fields.

Table of Contents

Acknowledgment **v**

Abstract **vii**

List of Figures **xv**

List of Tables **xxi**

1 Introduction **1**
- 1.1 Classification of pipe Inspection Robots . . . 3
  - 1.1.1 Mobility Mechanisms . . . 3
    - 1.1.1.1 Fluid-driven Locomotion . . . 4
    - 1.1.1.2 Wheeled Locomotion . . . 4
    - 1.1.1.3 Tracked Locomotion . . . 5
    - 1.1.1.4 Legged Locomotion . . . 5
    - 1.1.1.5 Inchworm Locomotion . . . 5
    - 1.1.1.6 Limbless Locomotion . . . 6
  - 1.1.2 Traction Force Generation . . . 6
    - 1.1.2.1 Gravitational Force . . . 7
    - 1.1.2.2 Wall-Pressing Normal Force . . . 7
    - 1.1.2.3 Adhesive Force . . . 8
- 1.2 Comparative Discussion . . . 8
- 1.3 Miniaturization of In-pipe Inspection Robots . . . 9
- 1.4 Thesis Objective . . . 10
- 1.5 Thesis Structure . . . 11

2 Micro-Ultrasonic Motor **13**
- 2.1 Properties of Ultrasonic Motors . . . 13
- 2.2 Driving Principle . . . 14
- 2.3 Modeling and Formulation of Phenomena . . . 16
  - 2.3.1 Modeling of the Motion . . . 16
  - 2.3.2 Modeling of Temperature Variation . . . 19
  - 2.3.3 Relationship between Temperature, Natural Frequency, and Angular Velocity . . . 20
- 2.4 Validation of Phenomena . . . 21
- 2.5 Previous Approaches to Solve the Temperature Variation Problem . . . 26
- 2.6 Controller Design . . . 28
- 2.7 Motor-Sensor System . . . 30

2.8 Experiments . . . 34
  2.8.1 Experimental Setup . . . 34
  2.8.2 Experimental Results . . . 35
    2.8.2.1 Constant Speed Experiment . . . 35
    2.8.2.2 Variable Speed Experiment . . . 37
      Stepwise Square Wave Command: . . . 37
      Sinusoidal Wave and Triangular Wave Commands: . . . 38
2.9 Performance Evaluation . . . 40
2.10 Conclusion . . . 41

3 In-Pipe Insect-Scale Robot 43
3.1 Ground-based Microrobots . . . 43
3.2 Design and Prototype . . . 44
  3.2.1 Micro-geared Ultrasonic Motor . . . 44
    3.2.1.1 Design of Micro-geared Ultrasonic Motor . . . 44
    3.2.1.2 Evaluation of Micro-geared Ultrasonic Motor . . . 46
  3.2.2 Prototype Design . . . 48
3.3 Performance Evaluation . . . 48
  3.3.1 Mobility Characteristics . . . 48
  3.3.2 Force Generated by the Robot . . . 49
3.4 Locomotion Modes . . . 50
3.5 Holding Force Mechanism . . . 53
3.6 Motion Strategy for Complex Pipelines . . . 54
  3.6.1 Navigation in a Funnel Segment . . . 56
  3.6.2 Overpass a 90° Elbow . . . 56
3.7 In-Pipe Navigation Experiments . . . 57
  3.7.1 Experimental Setup . . . 57
  3.7.2 Navigation in Complex Pipelines . . . 59
3.8 Conclusion . . . 60

4 Climbing Capabilities Using Dry Adhesives 63
4.1 Basic Design Requirements of Climbing Robots . . . 63
4.2 Miniaturization of Climbing Robots . . . 64
4.3 Basic Climbing Skills of the Prototype . . . 65
  4.3.1 Vertical and Inverted Climbing . . . 65
  4.3.2 Surface-to-Surface Transition . . . 66
    4.3.2.1 Concave Transitions . . . 66
    4.3.2.2 Convex Transitions . . . 66
4.4 Adhesive Technology . . . 68
  4.4.1 Magnetic Adsorption . . . 69
  4.4.2 Air Pressure Adsorption . . . 71
  4.4.3 Mechanical Grasping Attachments . . . 74
  4.4.4 Electrostatic Adsorption . . . 74
  4.4.5 Bio-Inspired Adhesion . . . 76
  4.4.6 Comparative Discussion . . . 79
4.5 Adhesive Material Testing and Selection . . . 81
  4.5.1 Friction Adhesion Model . . . 81

4.5.2 Adhesive Material Durability 83
4.5.3 Adhesive Material Selection 85
4.5.4 Lifespan Prediction of Adhesive Materials 88
4.6 Experiments 89
4.6.1 Climbing and Surface-to-Surface Transitions 90
4.6.2 Payload Capacity 91
4.7 Performance Evaluation 93
4.8 Conclusion 93

5 Conclusion and Future Work **95**
5.1 Conclusion 95
5.2 Future Work 97

References **99**

List of Publications **115**

Achievements **117**

List of Figures

1.1 A borescope for industrial applications [10]. 2

1.2 The main mobility mechanisms for in-pipe inspection robots previously reported. [11] 3

1.3 Different approaches for traction force generation for in-pipe inspection robots previously reported. [11] 7

2.1 (a) Design of the stator and the vibration mode generated by the stator. A traveling wave is generated along the circumference of the hole. (b) Components of the micro ultrasonic motor 15

2.2 (a) The stator generates an elliptical motion on the stator–rotor interface and transfers a driving force to the rotor. (b) The mechanical model of the micro-ultrasonic motor 17

2.3 Change in the rotor's angular velocity when the frequency ratio varies. 21

2.4 Impedance-frequency characteristic of the micro-ultrasonic motor. 22

2.5 Driving setup to operate the micro-ultrasonic motor. 23

2.6 (a) Micro ultrasonic motor placed in the experiment setup and (b) tracking the marker attached to the rotor by a high-speed camera. 23

2.7 Illustration of the speed measurement setup of the micro-ultrasonic motor. A marker is attached to the load to facilitate the tracking motion by the high-speed camera. 24

2.8 The relationship between the angular velocity and the driving frequency. . . . 24

2.9 Temperature variation in the stator while three different values of input voltages are applied. 25

2.10 Variation in the natural frequency of the stator as the temperature increases. . . 25

2.11 Transient response of the micro ultrasonic motor. The experimental result behaves as a first-order system as approximated in the model. 27

2.12 Block diagram of the ESC controller for optimum angular velocity tracking. . . 30

2.13 ESC localization technique. 31

2.14 (a) The prototype of micro-ultrasonic motor. (b) Components of the sensor system. From the left; the bracket, the TMR sensor, and a neodymium permanent magnet. (c) The motor-sensor system, in which the TMR sensor and the magnet are attached to the bracket and the rotor, respectively. 32

2.15 The output voltage of TMR sensor as the magnet angle changes. 33

2.16 Illustration of motor's angular velocity measured by the TMR sensor and by the high-speed camera simultaneously 33

2.17 The steady-state error of the micro-ultrasonic motor caused by the temperature rise. The output of the TMR sensor (internal sensor) is accorded to that of the high-speed camera (external sensor). 34

2.18 The block diagram of the speed control system for the micro-ultrasonic motor. . 35

2.19 Experimental results when ESC is applied to the micro-ultrasonic motor's closed-loop system: (a) The angular velocity, (b) the driving frequency, (c) temperature variation of the stator, and (d) the associated input power. 36

2.20 Experimental results when two controller loops are applied for tracking stepwise commands. The ECS is controlling the driving frequency while the input voltages are controlled by a PID controller. (a) Comparison between the reference and the actual angular velocity, (b) the transient response, and (c) the driving frequency localized by ESC. 39

2.21 Speed response by dual control scheme (ESC and PID) under variable speed commands. (a) Sinusoidal wave command input. (b) Triangular wave command input. 40

3.1 (a) Example of the microgears made of metallic glass. (b) The components and the structure of the micro planetary gear train: the gear system with a ratio of 64 uses an output shaft, four long planetary gears, a long sun gear, 8 short planetary gears, and a short sun gear. 45

3.2 Design of the micro-geared ultrasonic motor, a metallic flange fixes the motor and the planetary gear train. 46

3.3 Experimental setup to examine the relationship between the load torque and the angular velocity. The micro-geared ultrasonic motor is coupled to the pulley that lifts a payload. While the load weight is attached to the pulley, a load torque is given to the motor's output shaft. 47

3.4 Relationship between the load torque and the angular velocity. 47

3.5 (a) CAD design of the insect-scale inspection robot, two micro-geared motors drive the front and rear wheels using bevel gears. Another micro-motor is controlling the resistance of the pivot joint, and it is connected to the joint using 2 spur gears. (b) Prototype of the insect-scale inspection robot. 49

3.6 The relationship between the robot speed and the applied voltages; (a) Speed vs. amplitude and (b) speed vs. frequency. 50

3.7 Motion of the wheeled robot connected to a weight. The robot can drag a weight of 10 g on a surface with a friction coefficient of 0.97. 51

3.8 Change in the speed when the amount of the weight varies. The graph presents the mean, the maximum, and the minimum data for 10 trials. 51

3.9 (a) Demonstration of the two different shape modes, (b) and (c) Show the transformation strategy to switch from both in-line to anti-slip modes. (d) Presents how the integrated holding force mechanism works. 52

3.10 Evaluation of the traction force for different holding angles (θ_h). After adjusting a different holding angle at a time, the force gauge pulls the robot forward until it slides. 54

3.11 (a) The relationship between the holding angle and the traction force, and (b) Change in the speed when the holding angle varies. 55

3.12 Complex pipeline setups; (a) A Funnel segment connects two different diameters pipelines, and (b) A 90° elbow to change the direction heading of the pipes by 90°. 57

3.13 Motion strategy to navigate through diameter expansion and contraction pipelines. 58

3.14 Control diagram circuit to drive the inspection robot through the pipelines. . . 59

3.15 Demonstration of the navigation through a funnel segment connecting two different diameter pipelines, the setup is placed on a 45° slope. 60

3.16 Demonstration that the robot can climb vertically after passing through a 90° elbow. 61

4.1 (a) Demonstration of concave and convex corners. (b) Motion strategy to make a concave transition. (c) and (d) a Comparison between two design approaches for a convex transition; (c) A normal wheeled robot and (d) a caterpillar-like robot. 67

4.2 Motion strategy for the caterpillar-like robot to make the convex transition. . . 68

4.3 The MINOAS magnetic crawler uses permenant magnets on the wheels and on the tails to climb vertical walls. [127] 70

4.4 Two servo motors are controlling the heading direction of a magnet to maintain magnetization force with irregular surfaces; (a) Design of the magnetic spherical wheel. (b) Actual prototype of the wheel. [128] 71

4.5 A climbing robot employs multiple passive suction cups to climb vertical walls. [133] 72

4.6 A climbing robot employs a movable double propellers design to propel the robot on horizontal and vertical surfaces; (a) and (b) different sizes of propellers were investigated in the research. [137] 73

4.7 Recon Scout XT robot uses rotary microspine wheels to achieve advanced mobility like stair climbing and curb mounting on rough surfaces. [142] 75

4.8 The Brachiation robot using elastic energy stored in its soft body and mechanical grippers to climb tree branches [143] 76

4.9 HAMR-E, an insect scale climbing robot, climbs inverted curved surfaces using electro-adhesion pads. [115] 77

4.10 Stickybot, a centimeter-scale prototype that can climb on glass using gecko-inspired adhesion. [150] 78

4.11 A 1.4 grams insect-scale prototype navigates a circular track by using capillary wet adhesion. [157] 79

4.12 Evaluation of the friction adhesion model for the adhesive materials; (a) Normal adhesive force experiment, wheels are pulled off vertically by the force gauge until detachment from the substrate. (b) Shear adhesive force experiment, driving torque (Pr_2) is increased gradually to the point wheels start to rotate. . . . 82

4.13 Adhesive forces characteristics of the tested adhesive materials. The graph shows the mean, the maximum, and the minimum data for 15 trials. 84

4.14 Durability test of the adhesive materials for 50 cycles. 85

4.15 Schematic of the static analysis of the climbing robot in vertical navigation. . . 86

4.16 Schematic of the static analysis of the climbing robot in inverted navigation. . . 87

4.17 Experimental setup to measure the relationship between propelling speed and the degradation of adhesive forces with the traveling distance. 89

4.18 Variation of vertical climbing speed as the adhesive material degraded with traveling distance. 90

4.19 Demonstration of vertical and inverted climbing along with 3 different cases of surface-to-surface transitions. 91

4.20 Demonstration of the vertical navigation of the prototype while a payload of 2 g is attached to it. 92

4.21 Snapshots of the robot in inverted navigation while carrying an extra payload, the robot finishes the task successfully. 92

4.22 Variation of vertical climbing speed based on the payload weight. The graph shows the mean, the maximum, and the minimum data for 6 trials. 93

List of Tables

1.1 Comparison between different driving mechanisms of in-pipe inspection robots. 9

2.1 Simulation parameters for the temperature variation in the micro-ultrasonic motor. 26

2.2 ESC parameters identification. 30

2.3 Comparison between the proposed rotary actuator-sensor system with similar prototypes. 41

4.1 Comparison of adhesive techniques 80

4.2 Comparison between the climbing capabilities of the proposed insect-scale robot with similar prototypes. 94

Chapter 1

Introduction

Robotic researchers have told us for decades that robots will become our good partners and enhance the quality of our lives, but this has not yet been achieved. Inspection, assessment, and maintenance of the industrial sites and existing civil structures and infrastructure are current trends, including large-scale constructs such as plants, tunnels, bridges, roads, and pipelines. Robots and automatic systems can perform the inspection process with objective results and high efficiency for those time-consuming and repetitive tasks. They can also improve safety by displacing workers from high-altitude, dangerous, labor-intensive, and cost-inefficient work environments. Therefore, human visual inspections are being replaced with more precise methods using mechanical, electronic, and robotic systems. To achieve these benefits, robot designs must consider quantitative sensing methods combined with wireless communication, robust locomotion appropriate for the inspection environment, and autonomous operation that guarantees comprehensive and repeatable inspections of hazardous sites.

Perhaps the biggest impediment to the widespread implementation of inspection robots is the inspection environment itself. Civil structures are rarely uniform in shape and generally either exist in harsh outdoor environments or buried underground [1]. Furthermore, structures are not typically designed with considerations for easy inspection access and often require climbing hundreds of vertical feet, navigation around and over complex obstacles, or digging the ground [2, 3]. The same problem is associated with machines, where inspection of complicated machines like turbine engines requires the disassembly of a lot of components which can be costly and time-consuming. Compounding the difficulty is that inspections must sometimes be done in dark, wet, and dirty environments that degrade the usefulness of commonly used sensors such as cameras or infrared [4].

A common element that exists in all industrial sites, civil structures, and machines is a countless number of tubes and pipelines to transport all kinds of fluidic materials, such as water, petroleum, natural gas, and oxygen [5, 6]. We consider these tubes and pipelines as direct routes to the core of an inspection site or a complicated machine. Imagine a miniature robot accessing and inspecting a whole turbine engine by fuel lines, that can be a time and cost-wise inspection. The robot can be also implemented to inspect and conduct necessary repairs to the pipelines themselves, as aging and external impact accidents can cause many problems in the pipeline systems, such as cracks, corrosion, or damages [7, 8]. This idea may sound similar to the well-known inspection industrial borescope, which is an optical instrument designed to assist visual inspection of narrow and difficult-to-reach cavities, inaccessible structures, and the core of complicated machines [9]. It mainly consists of a rigid or flexible tube with an eyepiece or display on one end, and an objective lens or camera on the other, linked together by an optical or electrical system in between as shown in Fig. 1.1. Despite these great benefits, the borescope is inherently rigid and extrinsically manually actuated by an operator which makes it hard to accurately guide the position of its tip to a specific spot. One of the main reasons is the absence of a powerful actuator in a micro-scale to be fitted in the borescope tip.

The challenges of the infrastructure environment mean that the development of robots capable of operating in a wide variety of inspection environments as a full replacement for conventional inspection tools is desirable. It is time to think then of the next generation of borescopes, researchers believed that a miniature mobile robot capable of navigating inside narrow tubes and pipelines efficiently could be the next generation of borescopes. However, robots at such a scale are still in the research stage as many challenges related to their actuation techniques, compliant design, fabrication technology, control structures, and power delivery are not fully addressed yet. This includes the degree of adaptability with variations in the pipe diameter, pipe orientation regardless of gravity, and working environments. This thesis outlines some of the challenges related to the development and implementation of an insect-scale in-pipe robot and presents new solutions that lead to extending the working domain of the robot to a new era.

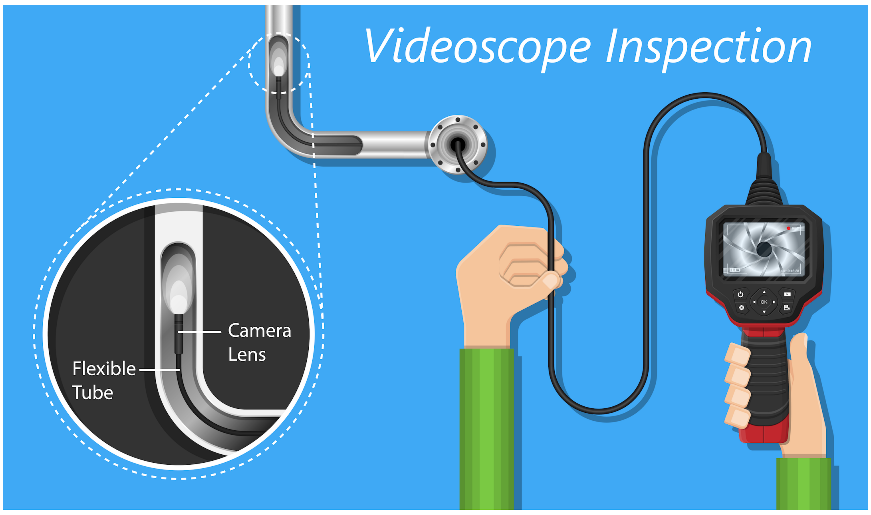

FIGURE 1.1: A borescope for industrial applications [10].

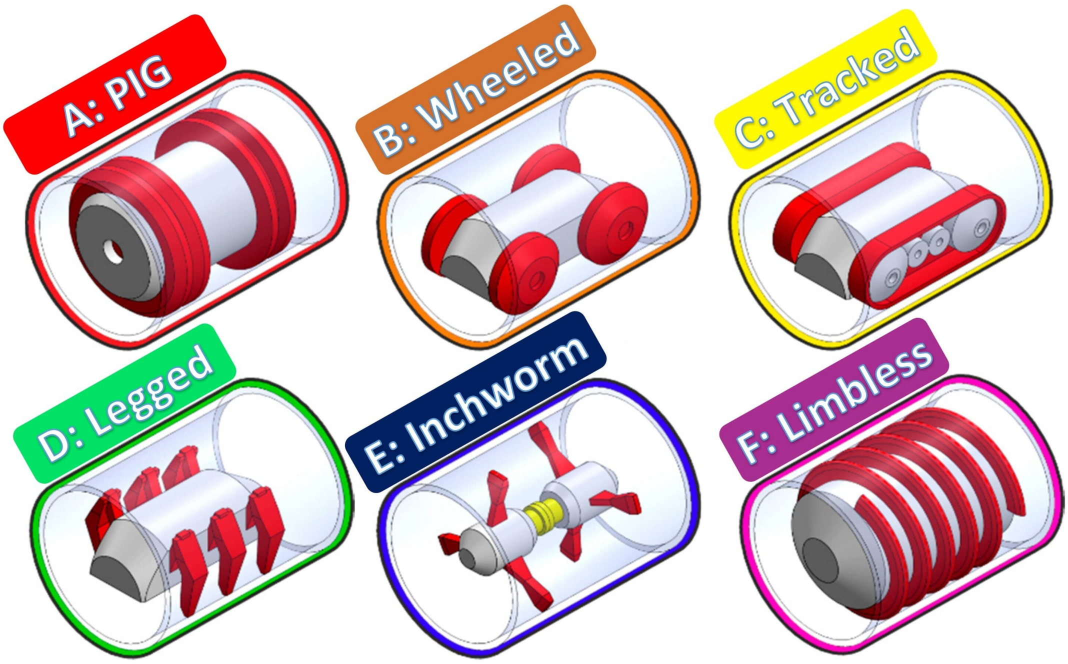

FIGURE 1.2: The main mobility mechanisms for in-pipe inspection robots previously reported. [11]

1.1 Classification of pipe Inspection Robots

Generally, pipe inspection robots can be roughly classified into outer-pipe and in-pipe inspection robotic systems. Outer-pipe inspection robots can perform pipe inspection without interrupting plant operations; however, they cannot inspect the inner pipe wall rigorously as opposed to the in-pipe robotic system. In-pipe robots enable an in-depth overview of the internal corrosion of the pipe, sludge built-up, and any problems related to the pipe. Furthermore, the use of the in-pipe inspection robotic system is beneficial when the pipes are buried underground or in any other inaccessible location. This research mainly focuses on in-pipe inspection robots, which have been a large number of prototypes proposed over the past two decades, all of which can be categorized by their mobility mechanism and traction force generation.

1.1.1 Mobility Mechanisms

One of the most important classifications for in-pipe inspection robots is their mobility mechanism as shown in Fig. 1.2. In the following subsections, we will briefly explain and highlighted the advantages and drawbacks of every mechanism.

1.1.1.1 Fluid-driven Locomotion

The fluid-driven in-pipe inspection robotic system is driven by compressed conveyance fluid. The difference in fluid pressures around the robot generates propulsive forces. The velocity of the propelled robot can be adjusted using flexible sealing elements and support on the robot's body. Pipeline inspection gauges (PIG) are the most popular inspection robots belonging to this category. PIG-type pipeline robots (Fig. 1.2 (A)) have a simple structure and can move inside straight pipelines by launching and receiving the robot at respective stations [12, 13]. It means that the robot can be deployed without the need to stop pumping the fluids. However, they struggle to turn at sharp bends and they require a proper tracking system to avoid the system from being stalled inside the pipe, which adds to the complexity of the control system. Since this category is considered an untethered system, an external monitoring system should be attached to the pipe for the signaling purpose of identifying the robot's movement inside the pipe during an inspection. The design also lacks adaptability features as every robot can be only applicable for a single pipe diameter.

1.1.1.2 Wheeled Locomotion

The wheel-type inspection robot (Fig. 1.2 (B)) is similar to the ordinary mobile robot which works on a basic mechanism by rotating the wheels by using various actuators for the driving force, and a number of commercialized robots have been reported up to now [14, 15]. This mechanism enables a robot to move rapidly and requires less energy when compared to other types of robotic locomotion mechanisms. Wheel-type robots can be divided into the directly driven wheel (active wheel) and passively driven wheel [16]. Some of the wheeled robots feature both active and passive wheels, they are categorized as hybrid wheeled type locomotion. In most of the previously reported prototypes, wheels were either made from rubber materials or from a metallic alloy. Rubber wheels are widely used as they feature simple structures and they are easy to process. Moreover, the friction coefficient of rubber materials is high which can improve the traction force. On the other hand, metallic wheels are much heavier and are widely used in magnetically attracted machines.

Although wheeled robots can move on turning pipes and winding pipes, it is hard for them to adapt to pipes with large diameter changes. Furthermore, the mobile robot tends to slip especially in wet conditions as it maneuvers inside the pipe due to the insufficient grip on the wall. This limitation can be overcome by using an in-pipe robot with wheels based on a multi-axis differential mechanism.

1.1.1.3 Tracked Locomotion

Track-based locomotion system (Fig. 1.2 (C)) is used in place of wheels when high traction force is needed. The large contact surface area makes these systems more stable and capable of withstanding higher payloads but also generally bulkier than their wheeled counterparts. That may prevent the downscaling of such a driving mechanism to a centimeter scale. The robot has three crucial components; the central body, the caterpillar wheel track, and the pantograph mechanism. Most of the previously reported tracked employ a multi-axis design [17–19], where the tracks (Usually 2 or 3) are connected symmetrically to the center module through the pantograph mechanism. The pantograph presses the tracks against the in-pipe walls with a partially passive spring mechanism coupled with a slider linkage mechanism or by external actuation force. This design increases the grip which allows incline and vertical in-pipe navigation. Moreover, it can be driven through curved and branch pipes as the differential speed of the tracks on both sides by controlling the speed of each driving track independently.

1.1.1.4 Legged Locomotion

The legged-type robot (Fig. 1.2 (D)) drives with the help of walking legs having several Degrees of Freedom (DOF). Legged robots can perform highly sophisticated motions and they have the merit to step over obstacles while traveling at a moderate speed. These robots are suitable for wet environments where the robot needs some clearance space from water droplets. However, some motion slipping can occur due to the poor traction force as a result of their small contact area with the pipe walls. The number of previously reported legged inspection prototypes is limited in the literature [20, 21], several reasons are involved but the most crucial element is due to the complicated control strategy needed to control the gait. The need for an independent actuator for each leg in most of the designs also adds to the complexity of the system, which results in a lot of actuators incorporated inside the robot which makes the system bulky. Moreover, this kind of foottype kinematic system is very complicated in design, production, installation, maintenance, and offers poor stability.

1.1.1.5 Inchworm Locomotion

Inchworm motion is also common for the locomotion of in-pipe inspection robots, which generally involve repetitive contraction and expansion motion of the robot's body as indicated in Fig. 1.2 (E). The high normal forces needed to support the robot during contraction make these systems generally well-suited for carrying high payloads. Most inchworm robots employ flexible fluidic actuators accompanied by ring-shaped tubes at each end that act as holding force mechanisms [22–25]. A typical inchworm motion is composed of periodic gaits that usually take five different steps to complete a single gait. The advantages of design lie in its adaptability to a wide range of pipelines and that it can propel into complex pipeline systems, including vertical and bend pipes. In addition, a fluidic actuator is practical and safe to be used in damp and wet conditions such as in water supply pipes because the actuator does not use electricity as its primary energy and has no risk of electrical leakage and short circuits in flammable working environments [26]. However, their locomotion speed is generally low compared with that of motor-driven robots, and they require many air supply tubes for bi-directional locomotion. Recently, the ring-shaped tubes have been replaced by some electrically actuated double-network hydrogel material that has better controllable friction properties [27].

1.1.1.6 Limbless Locomotion

Instead of exploiting wheels or legs, limbless robots utilize their body for propulsion. Most limbless robots consist of identical modules and the necessary propulsive effort for locomotion is accomplished by body undulation as shown in Fig. 1.2 (F). This category is widely known as helical or screw locomotion too. Many of the proposed designs are inspired by biological creatures like spirochete [28–30], which is a type of bacteria. The robot does not block the flow in a pipe because it has space inside its helical body through which fluids can flow. Despite the complex mechanism structure, the robot has a tendency to get jammed while moving through the bends of a confined space if the mechanism doesn't work properly. Although the robot has the merit of easily adapting to pipe diameter change, some concern arises about the damage marks on the inner walls due to the helical motion. To solve this dilemma, a twisted rubber tube robot is presented in [31], where the robot is driven by a continuous helical motion of a soft silicon rubber tube. As a consequence, scratch marks are no longer a potential threat.

1.1.2 Traction Force Generation

Another classification for the in-pipe inspection robots deals with the generation of traction force within the environments, in other words, the necessary force to keep the robot in continuous contact with the inner walls. It is worth mentioning that controlling the propelling velocity of the in-pipe robot is not easy unless the contact conditions between the wheels and the inner surface of the pipeline are determined precisely. This is also the major cause of the slip of the wheels and the degradation of the driving performance.

Many potential robotic solutions have been proposed before as presented in Fig. 1.3. Initially, when in-pipe inspection robots were presented, traditional gravity exploration robots were assigned for the task. These robots were generally built to handle rough terrain, they were not well suited to the pipeline complex environment and could explore only horizontal sections and

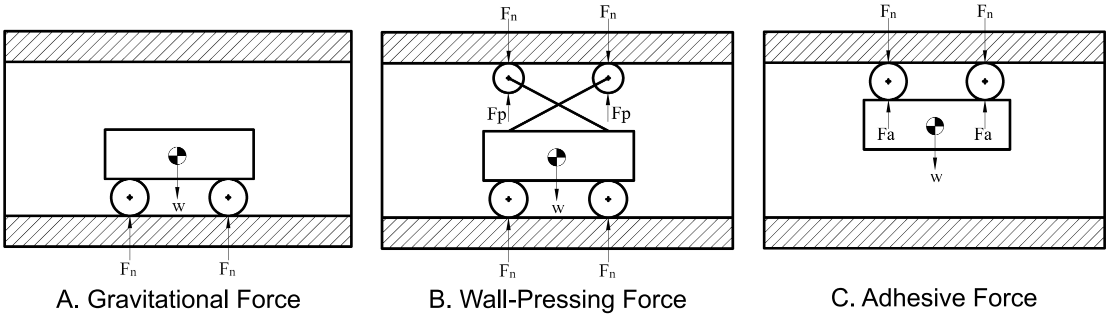

A. Gravitational Force B. Wall-Pressing Force C. Adhesive Force

FIGURE 1.3: Different approaches for traction force generation for in-pipe inspection robots previously reported. [11]

gentle inclines. Although these systems performed adequately in large-bore sewage and water-based networks. It wasn't until robotic systems developed advanced methods of in-pipe traction such as wall-pressing and adhesion through magnetic that the more complex pipeline configurations could be explored. Using the methods of traction in Fig. 1.3 as a design basis, many variations of in-pipe locomotion have been created to suit in-pipe sophisticated systems.

1.1.2.1 Gravitational Force

The most simple one relies on gravity to keep traction with the pipelines as shown in Fig. 1.3 (A). Wheeled robots, legged robots, and tracked robots are commonly locomotion mechanisms widely used in this category. As these robots have proved good robustness, excellent locomotion speed, simple control structure, high payload capacity, and efficiency in log-run applications, most of the existing commercially available in-pipe inspection robots belong to that category [14, 15]. Despite these great features, reliance on gravity alone restricts robots to only horizontal and slightly inclined pipelines. With no additional traction mechanism, there is a high tendency to slip especially in wet environments.

1.1.2.2 Wall-Pressing Normal Force

The wall-pressing technique utilizes the reaction of normal force from the enclosed walls to keep adequate traction while the robot is in motion as depicted in Fig. 1.3 (B). Screw robots, pipeline inspection gauge robots, limbless robots, and inchworm robots are all belong to that category. These robots prove good adaptability for navigation through complex pipeline systems such as a 90° elbow, a T-connection, or a C-type pipeline due to their high mobility. Good performance in both wet and dry conditions was also proven, as the traction ability is dominated by the constant pressure between wheels and pipe which can drive the robot forward or even hold its position. Their drawbacks are mainly related to the complex design structure of the holding mechanism, slow propelling due to the friction between the robot and the wall, and the requirement of complex control structures.

1.1.2.3 Adhesive Force

In this category, an adhesive force is generated between the robot and the pipe walls by different means as demonstrated in Fig. 1.3 (C). Most of the robots belonging to that category depend mainly on magnetic force interaction. The magnetic adsorption method adopts a permanent magnet or electromagnet (or a combination) and is suitable for use with ferromagnetic objects [32]. Although the robot can navigate complex pipeline systems including vertical pipes, its applicable working range is only limited to ferrous pipes. Magnetic wheels are commonly used in that category to provide propulsive forces, and several modules can be connected in series to overpass curved pipelines more efficiently. Although other adhesive techniques like suction cups (active and passive) were presented for climbing robots, the integration of these techniques is still limited in the field of in-pipe inspection robots. One of the reasons is related to the wet environments of most pipeline systems.

1.2 Comparative Discussion

All prototypes that have been discussed have the same general objective, which is to do an inspection inside pipelines. However, each of them has its own characteristics which adhere to its specific design requirements. As the requirement changes, every locomotion mechanism provides some limitations for current situations. The comparative study of the robots' driving mechanisms is given in Table 1.1. Based on the extensive review that was done on various in-pipe inspection robots, it is concluded that a wheeled-type motor-driven mechanism owns many features compared to other mechanisms. The mechanism features robustness, high driving forces, and locomotion speed, which fulfill the important requirements for an in-pipe inspection robot.

When it comes to the traction force mechanism, the mechanism should not spoil the advantages of the motor-driven mechanism. For instance, gravitational force seems a promising traction solution for traveling in simple horizontal pipeline structures, however, the robot wouldn't have any adequate traction for vertical pipes or work in wet conditions. Wall-pressing normal force is better than gravitational force in such challenging situations, but that will come at the cost of the propelling speed. The logical solution is therefore to adopt a design with hybrid traction techniques which will allow the in-pipe inspection robotic system to adapt and reconfigure in completing the inspection process more efficiently. The robot can be operated in two different traction modes, which are the gravitational force that can be applied as long as high-traction

TABLE 1.1: Comparison between different driving mechanisms of in-pipe inspection robots.

Criteria	PIG	Wheeled	Tracked	Legged	Inchworm	Limbless
Manoeuvrability	×	✓✓✓	✓	✓✓✓	✓	✓✓
Adaptability	×	✓✓✓	✓✓✓	✓✓	✓	✓✓✓
Horizontal Navigation	✓✓✓	✓✓✓	✓✓✓	✓✓✓	✓✓✓	✓✓✓
Vertical Navigation	×	✓✓	✓✓	×	✓	✓✓
Stability	✓	✓✓	✓✓✓	✓✓	✓	✓
Locomotion Speed	✓✓	✓✓	✓	✓	✓	✓

forces are not required, and the wall-pressing force that overcomes the shortages of gravitational force by improving the traction ability substantially whenever needed.

1.3 Miniaturization of In-pipe Inspection Robots

To improve the efficiency of in-pipe inspection, researchers have also been concerned about miniature prototypes of in-pipe inspection robots. A robot that can reach difficult-to-reach areas by accessing narrow tubes or pipelines that act as direct routes is advantageous. Currently, a wide range of pipelines of 25 mm diameter or less is commonly used for water and gas supplies inside buildings [33]. A miniature in-pipe robot can be very convenient to access and inspect these pipelines efficiently. Most of the existing literature on miniature in-pipe robots that were developed for narrow pipes is dedicated to wall-press flexible robots [22–25]. They employ various pneumatic-driven motion mechanisms to propel inside the pipelines. Inchworm, peristaltic, and helical motions are common modes of locomotion by using one or more air chambers that are pressurized independently. Although flexible robots have proven their advantages in narrow pipelines in terms of flexibility and holding force, the use of many air supply tubes adds to the complexity of the design [34].

On the other hand, despite having a high driving force and locomotion speed, motor-driven mechanisms are not popular in miniature in-pipe robots. A significant reason for this trend is the challenge of making and assembling the components necessary for a motor-driven robot. In general, robots designed at centimeter scales can generally rely on the assembly of off-the-shelf components. For example, inexpensive actuators (DC motors and shape memory alloy), sensors (position, inertial, etc.), and microcontrollers can be combined easily to make both wheeled robots and legged robots. However, the assembly of off-the-shelf components is no longer feasible at the millimeter scale. Driving motors and the holding force mechanisms must be fabricated especially which is not an easy task as their mechanisms consist of many rigid components, which are difficult to downsize [35]. The same problem is associated with the associated integrated sensors.

Due to all these challenges, the performance of a micro-scale in-pipe inspection robot does not match that of a macro-scale. Therefore, a robust miniature motor-driven in-pipe robot with an adjustable wall-pressing mechanism is desirable in the field of pipeline inspection systems.

In conclusion, we can summarize the primary challenges in the development of insect-scale robots to the following:

- Motors: What is the best way to design and fabricate efficient motors with high power densities to support locomotion?
- Mechanisms: How will robust mechanisms for mobility and traction generation be fabricated at these scales?
- Control: How can sensors and controllers be integrated on robots at this size scale and what are the best controllers to use for stable optimized locomotion?
- Locomotion Criteria: How will these robots move through their environment? What methods of locomotion are effective and efficient at these size scales?
- Power: What energy storage technologies can be integrated at these size scales and how the power transmission will be integrated with motors and controllers?

1.4 Thesis Objective

This thesis argues to design and build an insect-scale inspection robot that can overcome the limitations and weaknesses of current inspection tools. The robot can reach inaccessible areas by navigating inside a wide range of miniature tubes with an integrated holding force mechanism. The robot can also access these areas by other means like overcoming large obstacles where other robots would fail if integrated by an adhesive technique. To support this argument, subsequent chapters studied the actuation mechanism, control structure, design and locomotion modes, fabrication criteria, and adhesive technology of a caterpillar-inspired insect-scale in-pipe robot. Explicitly enumerate the objectives:

- Construction of the actuation mechanism that can drive the robot with excellent performance. To achieve that target, we must construct and investigate the time-variant performance of micro-ultrasonic motors. That can be only achieved by applying adaptive control techniques to eliminate the steady-state error of the motors throughout a closed-loop control structure.
- Design an insect-scale in-pipe inspection robot with an integrated holding force mechanism. To evaluate the active adaptability of the robot's linkage mechanism to navigate complex pipeline systems, several experiments are performed.

- Study the possibility of merging the robot with an adhesion mechanism to perform more challenging tasks such as replacing manual inspection at heights. For that, stability analysis and many experiments are performed to prove the viability of the insect-scale robot to navigate complex structures (vertically and invertedly) while performing different cases of surface-to-surface transitions.

1.5 Thesis Structure

This thesis is comprised of five chapters. Chapter 1 introduces different locomotion mechanisms and traction techniques while addressing the current challenges to minimize these systems. Chapter 2 investigates the performance of micro-ultrasonic motors as the actuation mechanism for the intended robot. We address the root causes of the steady-state error that exists in the motor and model the phenomena, and then several experiments have been carried out to verify the hypothesis experimentally. An adaptive controller that can coop with non-linear temperature-dependent characteristics of ultrasonic motors is then presented and tested. Experiments confirm that the controller eliminates the steady-state error by stabilizing the angular velocity of a micro-ultrasonic motor for a prolonged operating time under fixed and variable speed commands. Chapter 3 describes the design scheme and the locomotion patterns of the pipeline robot and then introduces the principle of operation of the integrated holding force mechanism. A description of the active motion strategy to navigate complex structures is elaborated and tested. Chapter 4 presents different adhesive technologies and elaborates on the testing methodology of the dry adhesive materials and the selection criteria of the appropriate tape based on the static analysis of the prototype. Experiments are carried out to demonstrate that the robot makes an unprecedented mobility performance for an insect-scale climbing robot. Chapter 5 summarizes the outcomes of the thesis and points out possible future work for the proposed approach.

Chapter 2

Micro-Ultrasonic Motor

Micro actuators are needed for a variety of purposes, ranging from practical applications such as medical and industrial endoscopes to scientific investigations such as controlling biomimetic microrobots. Downsized to a 2-3 millimeter scale, electromagnetic actuators that dominate at the macro-scale diminish their power due to their scaling law [36, 37]. Furthermore, they involve several technical problems to miniaturize the components, such as coils, permanent magnets, and bearings. Instead, piezoelectric ultrasonic motors perform at such a scale as the most prominent microactuators because of their high power density and good machinability [38, 39].

2.1 Properties of Ultrasonic Motors

Ultrasonic motors are actuators that primarily use the mechanical vibrations of piezoelectric elements to convert electrical energy into mechanical energy [40–43]. Input electrical AC voltages are applied to piezoelectric elements to generate expansion and contraction motions. The displacement of piezoelectric oscillations is amplified at the mechanical resonance of a stator. A rotor pressed against the stator moves by receiving the vibration via a frictional force.

The first applied in-practice ultrasonic motor is a rotational traveling-type ultrasonic motor made in Japan in 1986. Since then, ultrasonic motors have been used for autofocusing systems in camera lenses, head-rest control in cars, and calendar-turning mechanisms in mechanical watches [44, 45]. These adoptions are thanks to the excellent features of the ultrasonic motors that be summarized as:

- High power/weight ratio
- High power at low speed

- High holding torque at zero speed
- Quick response time
- Compact size and lightweight
- Resistant to external magnetic fields

Despite these great features, ultrasonic motors suffer from obvious nonlinear and time-varying characteristics that complicate their models for control, the necessity of a high-frequency power supply also adds to the complication of the drive circuit.

2.2 Driving Principle

There are many types of driving principles of ultrasonic motors including traveling waves, standing waves, and multi-mode excitation[46–50]. In the proposed motor, we employ the traveling wave as the driving principle as it features a simple structure that is easy to downsize. The left in Fig. 2.1(a) shows the stator in the axial direction. Four piezoelectric elements are bonded to the metallic cube with a hole. When voltage $E_1 = A_E \sin(2\pi f_E t)$ and its reserved-phase voltage $E_3 = -A_E \sin(2\pi f_E t)$ are applied to the upper piezoelectric element (PZT1) and bottom piezoelectric element (PZT3), respectively, PZT1 contracts and PZT3 expands or vice versa. Repeating contractions and expansions generate a three-wave mode along the stator hole (the right in Fig. 2.1(a)). In voltages E_1 and E_3, A_E is the amplitude and f_E is the frequency of the applied voltages. Likewise, when voltages $E_2 = A_E \cos(2\pi f_E t)$ and $E_4 = -A_E \cos(2\pi f_E t)$ are applied to the right piezoelectric element (PZT2) and left piezoelectric element (PZT4), respectively, the stator generates another three-wave mode with an angular difference of $\pi/2$ from the first one. When these voltages are applied simultaneously, two three-wave modes are combined along the circumference of the hole, and then this combination produces a traveling wave. This traveling wave generates an elliptical motion that transfers the driving force to the rotor via friction.

Fig. 2.1(b) shows the components and structure of the micro ultrasonic motor. It is constructed of a stator, a rotor, a contact part, a micro spring, and a rotor end. The stator is composed of a phosphor bronze cube with a side of 2 mm, and at the center, there is a hole with a diameter of 1.4 mm used for the rotor to pass through. The piezoelectric elements use hard materials with a high-quality factor (C-213, Fuji ceramics, Japan). A piezoelectric plate is polarized in the thickness direction and is cut to the desired size by a dicing saw. The four piezoelectric plates with a dimension of 2 mm × 1.6 mm and a thickness of 0.6 mm are bonded to the four surfaces of the stator by a conductive adhesive. The micro spring has an outside diameter of 0.8 mm, a wire diameter of 65 μm, and a natural length of 1.1 mm. When a rotor end is attached to the

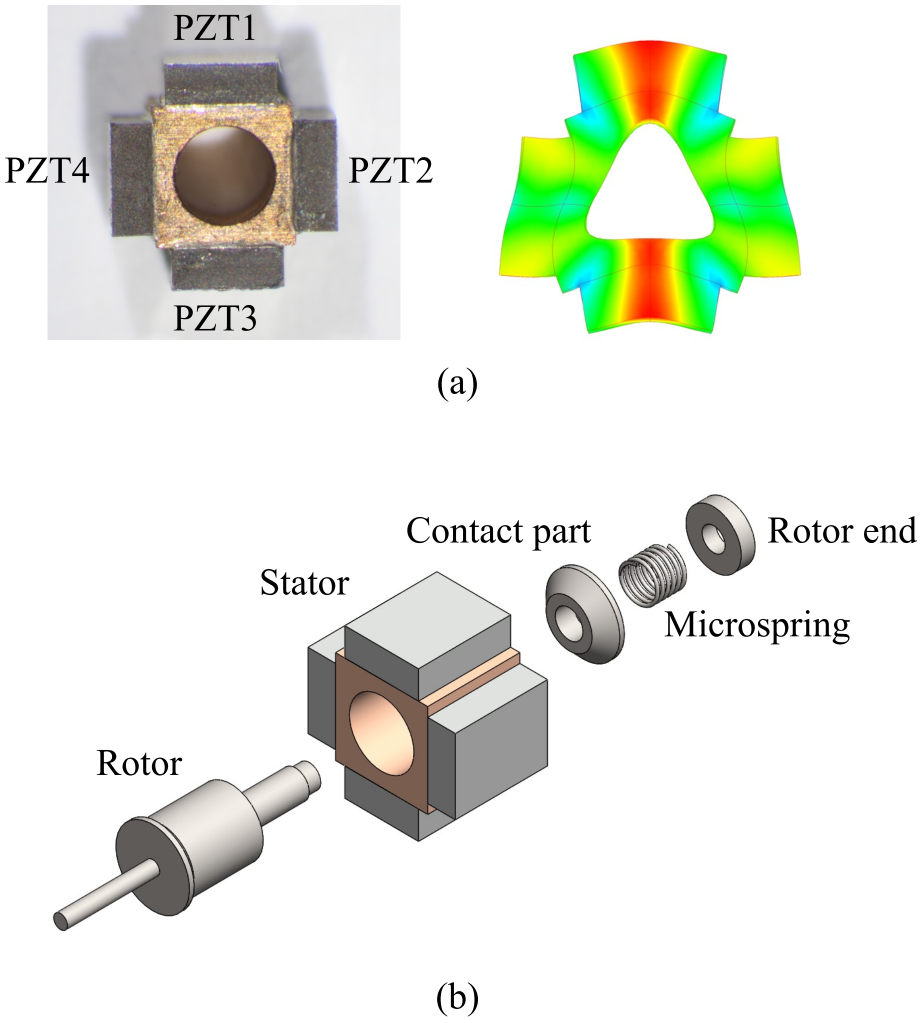

FIGURE 2.1: (a) Design of the stator and the vibration mode generated by the stator. A traveling wave is generated along the circumference of the hole. (b) Components of the micro ultrasonic motor

shaft, the micro spring is compressed to 0.6 mm, and a spring force of approximately 50 mN is exerted along the axial direction of the rotor as a preload.

The preload presses the rotor against the stator, which results in vibration amplitude transferred to the rotor as a result of the large friction between the elastic stator's body and the rotor [51, 52]. However, several internal power losses that occur in ultrasonic motors are mainly due to the mechanical damping of the stator, the dielectric loss of the piezoelectric elements, and the friction at the stator-rotor interface [53]. These dissipations result in a temperature rise that affects the stiffness of the piezoelectric material and the natural frequency of the stator [54]. This phenomenon makes the performance of traveling wave ultrasonic motors highly unstable, rotational speed is usually decreased and even meets with a sudden standstill which limits the usage of these motors in constant speed applications [55]. The problem also affects the lifetime of actuators as high temperatures accelerate the wearing of the friction layers and can cause permanent damage to the piezoelectric material [56]. None of the ultrasonic motors, therefore, can retain a desired steady state without control.

2.3 Modeling and Formulation of Phenomena

2.3.1 Modeling of the Motion

In ultrasonic motors, the stator is considered an electromechanical energy converter, in which the input voltages are converted into mechanical motion when the input voltages are applied to the piezoelectric elements. That produces a traveling wave on the inner surface of the stator circumferentially. The mass particles on the surface where the traveling wave moves generate an elliptical motion in the stator-rotor interface, spinning the rotor by frictional contact force as illustrated in Fig. 2.2(a). In general, the motion of that mass particle can be modeled as a mechanical system consisting of springs and damper elements in the horizontal and vertical directions. Fig. 2.2(b) shows the modeled mechanical system. In this system, we define the mass of the particle by m_s, the horizontal and vertical spring coefficients by k_x and k_y, respectively, and the horizontal and vertical damping coefficient by c_x and c_y, respectively.

For the motor to rotate, the rotor absorbs the vibration energy from the stator by friction and converts it into its rotational motion. The energy absorption is determined by the preload force F_N between the stator and rotor as detailed in [51]. By assuming the stator-rotor contact as an energy absorption factor with damping coefficients b_x and b_y in the horizontal and vertical direction, respectively, the equation of motions of the stator's vibration can be expressed as

$$\begin{aligned} m_s\ddot{x} + (c_x + b_x)\dot{x} + k_x x = F_x \\ m_s\ddot{y} + (c_y + b_y)\dot{y} + k_y y = F_y \end{aligned} \tag{2.1}$$

Where F_x and F_y are given by

$$\begin{aligned} F_x &= F_0 \cos(\omega t) \\ F_y &= F_0 \sin(\omega t) \end{aligned} \tag{2.2}$$

where F_o is the net force applied from the stator to the rotor and ω is the vibration frequency. The net force can be derived by

$$F_0 = n_1 V - F_N \tag{2.3}$$

where n_1 is the coupling factor that represents the electromechanical (voltage-to-force) conversion. The modeled system is well known as a forced harmonic vibrating system in which driving the system at its resonant state maximizes the vibration amplitudes [57]. The system is

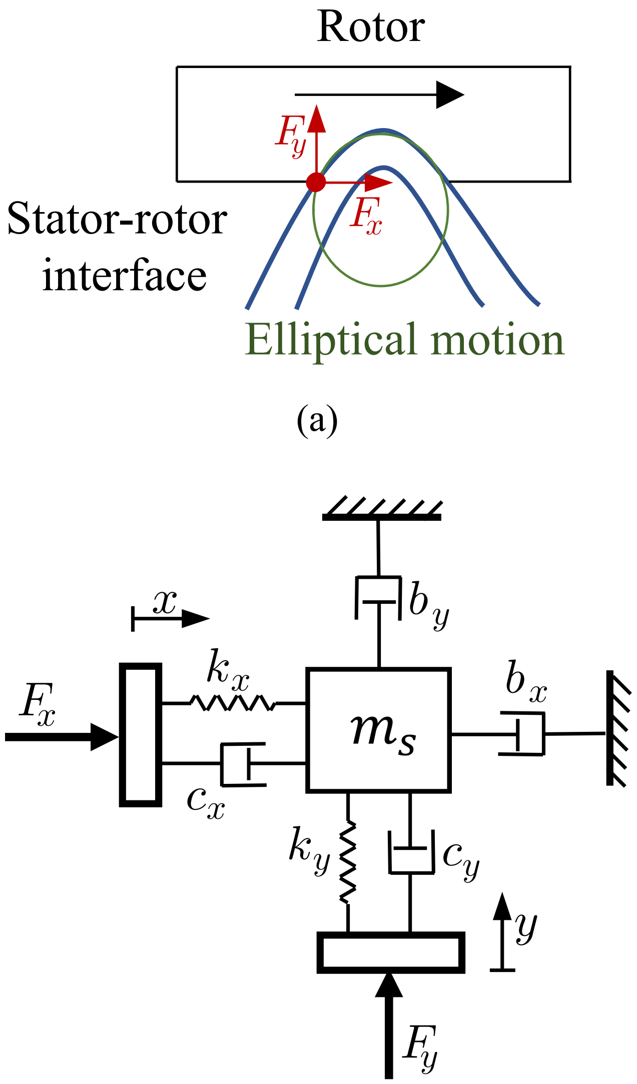
Rotor
F_y
F_x
Stator-rotor interface
Elliptical motion
b_y
x
k_x
F_x
m_s
b_x
c_x
k_y
c_y
y
F_y

(a)

(b)

FIGURE 2.2: (a) The stator generates an elliptical motion on the stator–rotor interface and transfers a driving force to the rotor. (b) The mechanical model of the micro-ultrasonic motor

at a resonant state if the applied frequency ω equals to its natural frequency ω_n which can be calculated as follows

$$\omega_n = \sqrt{\frac{k_x}{m_s}} = \sqrt{\frac{k_y}{m_s}} \tag{2.4}$$

The steady-state response of the vibrating system in the horizontal and vertical axis can be derived as

$$\begin{aligned} x(t) &= \frac{F_0}{[(k_x - m_s\,\omega^2)^2 + (c_x + b_x)^2\,\omega^2]^{1/2}}\cos(\omega t - \phi_1) \\ y(t) &= \frac{F_0}{[(k_y - m_s\,\omega^2)^2 + (c_y + b_y)^2\,\omega^2]^{1/2}}\sin(\omega t - \phi_2) \end{aligned} \tag{2.5}$$

Where ϕ_1 and ϕ_2 are given by

$$\begin{aligned} \phi_1 &= tan^{-1}\left[\frac{(c_x + b_x)\,\omega}{k_x - m_s\,\omega^2}\right] \\ \phi_2 &= tan^{-1}\left[\frac{(c_y + b_y)\,\omega}{k_y - m_s\,\omega^2}\right] \end{aligned} \tag{2.6}$$

As the elliptical motion starts, the mass particle moves with the peak horizontal velocity at the top point. As the rotor is in contact with the top point, it spins at an angular velocity $\mathit{\Omega}$. The peak horizontal velocity $\dot{x}_{max}$ can be derived by differentiation (2.5) as follows

$$\dot{x}_{max} = \frac{F_0\,\omega}{[(k_x - m_s\,\omega^2)^2 + (c_x + b_x)^2\,\omega^2]^{1/2}} \tag{2.7}$$

By dividing both the numerator and denominator of (2.7) by k_x and substituting (2.4) into it, the peak horizontal velocity can be expressed as

$$\dot{x}_{max} = \frac{F_0\,\omega/k_x}{[[1 - (z)^2]^2 + [\frac{d_x}{m_s\,\omega_n}z]^2]^{1/2}} \tag{2.8}$$

where d_x is defined as the total damping in the horizontal direction ($d_x = c_x + b_x$), while z is defined as the frequency ratio of the system that can be expressed as

$$z = \frac{\omega}{\omega_n} \tag{2.9}$$

By transforming this peak horizontal velocity into the rotor's angular velocity, $\mathit{\Omega}$ can be computed as

$$\mathit{\Omega} = \frac{\dot{x}_{max}}{r} \tag{2.10}$$

where r is the effective radius of the micro ultrasonic motor. Substitute (2.8) into (2.10), the rotor's angular velocity can be expressed as

$$\mathit{\Omega} = \frac{F_0\,\omega}{k_x r[[1 - (z)^2]^2 + [\frac{d_x}{m_s\,\omega_n}z]^2]^{1/2}} \tag{2.11}$$

The above equation is used when the moment of inertia is very small or neglected, i.e., no load is attached to the rotor. In other cases, the angular velocity can be calculated using the equation of motion for rotor dynamics as follows

$$I\,\dot{\mathit{\Omega}} - \nu_m\,\mathit{\Omega} = \tau - \tau_l \tag{2.12}$$

where τ is the applied torque, I is the moment of inertia, ν_m is the damping coefficient, and τ_l is the load torque that acts against the motor torque.

2.3.2 Modeling of Temperature Variation

The existing mathematical models of ultrasonic motors can estimate the response of the angular velocity under certain input voltages and torques; however, they cannot derive the steady-state error without considering the temperature of the stator. It is essential to model how the temperature rise affects the dynamic and steady-state characteristics of the rotation in the time domain. The heat dissipation generated in the micro-ultrasonic motor is due to the dielectric loss of the piezoelectric materials q_e, the mechanical damping of the stator q_m, and the friction loss between the stator and the rotor q_f. The total power dissipation q in the motor is the sum of these factors:

$$q = q_e + q_m + q_f \tag{2.13}$$

By subtracting the power q_d that radiates to the ambient air from the total dissipation q, the change in the stator's temperature T is expressed using the conversion of energy:

$$q - q_d = m\,c_p \frac{dT}{dt} \tag{2.14}$$

where m and c_p are the mass and the specific heat of the stator, respectively. The heat that dissipates to the ambient air with a temperature of T_0 by convection through the surface area A_s can be expressed as

$$q_d = K_T A_s (T - T_0) \tag{2.15}$$

where K_T is the heat convection coefficient. Eq. (2.14) shows that the surface temperature of the stator reaches the steady state when the radiation q_d is equal to the total loss q. By substituting (2.15) into (2.14), the stator temperature T is obtained as follows:

$$T = T_0 + \frac{q}{K_T\,A_s}(1 - e^{-\frac{t}{\gamma}}) \tag{2.16}$$

where $\gamma = mc_p/K_T A_s$ is the heat dissipation constant. When voltages with an amplitude E are applied, the total power loss q can be identified as $q = n_2 E$, and (2.16) can be rewritten as

$$\Delta T = \frac{n_2 E}{K_T\,A_s}(1 - e^{-\frac{t}{\gamma}}) \tag{2.17}$$

From (2.17), we can estimate how the input voltages affect the temperature rise.

2.3.3 Relationship between Temperature, Natural Frequency, and Angular Velocity

It is known that, in existing ultrasonic motors, the temperature rise lowers the stiffness of the piezoelectric materials, resulting in a decrease in the natural frequency. The micro-ultrasonic motor is more sensitive to temperature variation because the volume ratio of the piezoelectric material to the stator is larger than normal ultrasonic motors. Although the relationship between the temperature rise and the natural frequency is nonlinear, it can be approximated as a linear function in the range that the ultrasonic motor operates. Taking k_x previously described in the mechanical model of the motor in (2.1) as an example, the degradation of the spring constant due to temperature can be expressed as follows

$$k_x = k_{x0} - \alpha_x (T - T_0) \tag{2.18}$$

where k_{x0} is the original spring constant at $T = T_0$ and α_x is the coefficient of spring degradation. By substituting (2.17) into (2.18), we got

$$k_x = k_{x0} - \alpha_x \frac{n_2 E}{K_T\, A_s}(1 - e^{-\frac{t}{\gamma}}) \tag{2.19}$$

The change in the spring constant causes a shift in the natural frequency of the mechanical system expressed in (2.4) as follows

$$\omega_n = \sqrt{\frac{k_x}{m_s}} = \sqrt{\frac{k_{x0} - \alpha_x \frac{n_2 E}{K_T\, A_s}(1 - e^{-\frac{t}{\gamma}})}{m_s}} \tag{2.20}$$

Eq. (2.9) shows that a shift downward of the natural frequency enlarges the frequency ratio z of the system. Eq. (2.11) predicts that enlarging z will diminish the angular velocity of the rotor. To validate this point, we plot Eq. (2.11) with z as a variable while all other elements are kept constant at a unity value as shown in Fig. 2.3. The graph is compliant with the analysis of a damped forced harmonic system in [57].

At the initial configuration of the system, we manually adjust the driving frequency to match the natural frequency to operate the motor at the resonant state ($z = 1$). After the temperature rises, the natural frequency drops and the frequency ratio z becomes larger than 1. As a consequence, the system is no longer operated at the resonant state and the angular velocity drops.

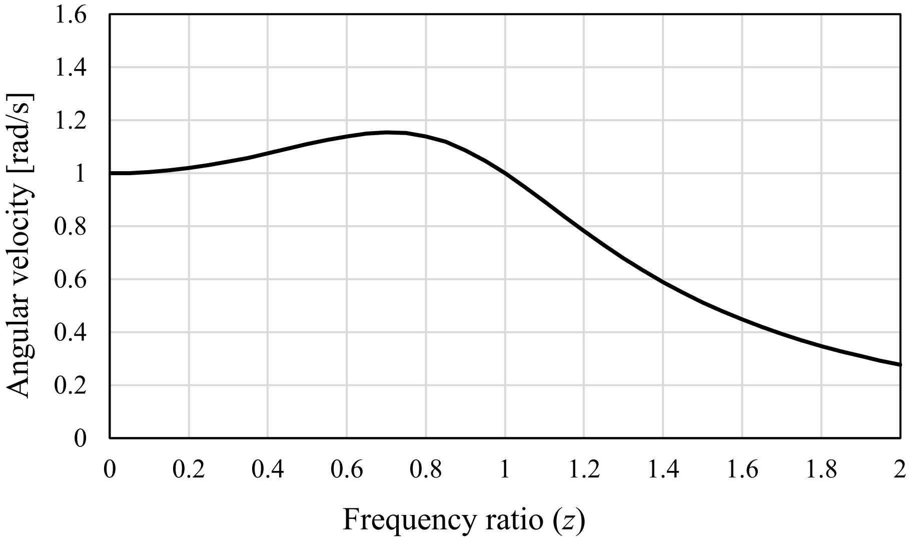

FIGURE 2.3: Change in the rotor's angular velocity when the frequency ratio varies.

2.4 Validation of Phenomena

The natural frequency of the vibration modes generated in the stator can be computed by a piezoelectric analysis based on the finite element method (FEM) (FEMTET, Murata Software Co., Japan). The FEM software shows that the stator generates three waves around the hole at a resonant frequency of 525 kHz. We can verify the FEM-based resonant frequency by experimentally measuring the natural frequency at a controlled room temperature of 25° C using an impedance analyzer (IM3570, Hioki E. E. Co., Japan). To measure the impedance of the motor, we connect the piezoelectric elements PZT1 and PZT3 to the signal and ground lines of the impedance analyzer, respectively, using contact probes. Fig. 2.4 shows the frequency response of the impedance when the frequency f_E varies around the resonant frequency. The decrease in the impedance indicates the existence of resonance. Besides, it shows the impedance characteristic between the piezoelectric elements PZT2 and PZT4. The resonant frequency at PZT2–PZT4 is in good agreement with that at PZT1–PZT3. This agreement enables the simultaneous excitation of the two three-wave modes to generate a traveling wave.

The next step is to experimentally evaluate the frequency characteristic of the motor, i.e., the variation in the angular velocity with the input frequency. In the measurement of the angular velocity, we manipulate the frequency while the two input sinusoidal voltages keep constant at 100 $\mathrm{V_{p-p}}$. These input voltages are generated using a wave generator with two channels (WF1974, NF Corp., Yokohama, Japan) and amplified by power amplifiers (BA4825, NF Corp., Yokohama, Japan). Furthermore, two transformers are used to generate voltages with reversed phases. For example, when voltage E_1 with a sine phase is input to a transformer, voltage E_3 with a negative sine phase is output from a transformer terminal. Similarly, when voltage E_2

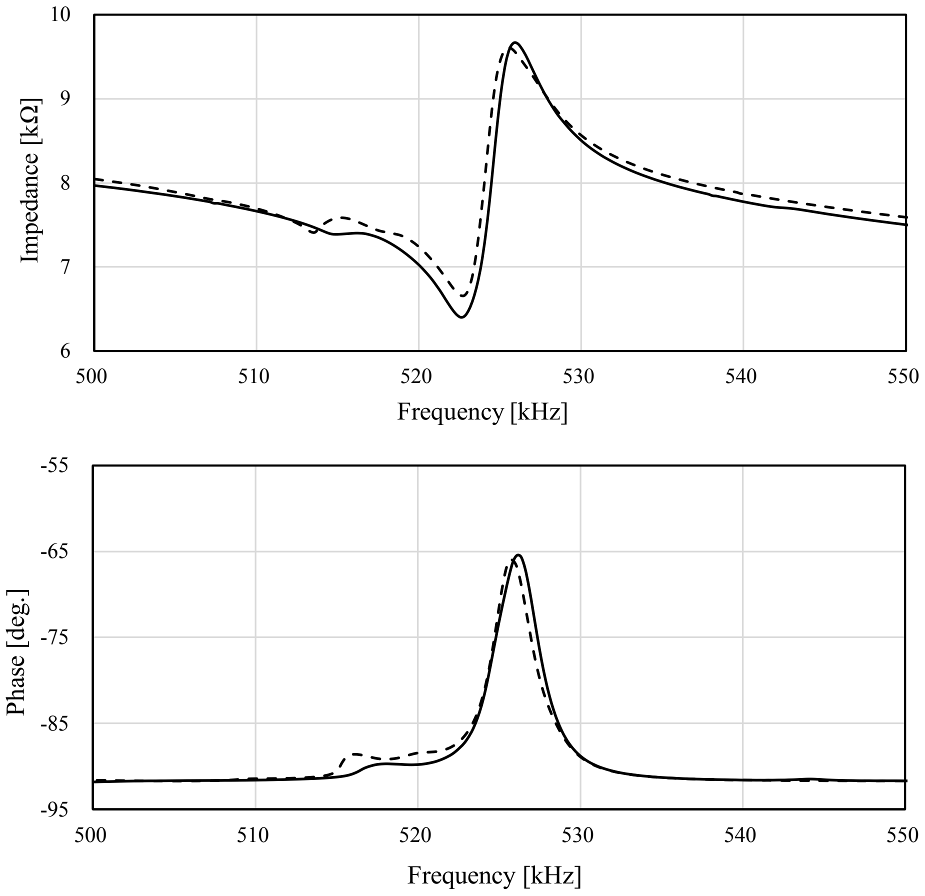

FIGURE 2.4: Impedance-frequency characteristic of the micro-ultrasonic motor.

with a cosine phase is input, voltage E_4 with a negative cosine phase is output. The driving setup is illustrated in Fig. 2.5.

To measure the angular velocity, a small bronze disc with a diameter of 3 mm and a thickness of 1 mm is attached to the end of the rotor as a load, as shown in Fig. 2.6(a), because the angular velocity without any load is too fast to be measured. A marker is also attached to the disc to facilitate the speed measurement. The motor angular velocity is measured using a high-speed camera with an image resolution of 320×240 pixels at 2000 fps (VW-9000, Keyence Co., Tokyo, Japan). By applying the input voltages, the rotor with the load starts spinning and the time-history data of the angular displacements are accumulated from the marker's movement in the images as shown in Fig. 2.6(b). The motor's angular velocity and acceleration can be computed by performing the time derivation of the tracking data as depicted in the overall speed measurement illustration in Fig. 2.7.

Fig. 2.8 shows the frequency characteristic of the steady-state angular velocity when the constant voltages are applied. The angular velocity peaks at 528 kHz, which is slightly higher than that of the resonant frequency of the stator without the rotor. That is because the preload

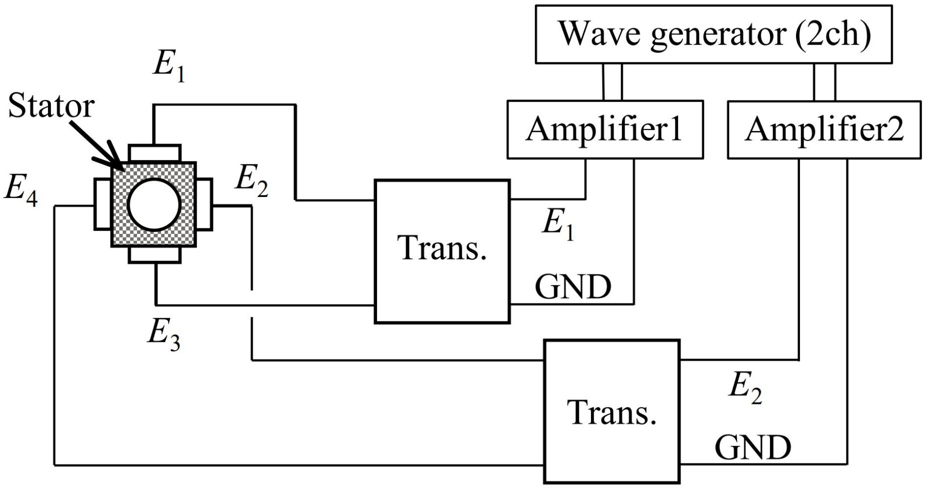

FIGURE 2.5: Driving setup to operate the micro-ultrasonic motor.

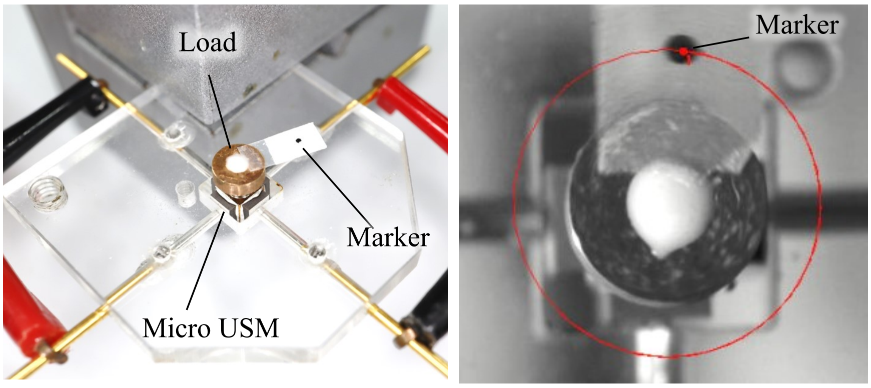

(a) (b)

FIGURE 2.6: (a) Micro ultrasonic motor placed in the experiment setup and (b) tracking the marker attached to the rotor by a high-speed camera.

force attached to the rotor enhances the stiffness of the stator, and it shifts the resonant frequency upward [58]. A peak torque of 60 μNm can be obtained from the angular acceleration and moment of inertia ($J_m = 1.1 \times 10^{-10}\,\mathrm{kgm}^2$) at the initial time when operated at resonant state.

To evaluate the extent of the actual temperature rise, we measure the time-history response of the stator's temperature during the motor operation. The surface temperature of the stator is measured by a spot finder IR camera (Xi 400, Optris Co., Germany) while the room temperature is constant at 25° C. Fig. 2.9 shows the time-history of the increment in the temperature ΔT when the amplitudes of 80, 100, and 120 $\mathrm{V_{p-p}}$ are applied. The experimental results are in good agreement with the simulation results of the temperature variation model shown in (2.17). Table 2.1 summarizes the parameters necessary for the simulation.

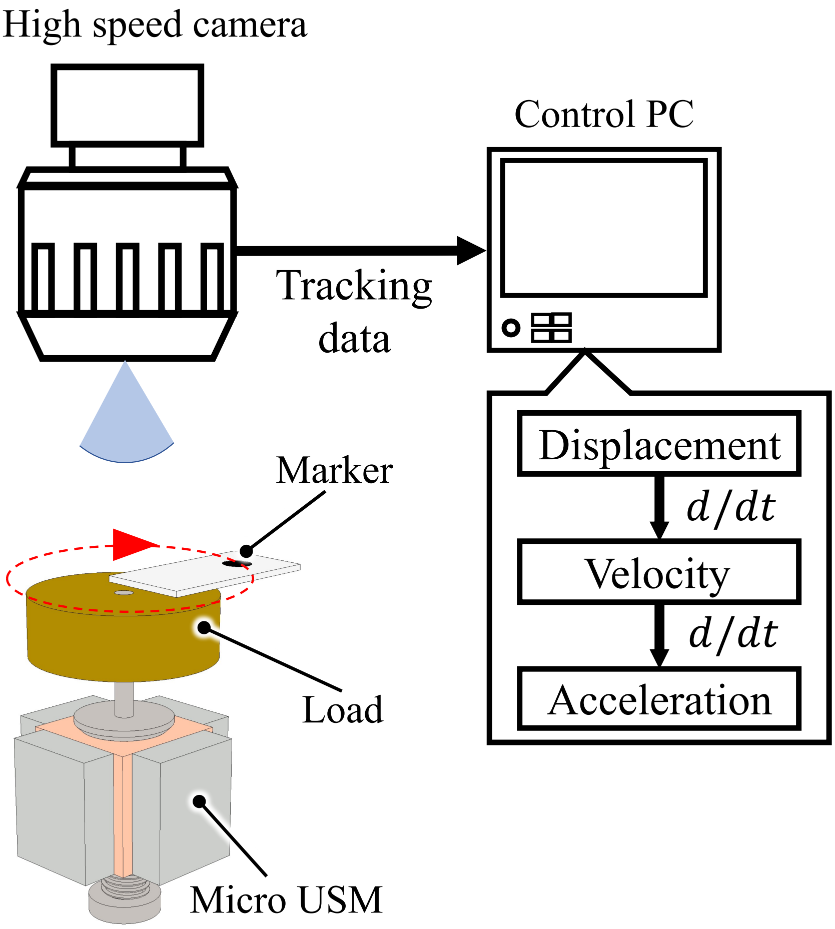
High speed camera
Control PC
Tracking data
Marker
Displacement
d/dt
Velocity
d/dt
Acceleration
Load
Micro USM

FIGURE 2.7: Illustration of the speed measurement setup of the micro-ultrasonic motor. A marker is attached to the load to facilitate the tracking motion by the high-speed camera.

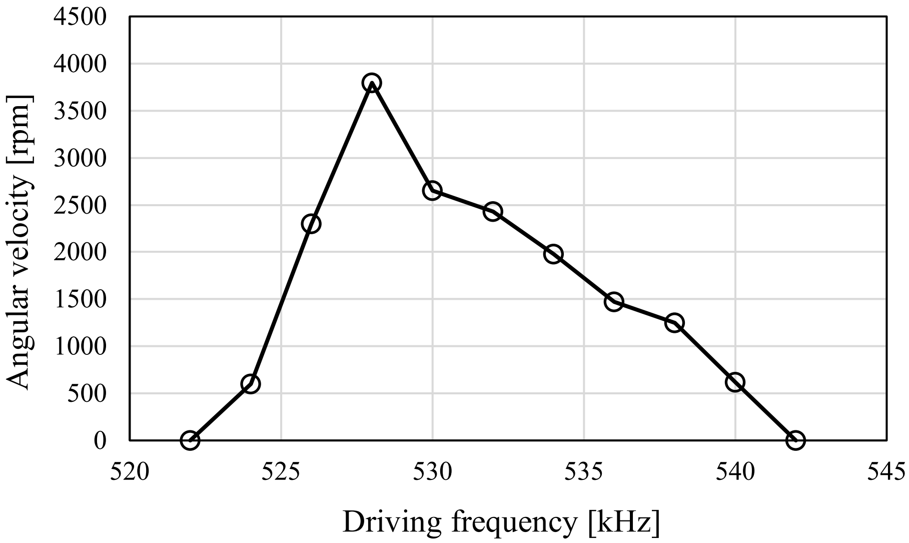

FIGURE 2.8: The relationship between the angular velocity and the driving frequency.

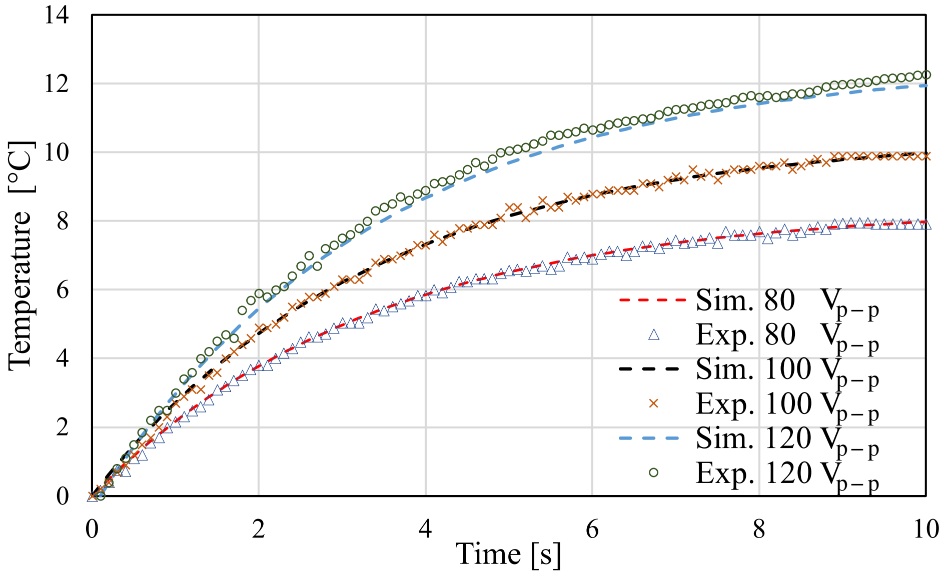

FIGURE 2.9: Temperature variation in the stator while three different values of input voltages are applied.

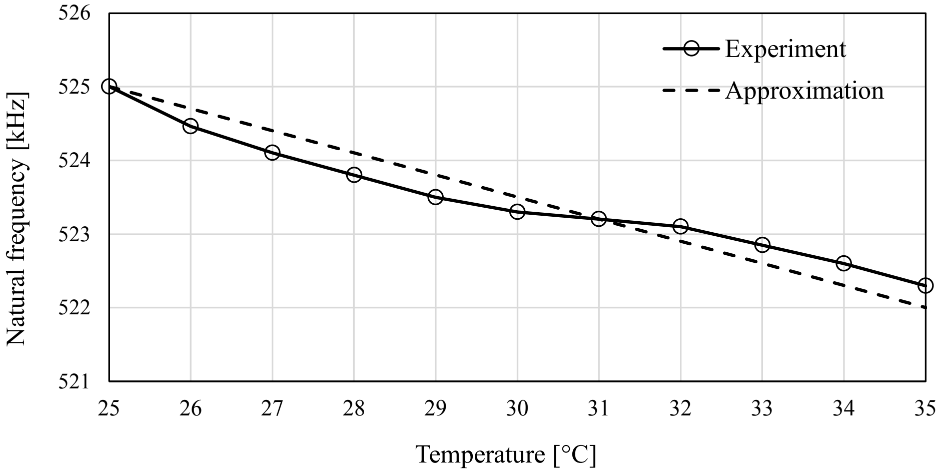

FIGURE 2.10: Variation in the natural frequency of the stator as the temperature increases.

We also examine how the temperature rise of the stator relates to the natural frequency as previously explained in section II-C experimentally. In this experiment, the stator is heated by flowing warmed air until $\Delta T = 10°$ C, while the resonant frequency is continuously recorded by the impedance analyzer. Fig. 2.10 shows the variation in the natural frequency of the stator when the temperature increases. The result shows that the resonant frequency is roughly linear to the temperature.

From Fig. 2.9 and Fig. 2.10, we can predict that the temperature rise enlarges the steady-state error as it alters the natural frequency of the stator. Because the micro-ultrasonic motor

TABLE 2.1: Simulation parameters for the temperature variation in the micro-ultrasonic motor.

Quantity	Symbol	Value
Volt/temp. constant	n_2	1.28×10^{-6}
Stator mass	m	0.0001 kg
Specific heat	c_p	0.435 kJ/kg ° K
Surface area	A_s	3.7×10^{-6} m^2
Heat conv. coeff.	K_T	3.3

cannot generate inherent performance at the non-resonant state, a controller that tracks the natural frequency and keeps the frequency ratio z in (2.11) equal to 1 is required.

2.5 Previous Approaches to Solve the Temperature Variation Problem

Many researchers have started to address the temperature problem and many control strategies have been proposed for the traveling wave ultrasonic motor in order to make it run smoothly and give full play to its advantages. The researchers' approaches can be mainly divided into two main categories; the first one is to control the operating temperature of the motor, and as a result, the motor will run at a stable speed. For example, Ou et al. [59] introduced a water-cooling system into the motor assembly. Although the design is efficient for large ultrasonic motors, it is complicated to implement the system for micro-scale size motors which will lead to the enlargement of the ultrasonic motor. Other researchers [60] proposed a different approach of switching on and off the input signal to the motor at a fast rate using the pulse width modulation (PWM) technique, allowing the motor to cool down between pulses. However, this approach lessens the maximum operating speed of the motors, minimizes output torque, and was only evaluated for a duration of almost 1s, which may be insufficient for the manifestation of temperature-related nonlinearities.

On the other hand, other researchers were primarily focused on developing control methods that led to a constant output performance under temperature variations. During continuous studies, researchers have realized that the ultrasonic motor has a different way of operating from the traditional one, and the motion control strategies designed for it must adapt to its own characteristics. In general, controlling traveling-wave ultrasonic motors (TWUSMs) are classified into two states: transient and steady states. The transient response of ultrasonic motors is in good agreement with the model based on the first-order system [61, 62]. Although the response speed depends on the moment of inertia, ultrasonic motors can reach the desired velocity within milliseconds as estimated in the model [63, 64], Fig. 2.11 shows the transient response of the micro ultrasonic motor.

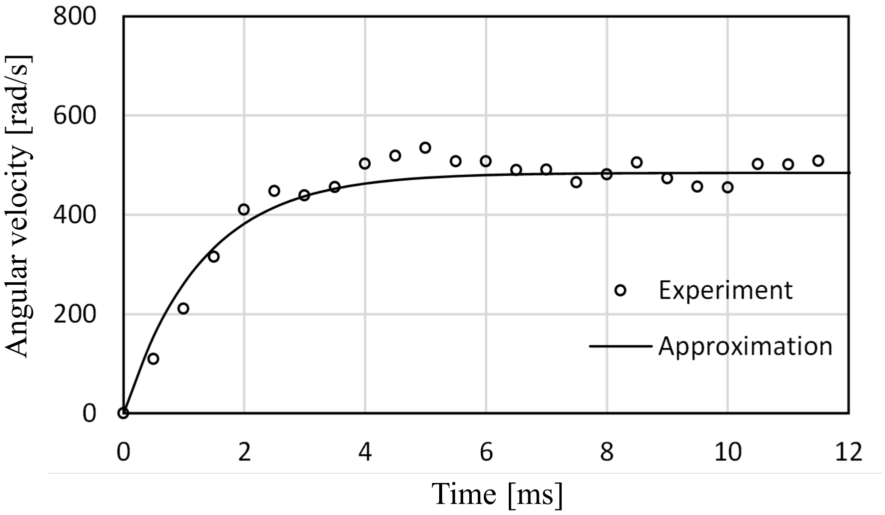

FIGURE 2.11: Transient response of the micro ultrasonic motor. The experimental result behaves as a first-order system as approximated in the model.

To control the angular velocity in the steady states, there are three manipulated variables: the voltage amplitude, the frequency, and the phase difference of the input signals [65]. In these, changing the driving frequency gives a more flexible range from a low-speed domain and is widely applied for the motion control of ultrasonic motors. Many approaches to developing control strategies for manipulating the angular velocity of ultrasonic motors have been previously reported. Classical PI and PID controllers [66, 67], fuzzy logic controllers [68, 69], neural network controllers [70], and adaptive controllers [71, 72], have been proposed as control algorithms for ultrasonic motors. For instance, classical controllers are simple and offer a wide stability margin but fail to cope with time-varying systems if not equipped with self-learning capabilities or an auto-tuning algorithm. On the contrary, a fuzzy logic controller can deal with nonlinear systems, but it relies too much on the designer's knowledge to define fuzzy rules. Both neural networks and adaptive controllers can adapt to the time-varying parameters of systems, thus suppressing the disadvantages of the classical and fuzzy controllers. However, the use of the neural network requires intricate online training iterations for output optimization. Although adaptive controllers seem promising, most of the existing methodologies are based on the model reference adaptive control (MRAC) approach. As most identified models of ultrasonic motors are based on classical linear system identification, estimating an accurate model for the MRAC approach is very complex. Therefore, designing a model-free adaptive controller that can handle the nonlinearity of ultrasonic motors and converge quickly to the optimum state is desirable.

2.6 Controller Design

Obtaining a good controller for a micro-ultrasonic motor is the key to this study, but it is as hard as accurately modeling the system. In the frequency-velocity characteristic (Fig. 2.8), the angular velocity peaks at the resonant frequency, which is treated as an optimal state. A controller that can converge the output of a system to the optimal state is necessary. The majority of adaptive controllers are model-dependent controllers designed for plants with known setpoints or tracking trajectories to the optimal state. Typically, these setpoints or trajectories are initially determined from the system dynamic model and updated by real-time system optimization [73]. On the contrary, another class of adaptive controllers is model-free like the extremum seeking controller (ESC) which can drive the system to optimal conditions without any prior knowledge about the process model [74, 75], yet provides desirable performance. This controller has a simple structure, a high robustness performance, and a fast convergence rate [76], and can also adapt to the change in plant dynamics.

In the past few years, many researchers have presented several schemes of extremum seeking control for nonlinear systems [75, 77–79]. The most two known approaches are perturbation-based and model-based ESC. On the one hand, a perturbation-based ESC adapts excitation by an external signal approach to find the unknown optimal operating condition of the plant. This technique optimizes the objective function by online measurement while considering that the input-to-output map is not known at all and that the estimation of derivatives of this map is done directly. It is simple and efficient as long as the transient response of the objective function is guaranteed to be on the right path of optimization. Its drawbacks are mainly related to that it relies too much on measured parameters and that the perturbation frequency must be slow. Many approaches have been proposed to improve the convergence rate of the perturbation-based ESC. For example, a dual-mode ESC and a phase compensator were introduced in [80] to neutralize the phase shift introduced by the system dynamics to the perturbation signal.

On the other hand, a model-based ESC is more convenient for systems with an accurate dynamical model even though some of its parameters are uncertain. It combines optimum search and adaptive control to guarantee the objective function's convergence to the optimum operating point. It requires explicit knowledge of the mathematical model of the plant, the objective function and its gradient, which may not be available for some systems. The literature is rich with many engineering applications where ESC is dominant, such as automotive applications [81, 82], mobile sensor networks [83], and fuel cell control in power plants [84].

Since real-time accurate speed measurements are used in the computations of our systems, and since the proposed model has some linearity assumptions around the operating range and some uncertainty, we adapt the perturbation-based ESC as the adaptive control scheme for the proposed closed-loop feedback system. The ESC algorithm could handle the non-linear constraints imposed by the temperature fluctuations inherently. With the driving frequency as a manipulated variable, the ESC is implemented to maximize a given objective that is defined as the rotor's maximum angular velocity as follows:

$$J = \mathit{\Omega}_{max} \tag{2.21}$$

Fig. 2.12 shows the schematic diagram of the ESC. The ESC aims to calculate the gradient of the objective function, and it continuously updates the control parameters to make the objective function maximum throughout the following three main processes.

1. Modulation process: The parameter being optimized is perturbed with a sinusoidal signal of amplitude A and frequency ω_p. In our case, the signal is induced to the input driving frequency $\hat{f}_{input}$ as it is the parameter being optimized as

   $$f_{input} = \hat{f}_{input} + A\ \sin(\omega_p\, t) \tag{2.22}$$

   The system's response to the input signal is the objective function $\mathit{\Omega}$ that we target for optimization.

2. Demodulation process: The perturbed signal f_{input} is applied to the system and the associated response $\mathit{\Omega}$ is measured. The response is filtered by a high pass filter (HPL) with a cutoff frequency ω_c. The cutoff frequency must be lower than the perturbation frequency ω_p to remove signal bias from the objective function without affecting its value. The gradient of the controller ζ is determined by correlating the filtered response with another sinusoidal perturbation having a unit amplitude and the same frequency as ω_p. Thus,

   $$\zeta = \mathrm{HPL}(\mathit{\Omega}) \times \sin(\omega_p\, t - \phi) \tag{2.23}$$

   Where ϕ is the delayed time imposed by the system dynamics. The sign of the gradient indicates the current controller position compared to the optimum point as indicated in Fig. 2.13. If ζ is positive, the current driving frequency is lower than the natural frequency of the system. On the contrary, if ζ is negative, the current driving frequency is higher than the natural frequency.

3. Parameter update process: The gradient is integrated over time and multiplied by a gain K to get a faster convergence. Updating the control parameter at time step n can be computed as follows:

   $$\hat{f}_{input}(n) = \hat{f}_{input}(n-1) + K \int \zeta\, dt \tag{2.24}$$

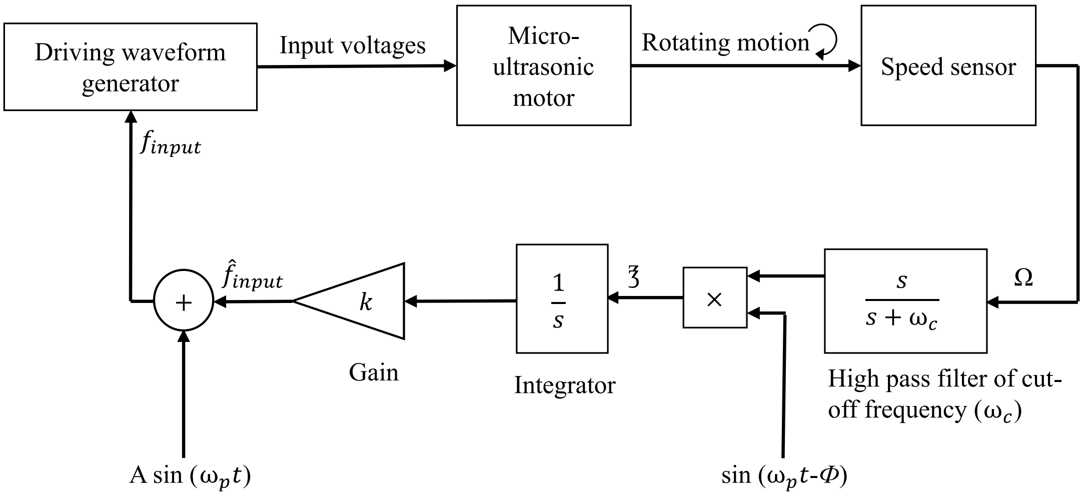
Driving waveform generator
Input voltages
Micro-ultrasonic motor
Rotating motion
Speed sensor
f_{input}
$\hat{f}_{input}$
+
k
Gain
$\frac{1}{s}$
Integrator
ξ
×
$\frac{s}{s+\omega_c}$
Ω
High pass filter of cut-off frequency (ω_c)
A sin ($\omega_p t$)
sin ($\omega_p t$-Φ)

FIGURE 2.12: Block diagram of the ESC controller for optimum angular velocity tracking.

TABLE 2.2: ESC parameters identification.

Parameter	Symbol	Value
Perturbed frequncy	ω_p	300 Hz
Cutoff frequency	ω_c	240 Hz
Perturbed amplitude	A	200 Hz
Gain	K	350
Sampling frequency		4000 Hz

The convergence rate of the driving frequency to the optimum frequency is proportional to the slope of the objective function. In other words, the integral gradient changes at a higher rate when Ω is far from the maximum value, while the steps become finer in the neighborhood of the optimum value Ω_{max}. At this point, the gradient stays almost constant.

Reached to the optimum value Ω_{max}, f_{input} oscillates around the current value until the system dynamics change again; the ESC sweeps for the new optimum driving frequency. Table 2.2 summarizes the parameters of the ESC. The frequencies ω_p and ω_c are set lower than the parameters of the operating system to prevent any interference. The sampling frequency is limited by the response time of the control circuits. The gain K is optimized to get an appropriate response within the working domain of the motor while considering the time-varying nonlinear characteristics of the motor. In other words, a too-fast convergence may lead to unstable condition for the motor and even meets with a sudden stop.

2.7 Motor-Sensor System

To implement the control structure to the ultrasonic motor, constructing a closed-loop motor-sensor system is absolutely necessary, but there was no tiny sensor that can be attached to the

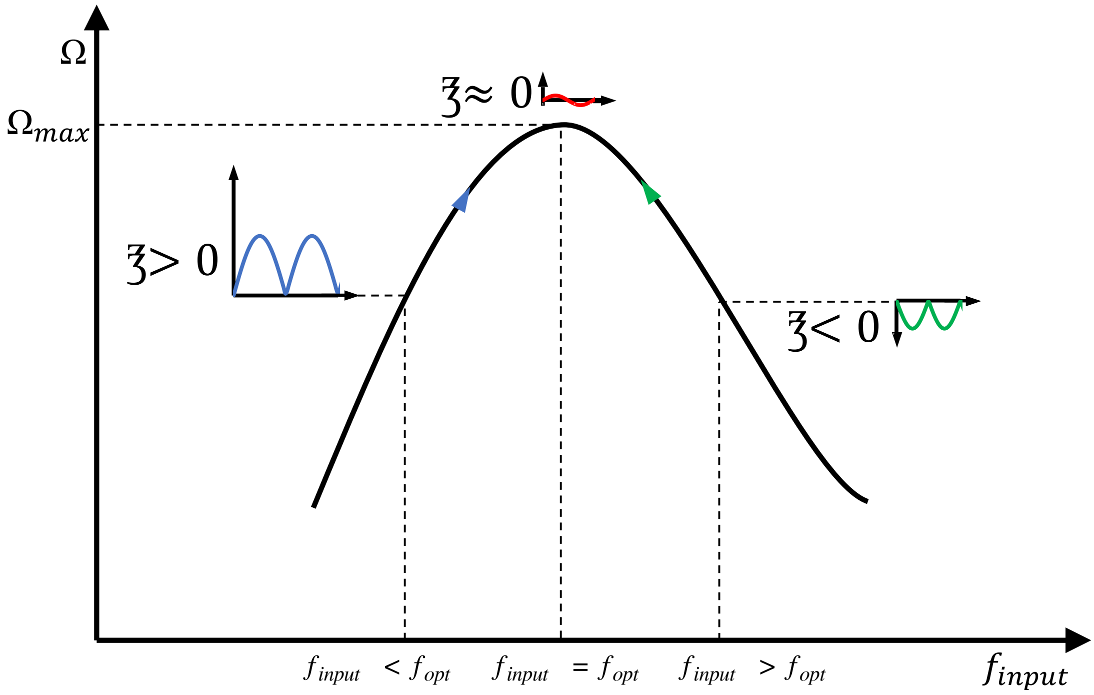

FIGURE 2.13: ESC localization technique.

micro-ultrasonic motor to detect the angular velocity. In other words, existing commercially-available rotary sensors, e.g., optical and hall sensors, were much larger than the micromotors and spoiled the advantage of the micromotors. The same problem is associated with the usage of the high-speed camera to calculate the rotational speed as indicated in Section 2.4. The camera is too bulky and it takes a lot of time to analyze the subsequent images. Recently, one of the leading sensor companies provided us with the smallest tunneling magneto resistance (TMR) sensor (TAS2240-YIAA, TDK Corp, Ltd, Japan). It is capable of detecting 360° of rotation angle despite its tiny size of 1.4 mm × 1 mm × 0.6 mm, which is very suited for the micro-ultrasonic motor.

Fig. 2.14(a) shows a prototype of a micro-ultrasonic motor, its total length measuring approximately 5 mm. Fig. 2.14(b) shows the components of the sensor system: from the left; a bracket, the TMR sensor, and a tiny magnet. The magnet is a cubic neodymium permanent magnet with a size of 0.5 mm × 0.5 mm × 0.5 mm (Niroku Manufacturing, Tokyo, Japan). Fig. 2.14(c) shows the motor-sensor system. The magnet is attached to the end of the rotor and spins with the rotor together. The bracket printed by a 3D printer (ProJet 3510HD Plus, 3D Systems Co., USA) holds the TMR sensor near the tiny magnet. When the motor is driven, the tiny magnet spinning with the rotor changes the direction of the magnetic field. The TMR sensor detects the alteration of the magnetic field and outputs a sinusoidal analog voltage corresponding to the change. We can calculate the angular displacement by converting the analog voltage to

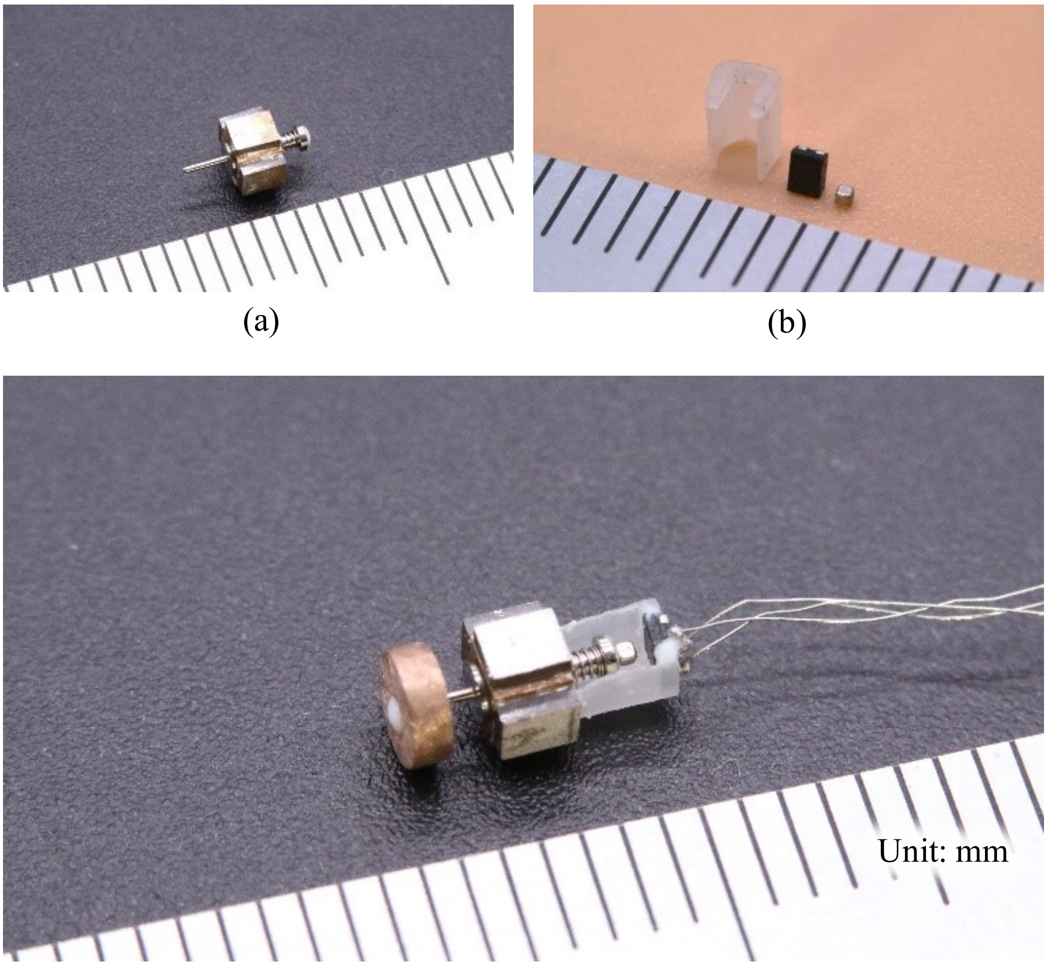

(a) (b)

(c)

FIGURE 2.14: (a) The prototype of micro-ultrasonic motor. (b) Components of the sensor system. From the left; the bracket, the TMR sensor, and a neodymium permanent magnet. (c) The motor-sensor system, in which the TMR sensor and the magnet are attached to the bracket and the rotor, respectively.

the angle. Fig. 2.15 shows the output signal of the TMR sensor when the magnetization angle changes.

To confirm the accuracy of the TMR sensor, we measure the open-loop angular velocity of the motor with the TMR sensor as an internal sensor, and simultaneously, the high-speed camera records the same motion as an external sensor as illustrated in Fig. 2.16. Fig. 2.17 shows the time-history response of the angular velocity for a period of 10 s. The angular velocity recorded by the TMR sensor is well accorded with that recorded by the high-speed camera. Besides, Fig. 2.17 shows the steady-state error; that is, after reaching the peak at the initial time, the angular velocity gradually decreases. This is because the temperature rise affects the stiffness of the piezoelectric material and the natural frequency of the stator. This steady-state error will be removed in the following sections.

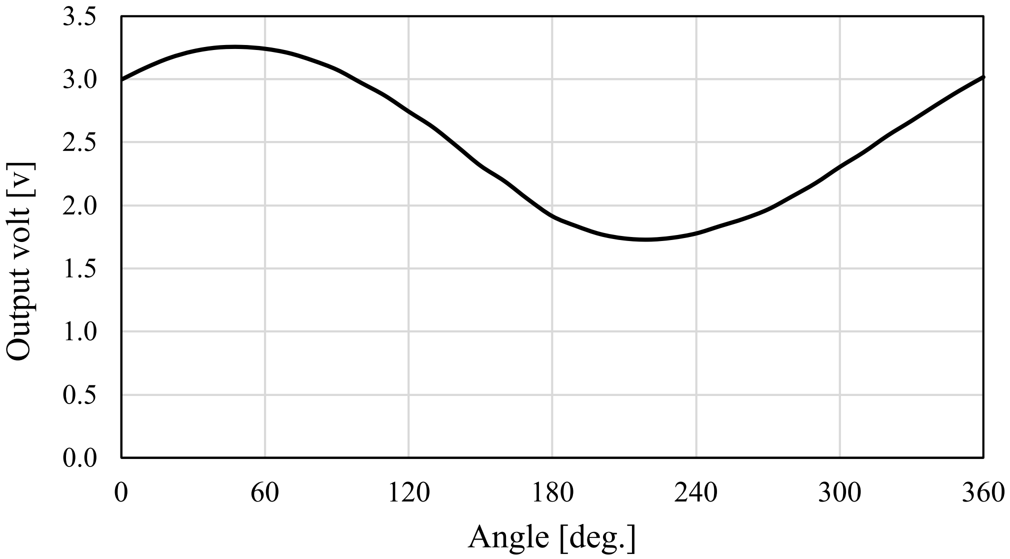

FIGURE 2.15: The output voltage of TMR sensor as the magnet angle changes.

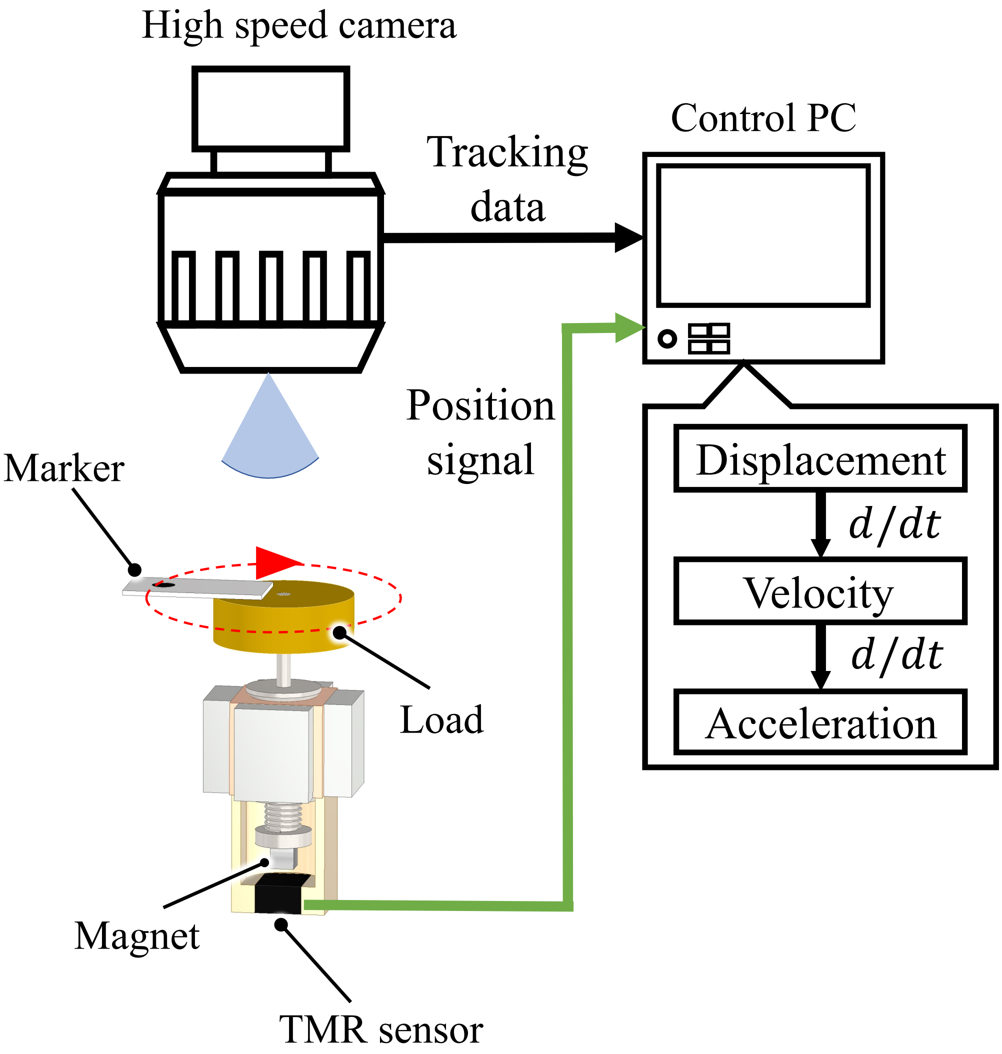
High speed camera
Tracking data
Control PC
Position signal
Marker
Displacement
d/dt
Velocity
d/dt
Acceleration
Load
Magnet
TMR sensor

FIGURE 2.16: Illustration of motor's angular velocity measured by the TMR sensor and by the high-speed camera simultaneously

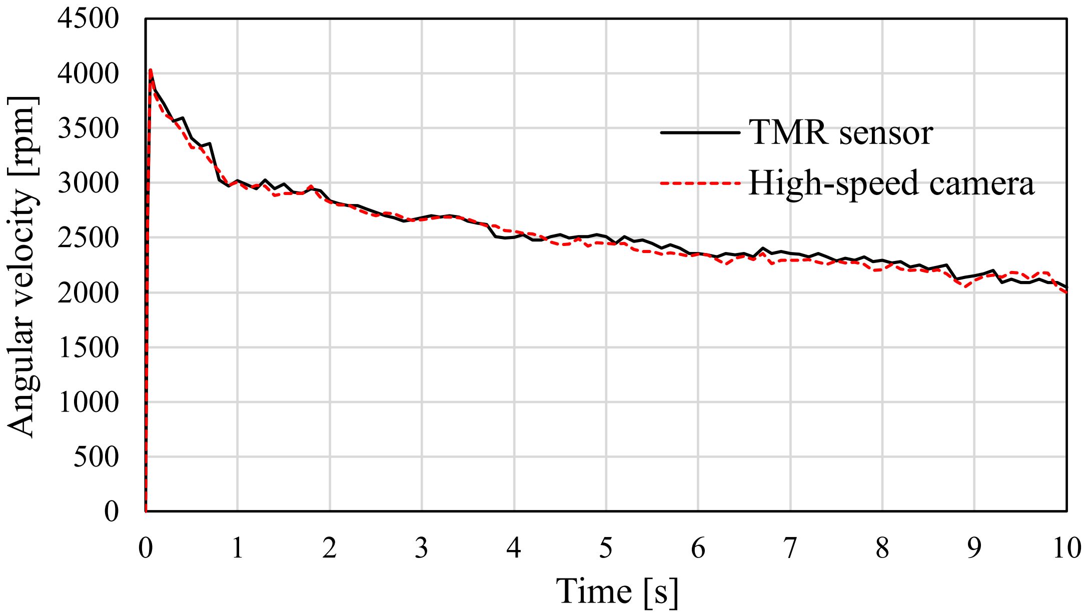

FIGURE 2.17: The steady-state error of the micro-ultrasonic motor caused by the temperature rise. The output of the TMR sensor (internal sensor) is accorded to that of the high-speed camera (external sensor).

2.8 Experiments

2.8.1 Experimental Setup

Fig. 2.18 shows the block diagram of the experimental setup to validate the control structure. The setup consists of the motor, the sensor, the motor driver, and the controller. In general, waveform generators can be controlled by communication with other external devices, but the response time is more than 10 ms. To obtain a quick response, a multichannel direct digital synthesis (DDS) board (AD 9959, Analog Devices Corp., USA) is employed to generate input signals. This board has four channels at up to 500 MSPS, and all of the channels can independently control the amplitude, the frequency, and the phase. The response time to set the output of the board is measured as 0.15 ms, which minimizes the delay time imposed by the system dynamics. The output voltages from the DDS board are amplified by power amplifiers (BA4825, NF Corp.), and the resultant voltages are applied to the motor. The microcontroller (Arduino Uno, Arduino Co., Italy) receives the feedback signal from the sensor and then sends it to MATLAB Simulink program on the PC where all ESC steps are applied. The updated driving frequency f_{input} is then sent back to the microcontroller that, in turn, forwarded to the DDS board. All of the data are stored in the PC memory for analysis. As the speed sensor operates near the high operating frequency of the motor, a low-pass filter is integrated into the system to remove any measuring noises. The cutoff frequency of the filter is higher than the perturbed frequency ω_p to not affect the measured data.

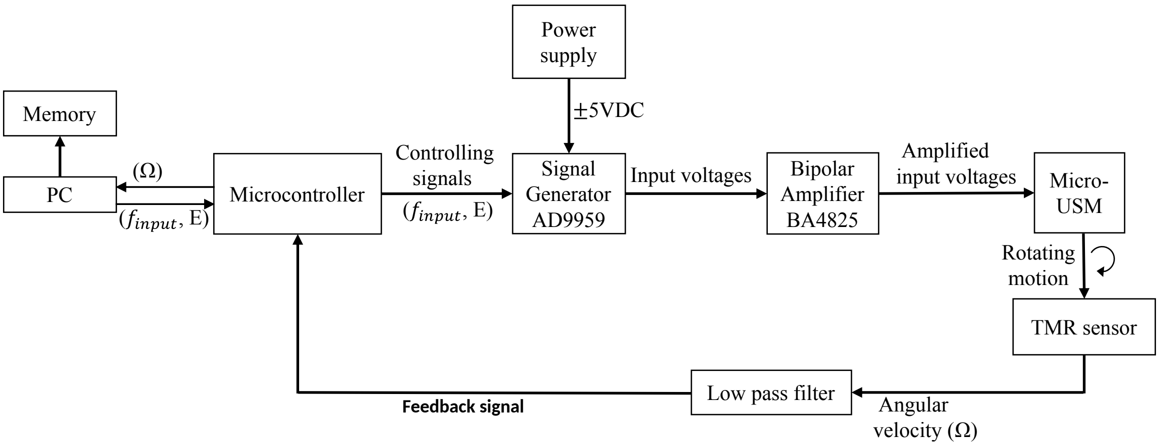
Power supply
±5VDC
Memory
PC
(Ω)
(f_{input}, E)
Microcontroller
Controlling signals
(f_{input}, E)
Signal Generator AD9959
Input voltages
Bipolar Amplifier BA4825
Amplified input voltages
Micro-USM
Rotating motion
TMR sensor
Low pass filter
Angular velocity (Ω)
Feedback signal

FIGURE 2.18: The block diagram of the speed control system for the micro-ultrasonic motor.

2.8.2 Experimental Results

Two experiments are demonstrated to show the effectiveness and robustness of the ESC under continuous operation.

2.8.2.1 Constant Speed Experiment

The main objective is to remove the steady-state error and obtain a stable angular velocity. In this experiment, the ESC is applied to the micro-ultrasonic motor under the same operating condition as the experiment for the velocity-frequency characteristic (Fig. 2.8). We set the initial driving frequency equal to the natural frequency of the stator (f_n = 525 kHz). Fig. 2.19(a) shows the steady-state response when the motor operates continuously for 10 seconds. The dotted line is the reference determined by the steady-state angular velocity measured in Fig. 2.8, whereas the solid line is the actual speed. The motor accelerates to the peak speed in 50 ms and then stabilizes at around 3800 rpm for a period of 10 s. If we compare the response of the motor in Fig. 2.19(a) to that of Fig. 2.17, it is clearly noticeable how the ESC controller minimizes the steady-state error over the operating time. To stabilize the angular velocity, the ESC localizes the natural frequency of the assembled motor (f_n = 528 kHz) after a few iterations, and it continuously sweeps to find the optimum frequency as shown in Fig. 2.19(b). The optimum driving frequency shifts downward with time. Fig. 2.19(c) shows the temperature variation of the stator during the motion while its initial temperature was recorded at 25° C. Although the increase in the temperature (ΔT = 14° C) is larger than that in the experiment for modeling the temperature-frequency curve (Fig. 2.9), the model works well to obtain the stable angular velocity in ESC.

In the view of the energy consumption, it is important to know how the input power behaves during the control. The electrical input power is measured as the product of the input voltages,

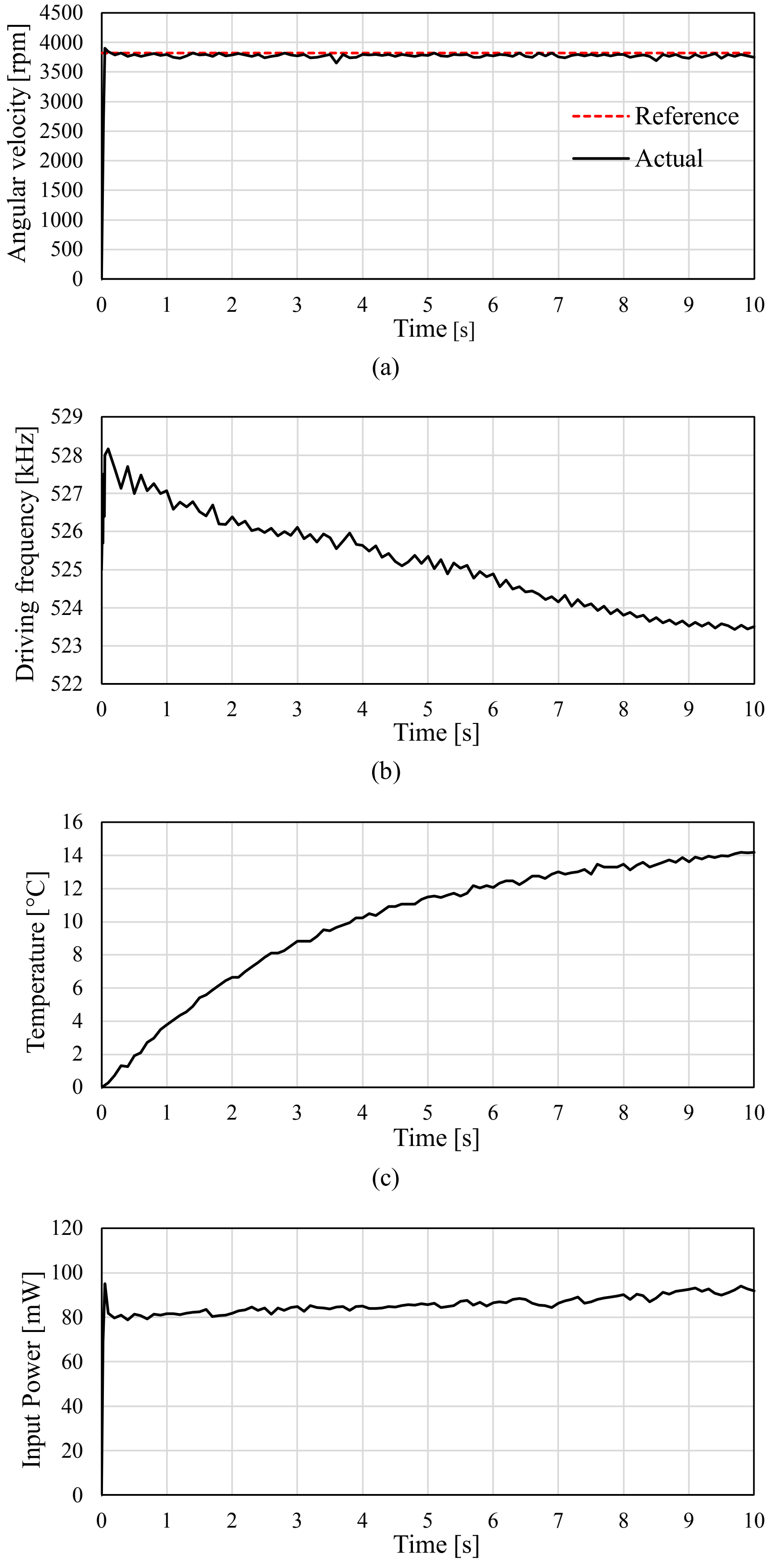

(a)

(b)

(c)

(d)

FIGURE 2.19: Experimental results when ESC is applied to the micro-ultrasonic motor's closed-loop system: (a) The angular velocity, (b) the driving frequency, (c) temperature variation of the stator, and (d) the associated input power.

the current, and the power factor. The induced current is measured for one of the four lines driving the motor; we assume that all the lines flow the same current for computation. Under a constant input voltage, the current supplied to the motor and the power factor are measured by a current probe (CT2, Tektronix Corp., Oregon, USA), and a lock-in amplifier (LI5655, NF Corp., Yokohama, Japan), respectively. Fig. 2.19(d) shows the electric input power to the motor; It peaks at the transient state, stables at the steady state, and then increases gradually in response to the thermal power losses. Similarly, the energy efficiency of the motor can be calculated based on the ratio of the mechanical output to the electrical input power. The mechanical output power is computed as the product of torque and angular velocity. The torque can be obtained from the angular acceleration and moment of inertia at the initial time. The efficiency records a maximum value of 6.3% at the steady-state at the first period of the motion and gradually decreases to 5.1% at 10 s.

2.8.2.2 Variable Speed Experiment

In case the manipulated valuable is only the driving frequency, the applicable range of the ESC is limited; Therefore, another control parameter is added for further control applications. Using the voltage control is suitable to offer a wide range of speeds. In this subsection, the motor follows variable input signals of the angular velocity. To follow the variable signals, we add another external voltage control loop (controlled by a PID controller) besides the ESC internal control loop. The PID controller manipulates the input volts which are proportional to the angular velocity in a roughly linear layout. The PID controller was designed and tuned using the online closed-loop auto-tuning toolbox of the MATLAB Simulink program. By executing a trigger test into the controller output, the frequency response of the system can be estimated. The controller's gains are tuned at K_p = 0.03613, K_i = 6.13, and K_d = 0.00103. In such an arrangement, the signal of the TMR sensor is fed back to both controllers simultaneously. Due to deadzone issues[42], the minimum saturation level for PID is set to 60 $\mathrm{V_{p-p}}$ while the maximum is set to 120 $\mathrm{V_{p-p}}$ to avoid excessive heating.

Stepwise Square Wave Command: In this experiment, the motor follows a series of stepwise commands of the angular velocity. Fig. 2.20(a) shows that both controllers drive the motor to match the reference speed without overshoot and steady-state error. The dotted line indicates the input command reference while the solid line refers to the actual motor speed. A slight variation in the steady-state speed is observed due to the perturbed signal of the ESC, although the speed fluctuation is minimized after the transient state. Fig. 2.20(b) magnifies a step response. It demonstrates a good agreement between the reference and measured trajectories. The steady-state speed overlaps the reference, except for the transient time.

In this experiment, the driving frequency is initially set at $f_n = 525$ kHz and we program the ESC to restore this value as the motor stops during the operation. Fig. 2.20(c) shows the optimum driving frequency localized by ESC while the motor follows the stepwise input. The frequency downshifts at a proportional rate to the angular velocity. The result means that manipulating the voltage amplitude is independent from the frequency shift.

Sinusoidal Wave and Triangular Wave Commands: Other variable input commands are also tested to verify the feasibility of using the dual-mode control structure. A sine wave command of 60 Hz frequency and 500 rpm amplitude is initially evaluated, then a triangular wave command of 100 Hz frequency and 2000 rpm peak-to-peak value is examined. Each commanded input is executed continuously for 5 seconds. Due to the deadzone limitation of ultrasonic motors, we set the midline of the sine wave input to be at 2500 rpm, while the lower margin of the triangular wave is set to 1000 rpm. Fig. 2.21(a) and (b) show the speed response of the motor to match the two prescribed input commands. In both experiments, the motor could track the commanded given inputs efficiently although some speed fluctuations are recorded. Despite the controller's stability, some overshoot can be observed too at the edges occasionally.

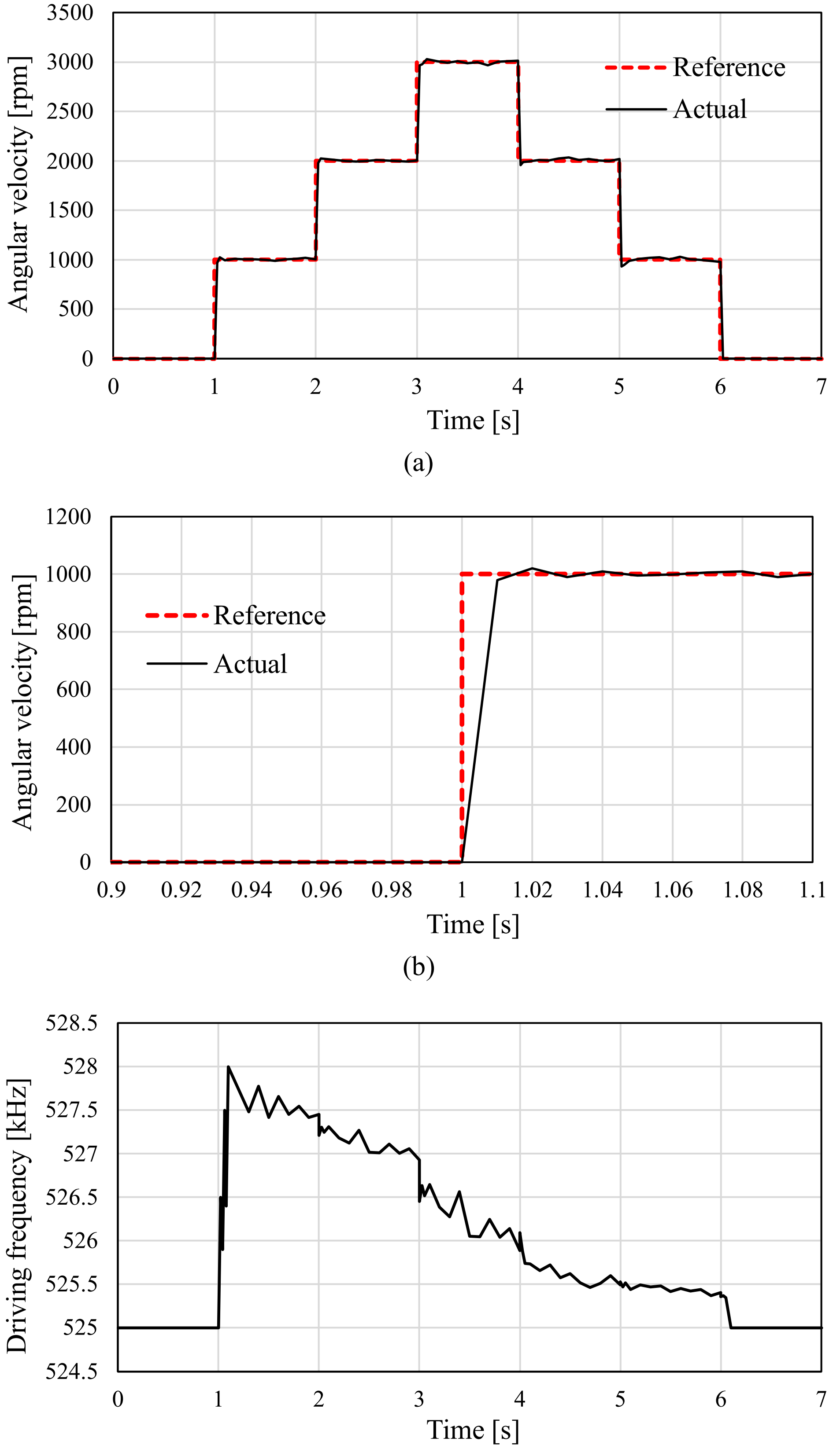

(c)

FIGURE 2.20: Experimental results when two controller loops are applied for tracking step-wise commands. The ECS is controlling the driving frequency while the input voltages are controlled by a PID controller. (a) Comparison between the reference and the actual angular velocity, (b) the transient response, and (c) the driving frequency localized by ESC.

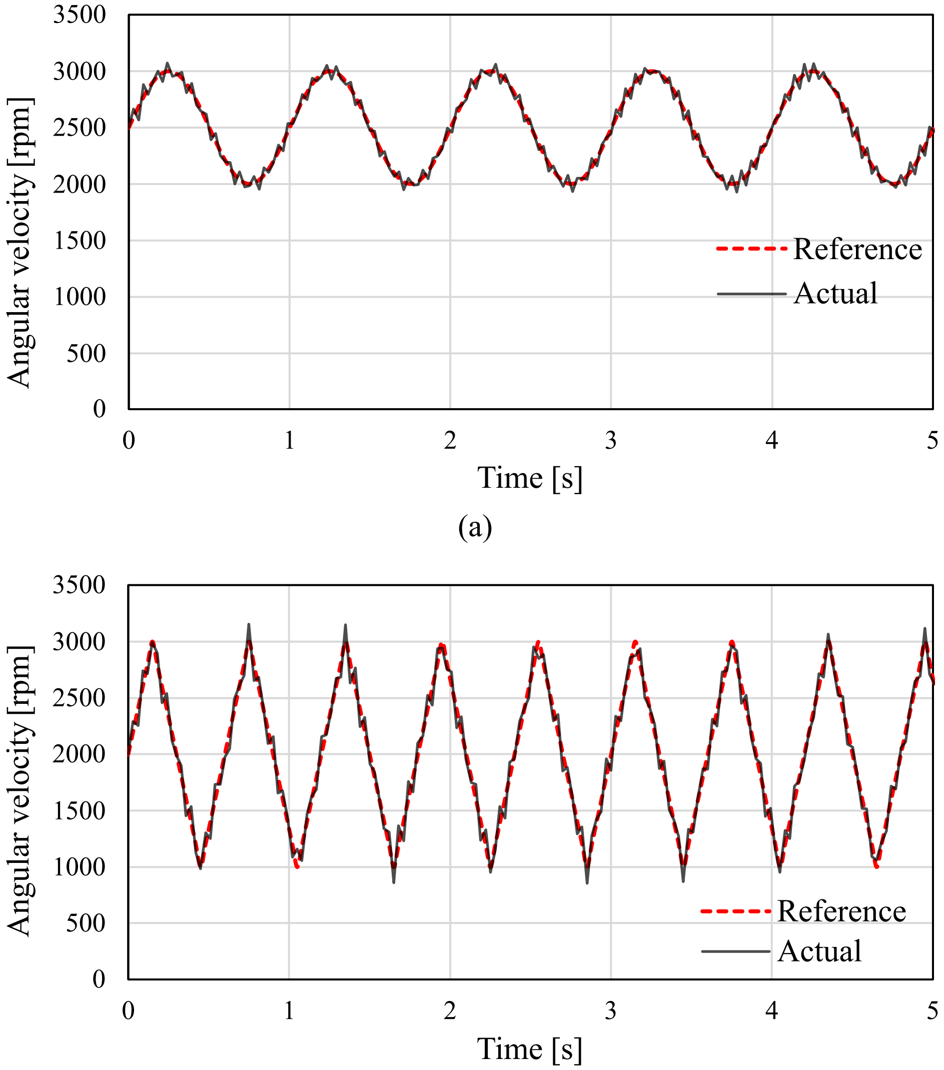

(a)

(b)

FIGURE 2.21: Speed response by dual control scheme (ESC and PID) under variable speed commands. (a) Sinusoidal wave command input. (b) Triangular wave command input.

2.9 Performance Evaluation

Finally, a typical benchmark is to compare the performance of the proposed rotary actuator-sensor system with similar prototypes previously reported by other researchers. Actually, only a few comparable-sized motor-sensor systems have been shown in the past 10 years. For example, a miniature ultrasonic motor that employs a magnetic sensor was reported in [85]. It is as small as our system, but it appears that this study has not been continued afterward. Another prototype that employs the deformation of one piezoelectric plate as the feedback sensing element was reported in [86]. Seeing the motor market, several commercial products (e.g., M3-RS, Newscale

TABLE 2.3: Comparison between the proposed rotary actuator-sensor system with similar prototypes.

Reference	Size [mm^3]	Feedback sensor	Torque [μNm]	Op. frequency [kHz]	Op. volt [V_{p-p}]	Max. angular velocity [rpm]
T. Kanda et al. [85]	$2.6\times 2.6 \times 9.6$	Magnetic sensor	2.87	30.6	60	552
S. Toyama et al. [86]	$3\times 3 \times 8.4$	Deformation of one PZT plate	52	250.75	180	3300
Squiggle motor (M3-RS) [87]	$12 \times 22 \times 16$*	Magnetic sensor	40	N/A	N/A	183
This work	$3.2\times 3.2 \times 5$	Magnetic sensor	60	528	100	3800

*Including a built-in motor driver and a controller

Tech. ltd., USA) are released for applications. Although this system contains a motor driver in addition to the actuator and sensor, it still results in a compact size [87].

Table 2.3 summarizes the size, feedback sensing technique, stall torque, operating frequency, operating volts, and the maximum angular velocity of the motors. With a more compact size, Table 2.3 demonstrates the superiority of the proposed system over all comparable prototypes in terms of overall size, stall torque, and maximum angular velocity.

2.10 Conclusion

In this chapter, we address the steady-state error of the micro-ultrasonic motor. For that, a mathematical model was then derived from scratch to justify the hypothesis of the time-varying behavior of the micro-ultrasonic motor. That was followed by several experiments to prove the effectiveness of temperature variations on the performance and dynamic characteristics of ultrasonic motors experimentally. A model-free real-time adaptive controller that can coop efficiently with that problem is then presented. The controller is based on the extremum-seeking controller approach that features design simplicity and a high convergence rate. To implement the proposed controller, we constructed the smallest motor-senor system that consists of a 2 mm size ultrasonic motor, a tiny TMR sensor, and a tiny magnet. The new feedback system is evaluated to confirm its robustness, then the proposed controller is tested as the motor operates at its maximum velocity for 10 seconds as the controller continuously localizes the optimum driving frequency. When combined with an external voltage control loop, the applicable range of the ESC was extended and the motor could follow prescribed increasing or decreasing variable commanded angular velocities efficiently.

Final results have revealed that despite running at a constant angular velocity, other associated problems in micro ultrasonic motors such as efficiency improvement are still not fully addressed. Still, we have achieved one step ahead in fully controlling the nonlinear characteristics of ultrasonic motors. More work is still needed to address these challenges.

Chapter 3

In-Pipe Insect-Scale Robot

Millimeter-scale or sub-gram microrobots (the so-called insect-scale microrobots) enable access in narrow and complex environments such as the inside of pipes, gastrointestinal tracts, and disaster-relief sites. However, the mobility of these microrobots is yet to reach that observed in similar-sized biological creatures. For such scale, researchers mimic the locomotion pattern of biological creatures as they represent a truly successful example. In the few years, a vast number of insect-scale microrobots have been proposed to approach and surpass the level of biological systems [88]. In these, the great majority of insect-scale microrobots are flying vehicles with flapping wings [89–92]. With the emergence of these flying robots, new technologies, such as newly designed actuators and additive fabrication, have brought rapid advancement in the field of microrobotics [93, 94]. Compared to the flying kind, ground-based microrobots are still few, although they also have much potential for a wide range of applications.

3.1 Ground-based Microrobots

To design an insect-scale inspection robot, we must screen previously reported prototypes to fade their drawbacks. Seeing the existing literature, we can classify ground-based microrobots into two types: crawling legs [95–99] and rolling wheels [100–102]. Large-sized legged robots can provide good mobility in rough terrains, where existing vehicles cannot go, but the mobility of millimeter-scale legged robots is limited due to the narrow range of motion of crawling legs. Continuously rotating wheels excel on flat surfaces at a macro-scale. Large-sized wheel systems can be constructed by conventional technologies, but the miniaturization of wheel systems requires novel technologies such as small actuators, fabrications, and integration systems. For example, one of the smallest wheel-based microrobots, with dimensions of 18 mm × 8 mm × 8 mm, employs a new linear electromagnetic actuator using a ratchet mechanism [102]. It can move on a flat surface at a speed more than its body length per second; however, the tiny actuator cannot generate sufficiently large torque for carrying payloads or climbing inclines.

One reason for wheel-based microrobots to be few in number is the lack of microactuators with high torque density. To develop practical micromotors, various prototypes have been proposed using several driving principles; mainly, electrostatic force, electromagnetic force, and piezoelectric effect. In these, piezoelectric rotary ultrasonic motors are one of the most practical actuators because of their high torque density and simple structure [103–106]. (Incidentally, millimeter-scale ultrasonic motors have been implemented to limited spaces inside watches [107] and camera lenses [108].) Miniature ultrasonic motors have shown great performance [106], but they have not been employed in any millimeter-scale robot yet. The primary focus for all of these microrobots was the development of the mechanisms and actuators. The integration of sensing and control for a robot that ‘senses, thinks, and acts’ was largely neglected in these first prototypes.

3.2 Design and Prototype

Locomotion in narrow pipes is challenging for robots because of the unique geometrical environment. To satisfy the requirements of in-pipe navigation, the robot must comply with a narrow body design, bidirectional powerful locomotion, and a robust holding force mechanism.

3.2.1 Micro-geared Ultrasonic Motor

One of the main problems in the previously reported insect-scale robot prototypes was the lack of adequate power; therefore, we plan to combine the micro-ultrasonic motor with a planetary gearbox to boost the locomotion by means of high-torque density actuators.

3.2.1.1 Design of Micro-geared Ultrasonic Motor

The planetary gear train is one of the most commonly used gear systems. It is composed of a sun gear connected to an input axis, planet gears mounted on a carrier, and an annular gear meshed with the planets. The carrier functions as an output shaft of the current stage and transfers output torque to the next stage. Using multiple stages, the planetary gear train has a large reduction ratio and high torque-to-weight ratio. Miniaturization of those gear components is possible by injection molding. The most often used microgears are plastic watch gears, but the plastic materials lack the stiffness needed to transfer large output torque. Instead of plastics, metallic glass, a solid amorphous metal with a disordered atomic-scale structure, enables injection molding in

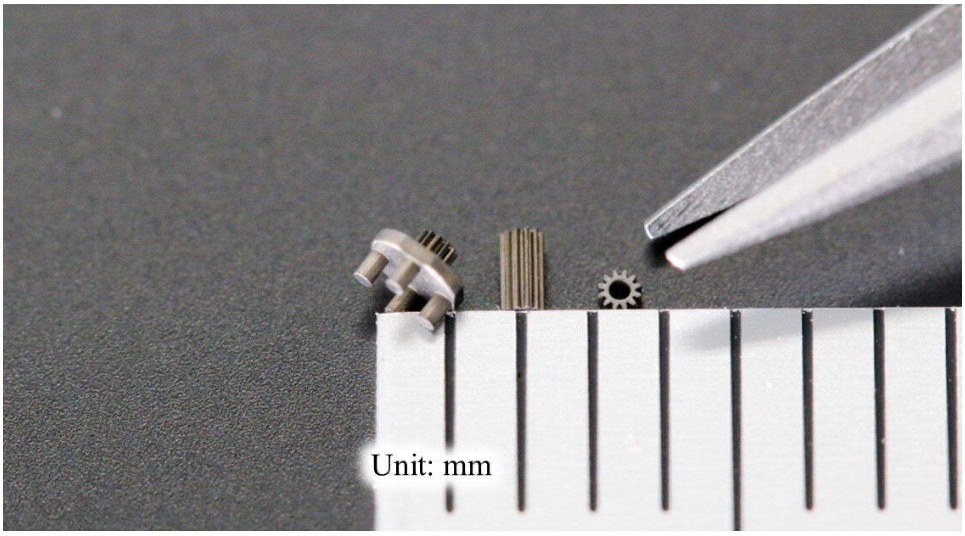

(a)

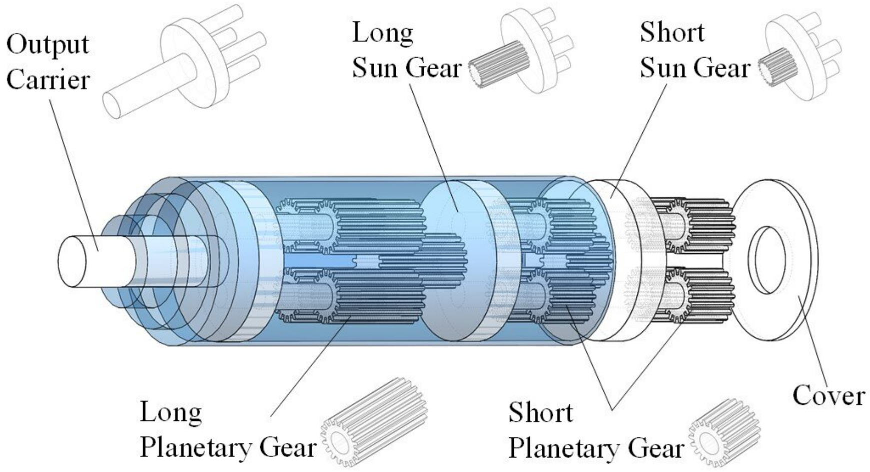
Output
Carrier
Long
Sun Gear
Short
Sun Gear
Long
Planetary Gear
Short
Planetary Gear
Cover

(b)

FIGURE 3.1: (a) Example of the microgears made of metallic glass. (b) The components and the structure of the micro planetary gear train: the gear system with a ratio of 64 uses an output shaft, four long planetary gears, a long sun gear, 8 short planetary gears, and a short sun gear.

a similar manner as plastic gears because of its high casting quality [109]. The resulting gears can have high stiffness and durability, the same as that shown by gears made of metals, to make a microrobot powerful.

Fig. 3.1(a) shows the components of a micro planetary gear train: a sun gear, a planet gear, and a carrier, all of which are made of metallic glass ($Zr_{55}Cu_{30}Al_{10}Ni_5$ at %). Fig. 3.1(b) shows the structure of the micro planetary gear train, wherein all components are assembled. This gear system has three stages, and four small planet gears are attached to each stage for each sun gear.

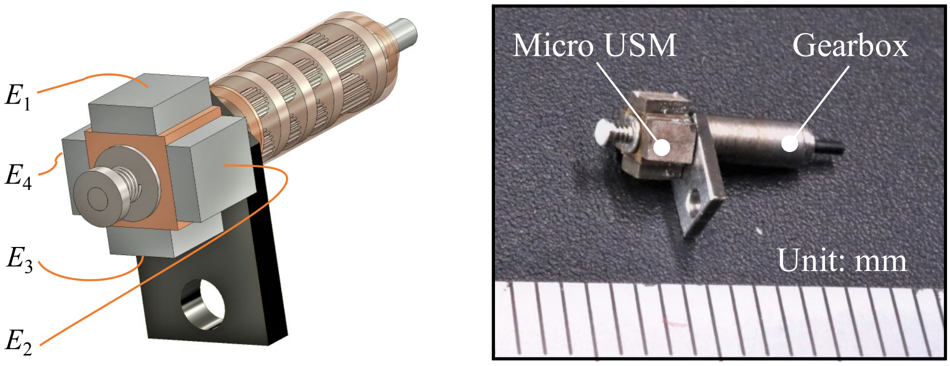

FIGURE 3.2: Design of the micro-geared ultrasonic motor, a metallic flange fixes the motor and the planetary gear train.

One stage has a gear ratio of 1/4 so that the gear ratio of the entire system becomes $1/4^3 = 1/64$. The resulting dimensions of this micro planetary gear train are 2 mm outer diameter and 7 mm length, including the length of the output shaft outside the gearbox, and it weighs 78.8 mg.

Fig. 3.2 shows the design of the assembled micro-geared ultrasonic motor. A flange fixes the micro-motor with a pinion gear and micro planetary gear train while the input voltages, E_1 to E_4, are applied to the four piezoelectric elements through wires of a diameter of 0.1 mm. The prototype of a micro-geared ultrasonic motor was also presented in Fig. 3.2, its total length of which is 11.2 mm.

3.2.1.2 Evaluation of Micro-geared Ultrasonic Motor

The torque–speed characteristic is one of the important data to show how much performance the geared motor produces. This characteristic can be evaluated by measuring the angular velocity when a load torque is applied against the rotational direction of the rotor. Fig. 3.3 shows the experimental setup used to change the amount of load torque. The output shaft from the micro-geared ultrasonic motor is connected to a pulley (with a radius of 4 mm) by a miniature coupling as shown in the detailed view of Fig. 3.3. Both sides of the pulley are supported by bearings, and only load torque is applied to the output shaft. In addition, multiple weights varying from 5 to 25g are attached to the pulley as a payload by a string. Load torque is calculated as the product of the pulley radius and the weight amount that the motor can lift. When the rotor spins, the output axis rolls the string and lifts the payload through the pulley. During this experiment, the amplitude and frequency of the applied voltages are constant (A_E = 80 $\mathrm{V}_{\mathrm{p-p}}$ and f_E = 525 kHz). Here, this frequency has been adjusted to maximize angular velocity.

Fig. 3.4 shows the relationship between load torque and angular velocity when the load torque varies from 0 to 1 mNm. The motor smoothly reaches a steady-state angular velocity at a load torque from 0.2 to 0.6 mNm. At higher load torques (0.8-1.0 mNm), the continuous

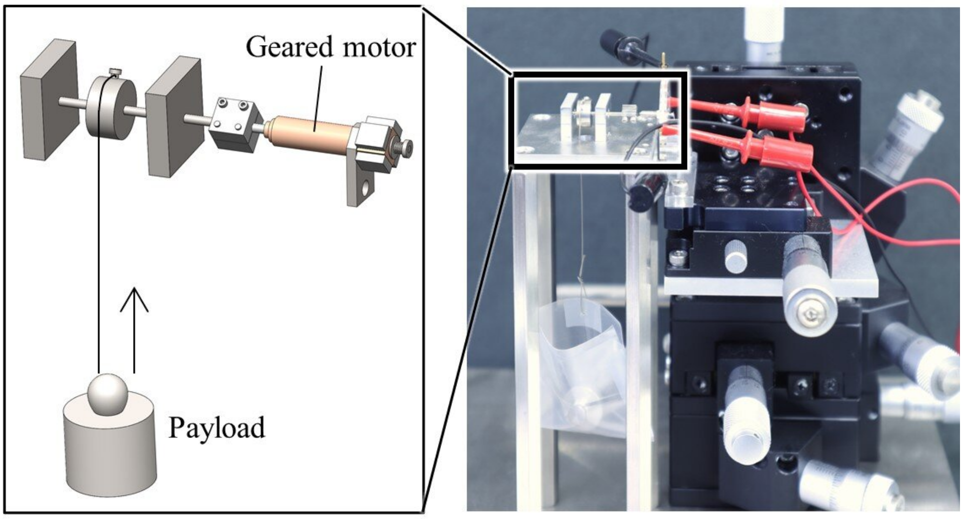

FIGURE 3.3: Experimental setup to examine the relationship between the load torque and the angular velocity. The micro-geared ultrasonic motor is coupled to the pulley that lifts a payload. While the load weight is attached to the pulley, a load torque is given to the motor's output shaft.

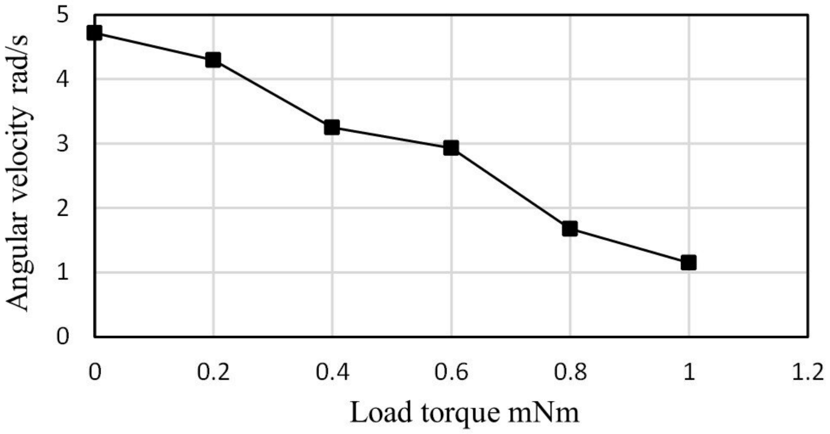

FIGURE 3.4: Relationship between the load torque and the angular velocity.

driving time of rotation shortens, and the number of times that the motor cannot start spinning increases. This is because of the unstable static friction behavior of the gears and the instability of torque generated from the micro ultrasonic motor.

Considering the case of a load torque of 0.5 mNm, wheels with a radius of 2 mm can generate 250 mN force tangentially. This value is sufficient to operate insect-scale microrobots and is the highest torque generated in existing millimeter-scale microrobots.

3.2.2 Prototype Design

To enlarge the working domain to a wide range of pipeline diameters, the proposed in-pipe robot is designed as an articulated robot that consists of 2 links connected by a pivot joint. The design was mainly inspired to imitate the motion of caterpillars. The pivot joint allows the robot to extend and flex as shown in Fig. 3.5(a). The robot has 6 wheels, a pair of active wheels at each end to drive the robot, and 2 passive wheels at the pivot joint. The active wheels are driven by two micro-geared ultrasonic motors to make mobility more powerful. The geared motor is fixed by a screw with a diameter of 1 mm to one side of the chassis through the flange. After the geared motor starts rotating, the driving force generated from the geared motor is transferred to the front axle via a pair of bevel gears. A shaft with an outer diameter of 0.5 mm and length of 10 mm is used as the axle. We select the normal design of the bevel gears and reduce the size of their CAD model to be suited for the microrobot. The diameter of the pitch circle is set to 2 mm, and the number of gear teeth is set to eight. The passive wheels are fitted to the joint through micro-bearings; thus, they are free to rotate. Incidentally, they are the smallest commercially available ball bearings (manufactured by Minebea Co. Ltd., Japan), having an outer diameter of 1.5 mm, an inner diameter of 0.5 mm, and a depth of 0.6 mm. To extend the robot, stop a pair of active wheels and drive the other one far from the center. As the motors rotate in both directions, the opposite maneuver is performed to flex. When fully extended, the length of the robot is 40 mm, and its height is 7 mm. When fully contracted, the length of the robot is 15 mm, and its height is 22 mm if we take into account the passive tires' height. The structure is also narrow as the width measures only 10 mm.

Another ultrasonic motor (USM) is also connected to the pivot joint to control the motion of the pivot joint by using two spur gears with a gear ratio of 1/2. All the wheels are 7 mm in diameter and are made from soft rubber. The robot's links, wheels hub, and gears are printed by a 3D multijet printer that stacks UV-curable resin layers one by one using an inkjet (ProJet 3510HD Plus, 3D Systems Co., USA). The real prototype is presented in Fig. 3.5(b).

The robot is connected to the motor drivers via a tether, the diameter of the wires is 0.1 mm to reduce weight and resistance as possible. The wires act as a lifeline rescue method to safely retrieve the robot from the pipelines in emergency situations.

3.3 Performance Evaluation

3.3.1 Mobility Characteristics

Locomotion performance depends on the characteristics of the proposed insect-scale wheeled robot. The fundamental characteristic of the robot on a horizontal plane is examined by changing

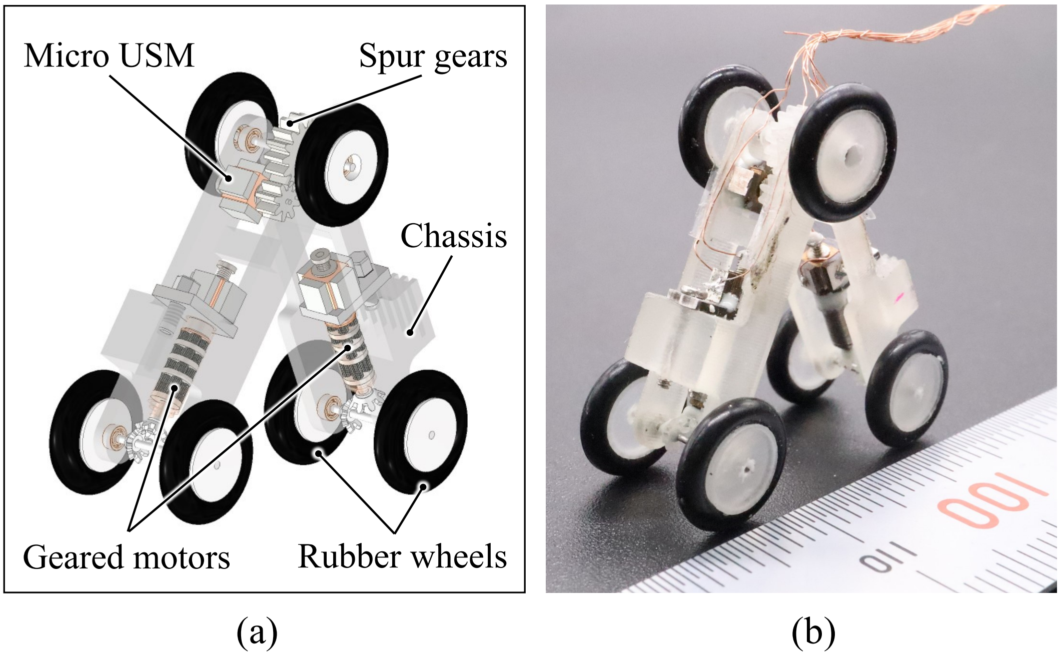

FIGURE 3.5: (a) CAD design of the insect-scale inspection robot, two micro-geared motors drive the front and rear wheels using bevel gears. Another micro-motor is controlling the resistance of the pivot joint, and it is connected to the joint using 2 spur gears. (b) Prototype of the insect-scale inspection robot.

the amplitude and frequency of the input voltage applied to the micro-ultrasonic motors. (How these parameters affect the performance of the micro-ultrasonic motor is explained in Chapter 2.) Knowing these behaviors is important for controlling the posture of the robot. To reduce the slip of the wheels, the road is covered with a silicone rubber sheet with a static friction coefficient of 0.97. The variation of the robot's speed with the input voltages and frequency on the horizontal plane are shown in Figs. 3.6(a) and (b), respectively. The robot starts to move at more than 40 $\mathrm{V_{p-p}}$ and increases the speed roughly proportional to the voltage (Fig. 3.6(a)). When the frequency is manipulated, the speed peaks at the resonant frequency and gradually decreases far from the resonance (Fig. 3.6(b)). A peak speed of 12.3 mm/s is obtained when input voltages of A_E = 120 $\mathrm{V_{p-p}}$ and f_E = 523 kHz are applied.

3.3.2 Force Generated by the Robot

In-pipe navigation is considered a challenge for any robot and requires actuators to significantly boost torque to propel the robot against the inner walls. Therefore, the maximum force/torque that the proposed robot can generate is evaluated experimentally. Fig. 3.7 shows that the robot pulls a weight on a horizontal plane. Several weights are attached to the robot and the moving speed is recorded. In the experimental setup, a ruler was attached for the calibration of displacement. For all experiments, the same input voltage of 100 $\mathrm{V_{p-p}}$ is applied. Fig. 3.8 shows the

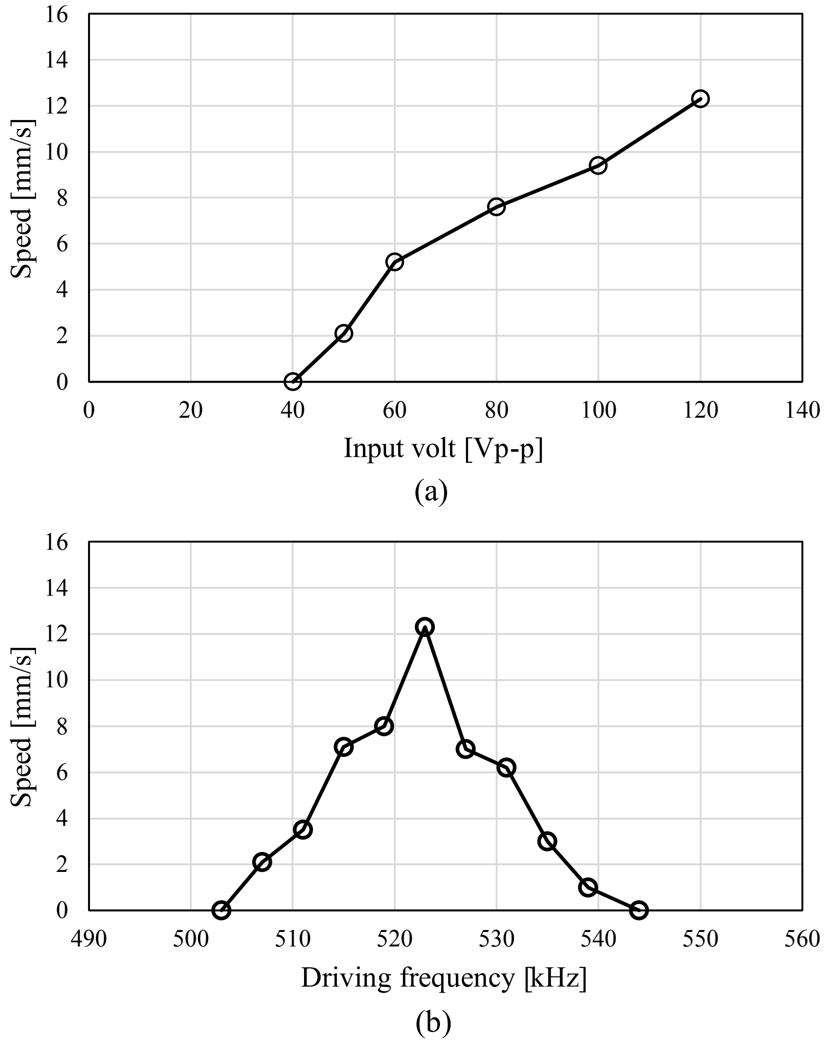

FIGURE 3.6: The relationship between the robot speed and the applied voltages; (a) Speed vs. amplitude and (b) speed vs. frequency.

relationship between the robot's speed and different weights. It shows that the robot pulls 10 g of weight at an average speed of 4 mm/s. At higher loads, the robot tends to lean backward, and the front wheels lose grip. Because the insect scale robot weighs just 1.7 g, it can steadily drag approximately six times its own weight.

3.4 Locomotion Modes

The robot can navigate forward and backward inside the pipeline in 2 mode shapes; an in-line mode and an anti-slip mode. Fig. 3.9(a) shows a comparison between the 2 shape modes. In general, the in-line mode is assigned for simple horizontal pipelines, where traveling speed counts as long as the robot keeps adequate traction with the pipe walls. Herein, the traction between the wheels and the walls is only due to gravity. Anti-slip mode is for navigation through slip-

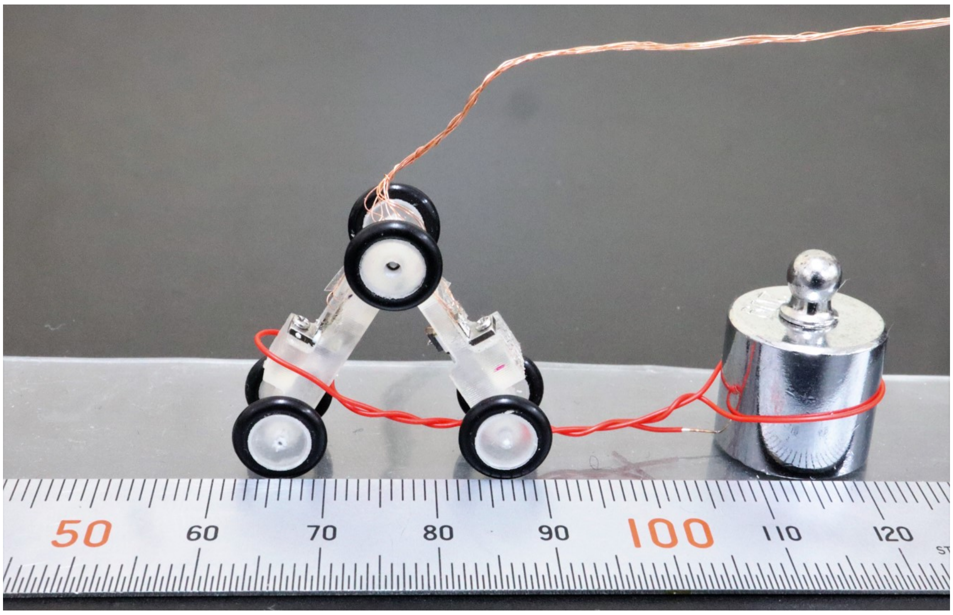

FIGURE 3.7: Motion of the wheeled robot connected to a weight. The robot can drag a weight of 10 g on a surface with a friction coefficient of 0.97.

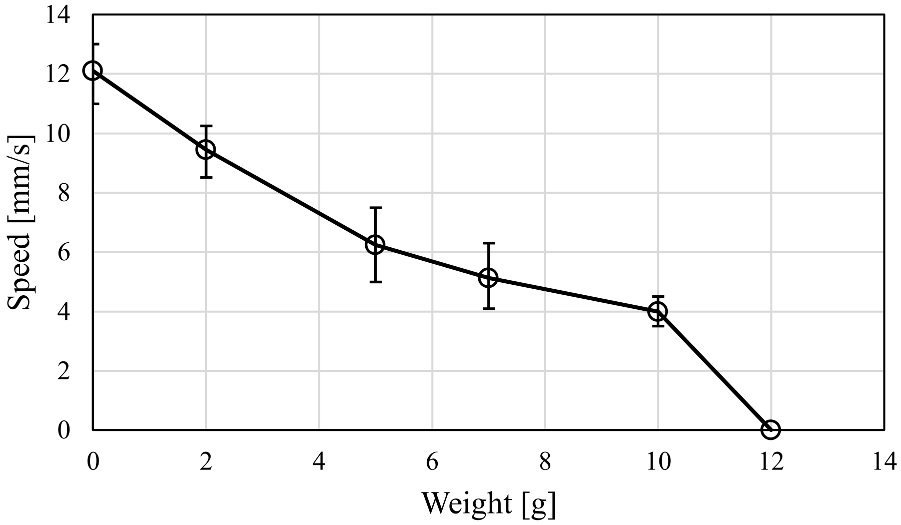

FIGURE 3.8: Change in the speed when the amount of the weight varies. The graph presents the mean, the maximum, and the minimum data for 10 trials.

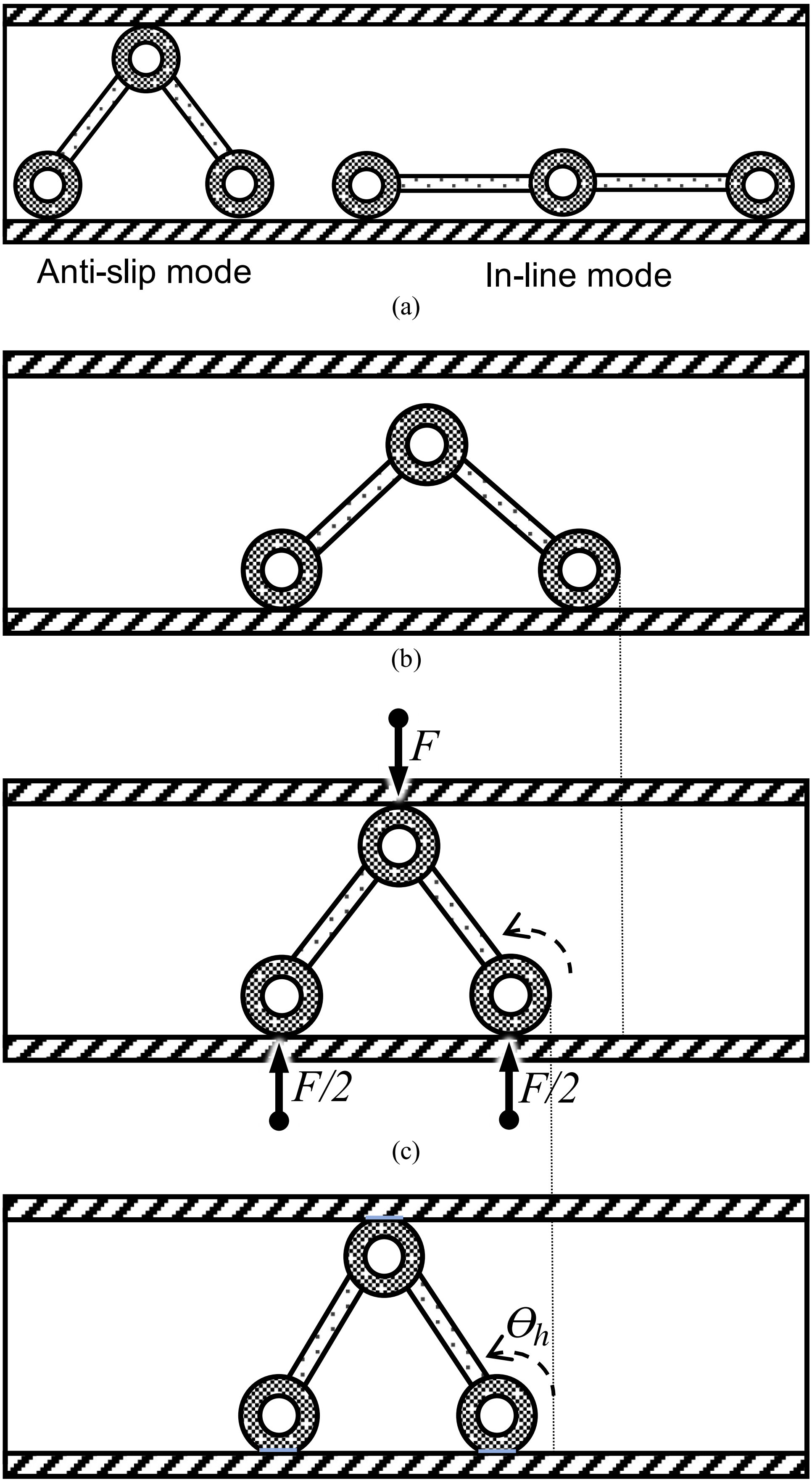
Anti-slip mode
In-line mode
F
F/2
F/2
θ_h

(a)

(b)

(c)

(d)

FIGURE 3.9: (a) Demonstration of the two different shape modes, (b) and (c) Show the transformation strategy to switch from both in-line to anti-slip modes. (d) Presents how the integrated holding force mechanism works.

pery pipelines or vertical ones. In this mode, the robot deploys the holding force mechanism by pressing its passive wheels against the inside pipe wall, which creates an extra traction force between the active rotating wheels and the walls. In other words, the generation of the traction force is based on the robot's layout. Figs. 3.9(b) and (c) show the locomotion pattern to transform from in-line to anti-slip mode. The robot starts by moving its back wheels forward until the passive wheels push the upward pipe wall. Pressing the upper wall with force F increases the normal force between active wheels and the pipeline wall by the same amount, which results in an improvement in traction force. Moreover, as the wheels are made from soft rubbers, rotating the back wheels further ahead is possible to enlarge the traction force and the wheels' contact area profile (Fig. 3.9(d)). For better analysis in the next section, we call that angle a "holding angle" and it is denoted as θ_h. Eventually, the traction force can be adjustable based on pipeline conditions, which comes at the cost of propelling speed.

3.5 Holding Force Mechanism

The holding mechanism is evaluated and tested through a series of experiments to prove its robustness and to determine the applicable operating range in which the robot moves inside a pipeline smoothly. In other words, a too-small traction force cannot retain the contact between the wall and wheels in slippery conditions, and a too-high traction force stops the rotation of wheels.

As it is almost impossible to determine exactly the contact condition (normal force) between the wheels and the inner surface of the pipeline, the traction force can be measured experimentally. The traction force is defined as the friction between the drive wheels and the pipe walls. Fig. 3.10 shows the experimental setup, the pipeline is made from acrylic material with an inner diameter of 22 mm. The experiment procedures are as follows; the robot is initially switched from in-line mode to anti-slip mode until the passive wheels come into contact with the walls of the pipe. The rear wheels are then rotating further ahead at a different angle at a time to increase the traction force. The traction force is measured by pulling the robot with a force gauge until the robot slips forward. Maximum pulled-off force just before detachment is recorded as the traction force. Throughout all the experiments, the same input volt of 100 $\mathrm{V_{p-p}}$ is applied to the geared motors. Fig. 3.11(a) shows the relationship between the holding angle (θ_h) and the traction force. As the angle increases, higher normal forces are generated between active wheels and the inner surface of the pipeline, which leads to a more traction force. To measure the angle of the wheels, we attach a tiny magnet and a rotary angle sensor at the end part of the ultrasonic motor to measure its rotation angle. As the sensor is capable of detecting 360° of rotation angle, the angle of wheels can be identified then as the gearbox ratio is constant. All of the backlash motions of gears are neglected.

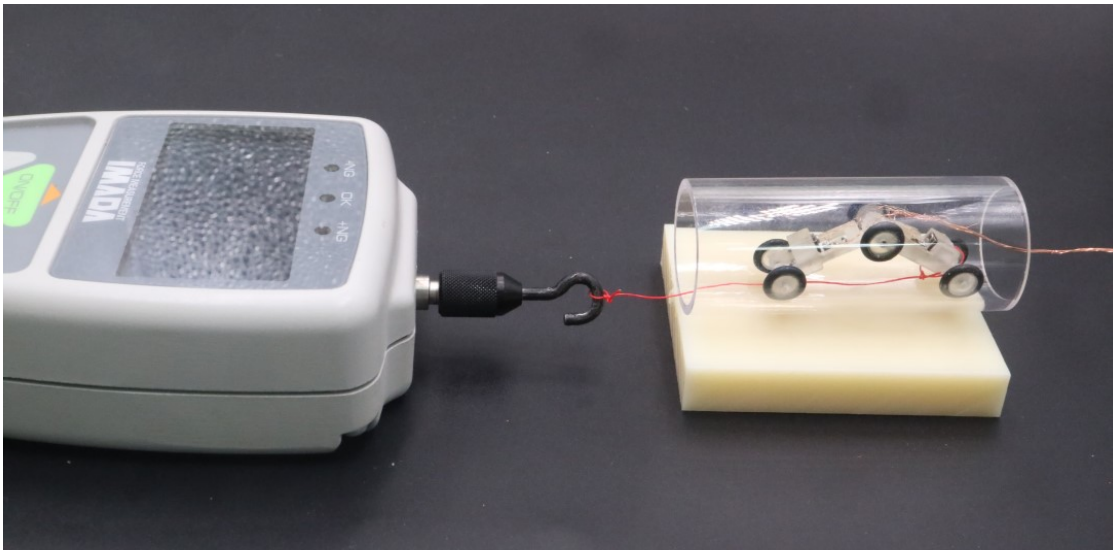

FIGURE 3.10: Evaluation of the traction force for different holding angles (θ_h). After adjusting a different holding angle at a time, the force gauge pulls the robot forward until it slides.

Propelling speed is also important for controlling the posture of the robot inside the pipelines. Therefore, we also measured the propelling speed with different holding angles. For this evaluation, the traction force is set to a new value at a time, then the robot proceeds to move forward with its full power. Fig. 3.11(b) shows the variation of the robot's speed when different holding angles are applied. The robot's speed drops as the traction force increases until it comes to a complete stop when the traction force exceeds the propulsive force.

Considering the results, the holding angle should not exceed 7°, so that the robot can navigate with adequate performance through the pipelines. The high power-to-weight ratio enables additional equipment for exploring missions and inspection tasks to be attached to the robot. The current work is dedicated to the navigation skills of the robot while retaining its holding force.

3.6 Motion Strategy for Complex Pipelines

The pipeline robot with this new configuration not only has the same features as existing pipeline robots but also has better environmental adaptability. This section is devoted to describing the active motion strategies used for increasing pipe-passing capabilities by navigating complex pipeline systems such as a funnel segment pipeline and a 90° elbow connection as shown in Figs. 3.12(a) and (b).

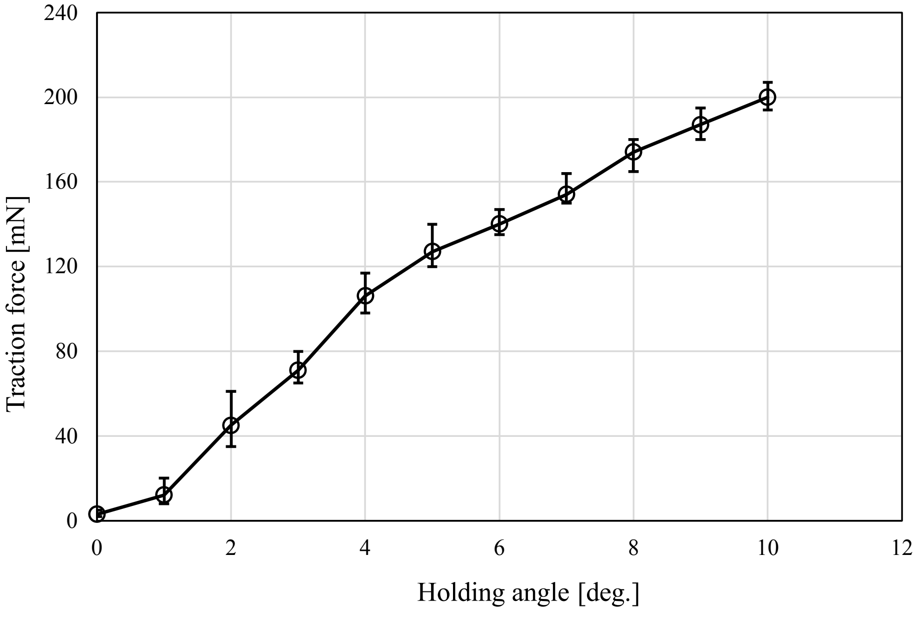

(a)

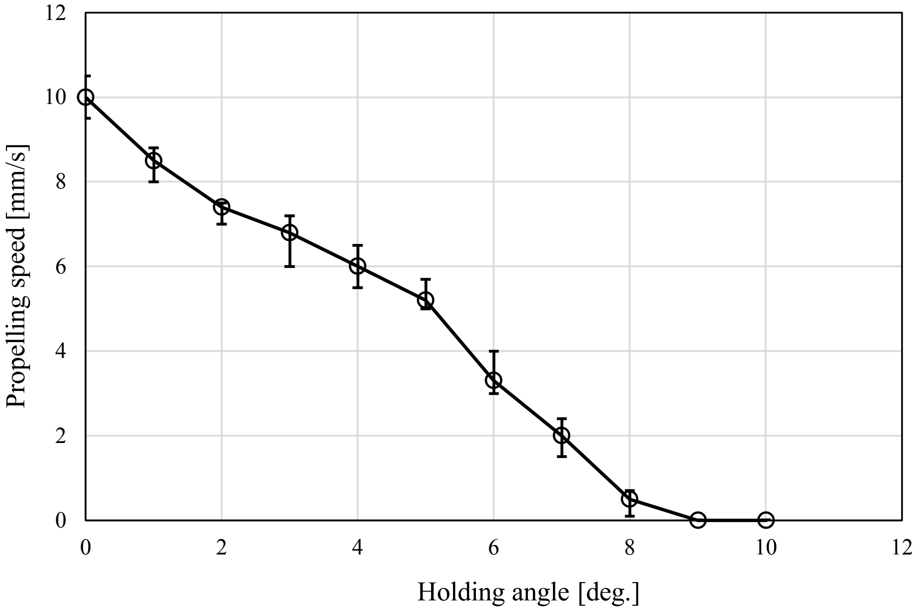

(b)

FIGURE 3.11: (a) The relationship between the holding angle and the traction force, and (b) Change in the speed when the holding angle varies.

3.6.1 Navigation in a Funnel Segment

A funnel segment is used to connect pipelines with different diameters (d_i and d_o) as indicated in Fig. 3.12(a). Navigation through segments where the pipeline diameter is continuously changing is very tricky especially when the anti-slip mode is deployed. The robot must continuously change its geometrical configuration while retaining the traction force. Fig. 3.13 shows the motion strategy to navigate in funnel segments. The strategy consists of 2 main stages; transformation to anti-slip mode to deploy the holding force mechanism, and continuously adapting the robot configuration to maintain the traction force. This strategy allows the robot to move in funnel segments whether the diameter is expanded or contracted. Detection of diameter change is conducted by comparing the rotational speed of the three ultrasonic motors. After the deployment of the holding force mechanism to a predefined adjustment, the controller periodically increases the rotational speed of the rear wheels slightly while monitoring the movement of the pivot joint. If the motor connected to the joint rotates, that indicates that a new space starts to develop above the passive wheels, which refers to a diameter expansion case. In such a case, the controller will drive the back wheels only until the traction force is retrieved. On the other hand, the diameter contraction scenario can be detected by comparing the rotational speed of both the front and back motors. In other words, if the front and back motors start to decelerate simultaneously, it is an indication of a diameter contraction case where the robot will eventually stick in the narrower diameter with the current configuration. The controller will react by accelerating the front wheels slightly before proceeding with moving both wheels at the same speed. This approach solves the jamming problem while retaining the traction force.

3.6.2 Overpass a 90° Elbow

A 90° elbow is designed to change the heading direction of a pipeline in a perpendicular arrangement. It is worth mentioning that the inner (r_i) and the outer (r_o) rotating radius are not usually the same as indicated in Fig. 3.12(b). At the inlet of the curve, the front wheels encounter the curve contour before the other wheels, which causes the distance between the front and the passive wheels to shrink, the same situation as a contraction diameter previously explained. The opposite phenomenon occurs while exiting the curve. Therefore, the same motion strategy explained in Fig. 3.13 is assigned for the 90° elbow. In the case where the robot navigates in a vertical heading after exiting the elbow, the traction force is adjusted to a higher value by setting the holding angle (θ_h) to a higher level. That should provide enough force to counter the gravitational effects.

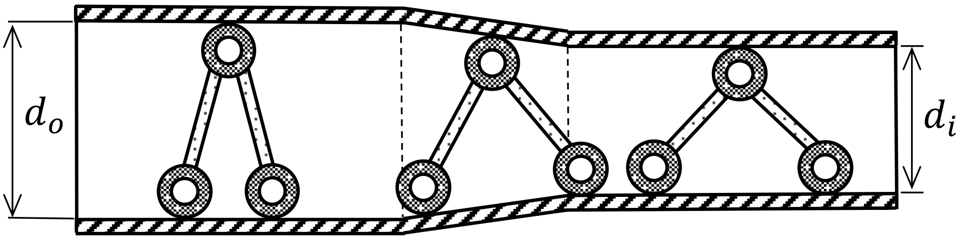

(a)

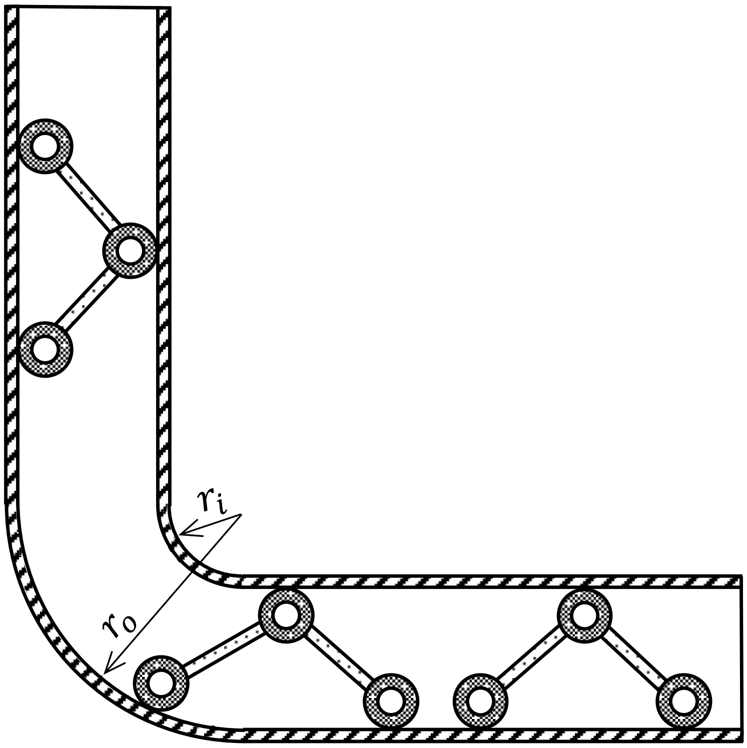

(b)

FIGURE 3.12: Complex pipeline setups; (a) A Funnel segment connects two different diameters pipelines, and (b) A 90° elbow to change the direction heading of the pipes by 90°.

3.7 In-Pipe Navigation Experiments

3.7.1 Experimental Setup

Fig. 3.14 shows the schematic diagram of the control system to drive the proposed in-pipe inspection robot. A multichannel direct digital synthesis (DDS) signal generator board (AD 9959, Analog Devices Corp., USA) followed by a power amplifier (BA4825, NF Corp., Yokohama, Japan) are used to generate the input sinusoidal voltages for the ultrasonic motors. The voltages passed through a custom-made switching board before being applied to the motors. The switching board consists of eight MOSFET transistors, and it is controlling the rotational speed of the motor through the pulse width modulation (PWM) technique. The board can also change the

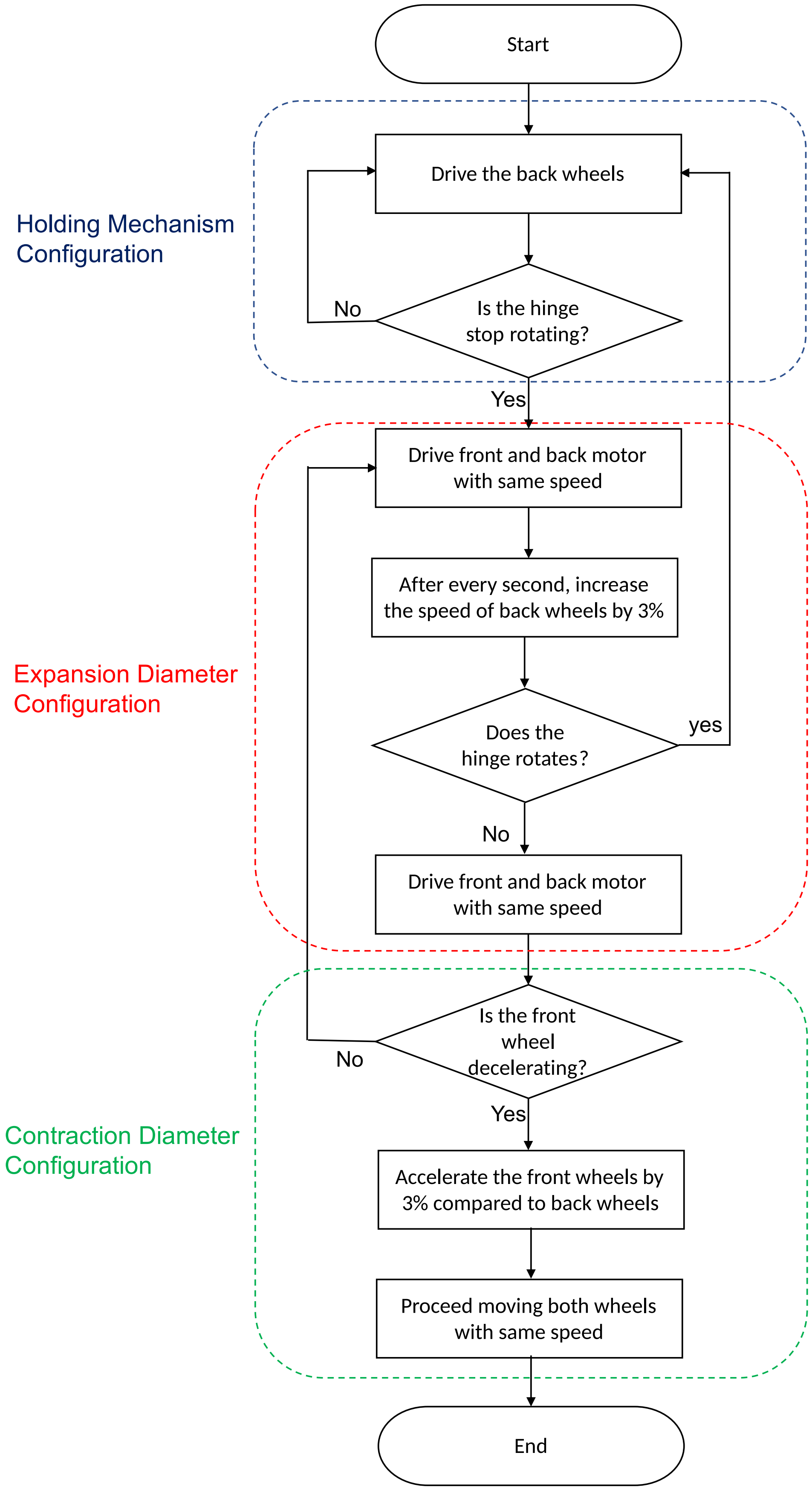
Start
Drive the back wheels
Holding Mechanism Configuration
No
Is the hinge stop rotating?
Yes
Drive front and back motor with same speed
After every second, increase the speed of back wheels by 3%
Expansion Diameter Configuration
Does the hinge rotates?
yes
No
Drive front and back motor with same speed
Is the front wheel decelerating?
No
Yes
Contraction Diameter Configuration
Accelerate the front wheels by 3% compared to back wheels
Proceed moving both wheels with same speed
End

FIGURE 3.13: Motion strategy to navigate through diameter expansion and contraction pipelines.

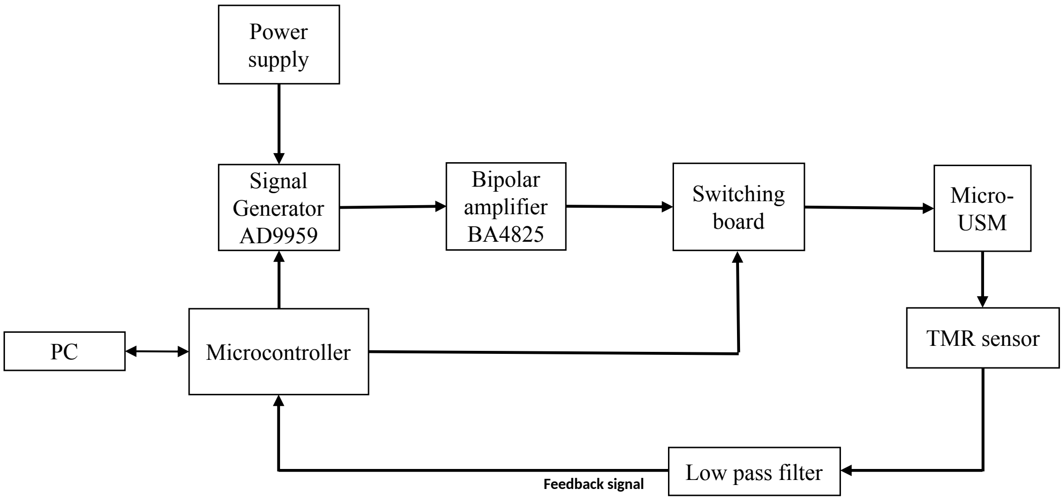

FIGURE 3.14: Control diagram circuit to drive the inspection robot through the pipelines.

rotational direction of motors (clockwise or anti-clockwise) by manipulating the phase angle of input voltages. The other setup components include an Arduino Uno microcontroller (Arduino Corp., Italy) at the core of the setup. The microcontroller is based on the ATmega 328P ship (ATMEL Corp., USA) that runs at 16 MHz. The microcontroller receives the feedback position signal from the position sensors, analyzes the situation, and performs the appropriate motion strategy by sending the updated PWM control signal to the switching boards. The feedback signal is filtered by a low-pass filter to remove any signal noises. All of the data are stored in the PC memory for storage and analysis.

3.7.2 Navigation in Complex Pipelines

Several experiments are conducted to analyze the characteristics and behavior of the proposed robot while navigating complex pipeline systems. The tests validate the versatility, adaptability, and robustness of the robot along with the motion strategies. Two test beds with the same configuration previously shown in Section IV are built using acrylic pipelines. The operator's interaction in the system is limited to adjusting the holding angle then the active control mode interferes and the controller drives the robot to the finish point.

The first experiment is to navigate inside two different diameters of pipelines connected by a funnel segment. The diameters of the two pipelines are 22 and 15 mm. This setup is placed on an inclined slope of 45° to make the test more challenging for the robot. The holding angle is initially set to 2° but the robot failed midway as it was about to enter the funnel segment, so the angle is re-adjusted to 4°. Fig. 3.15 shows snapshots of the robot's motion, expansion and contraction techniques are successfully functional as the robot navigates stably the intended setup at an average speed of 4.3 mm/s.

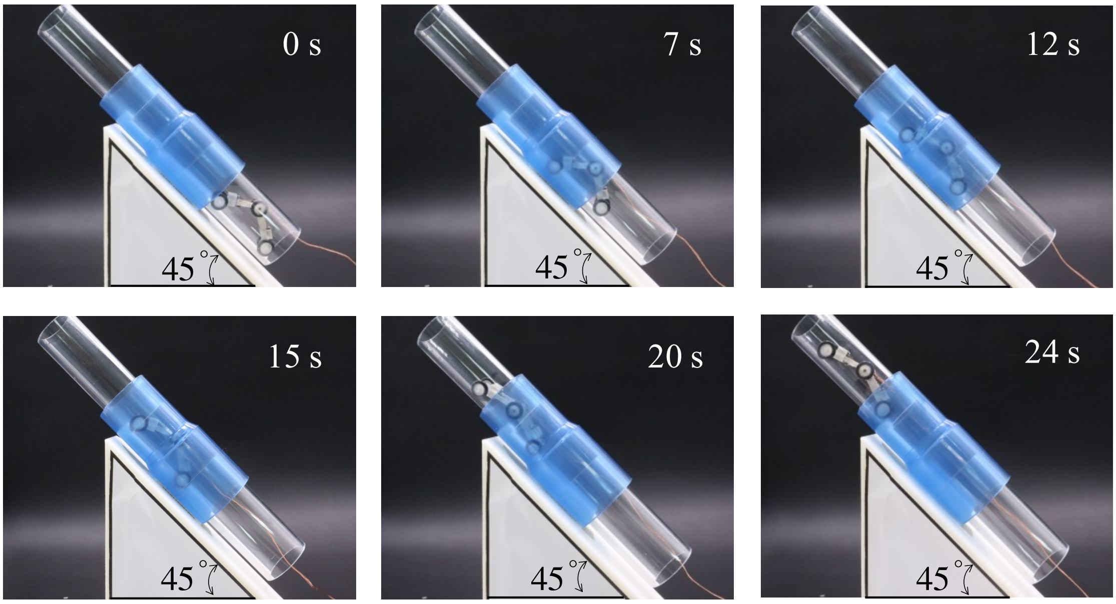

FIGURE 3.15: Demonstration of the navigation through a funnel segment connecting two different diameter pipelines, the setup is placed on a 45° slope.

To ensure that the robot can travel vertically, the second experiment of the 90° elbow is configured so that the exit pipe is pointed upward as shown in Fig. 3.16. In this experiment, we adjust θ_h to be 6° to encounter the influence of gravity. The robot's motion is shown in Fig. 3.16, it navigates with an average locomotion speed of 3.5 mm/s for horizontal locomotion and 2.1 mm/s for vertical climbing locomotion. The main reason why vertical locomotion is slower is attributed to the weight of the wires that act in the opposite direction of the locomotion. In contrast, when the robot is tested while descending in the same setup, speed is recorded as 4 mm/s as the weight of the wires acts in the same direction as locomotion. Through vertical locomotion, there are some accidents when the rubber tires come off from the wheels' hub, and the robot fails to make contact with the wall of the piping. In addition, an overload error occasionally occurs in the actuators, leading to the geared motors stopping rotating after operating for a long time. Therefore, decreasing the holding angle to 5° and curtailing the maximum operating speed can be considered as a reasonable approach.

3.8 Conclusion

The chapter presents the design and experimental of an inspection robot with an integrated holding force mechanism for narrow in-pipe inspection tasks. The robot is wheeled-driven and can employ two driving modes to navigate through pipelines diameters from 12 to 25 mm. The robot can switch between two driving modes to compromise between propelling speed and high traction force based on the condition inside the pipelines. The holding force mechanism was

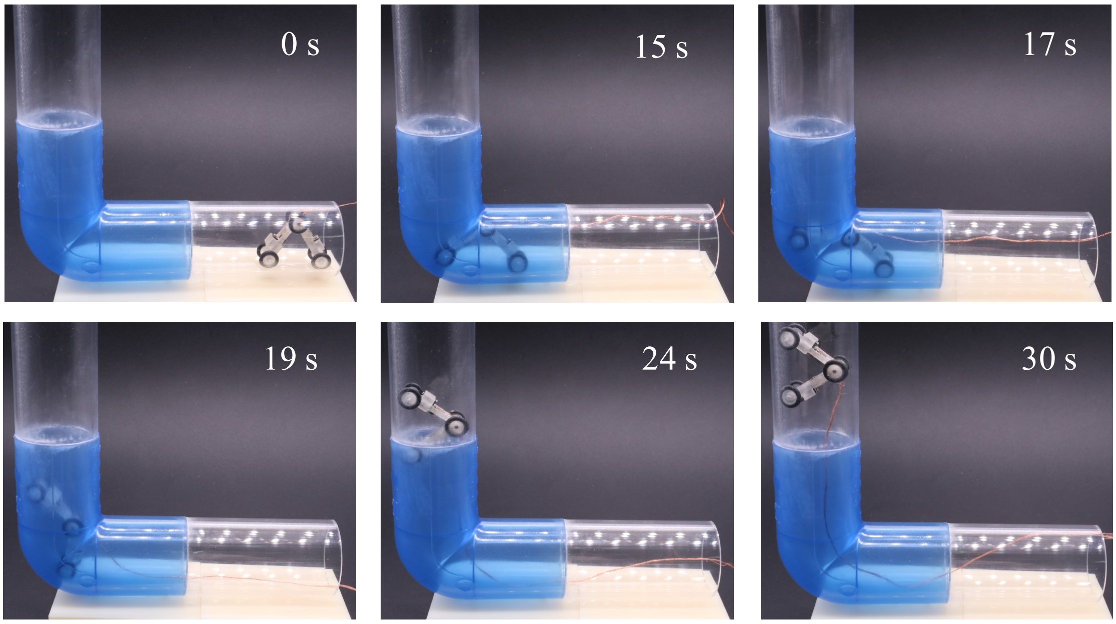

FIGURE 3.16: Demonstration that the robot can climb vertically after passing through a 90° elbow.

also evaluated, the tire's stiffness is advantageous to increase the contact area and the traction force of the robot without any extra equipment.

To navigate through complex pipeline systems like a funnel segment and a 90° elbow connection, a motion strategy that allows navigation in expanded and contracted pipe's diameter while retaining the traction force was demonstrated. The strategy was validated by experimentally testing the robot in real setups. The robot completed successfully all the intended tasks with efficiency and reliability.

Chapter 4

Climbing Capabilities Using Dry Adhesives

From the inclination of pipe inspection robot growth in recent years, the development of in-pipe inspection robots is much faster than the out-pipe ones. Although in-pipe robots suffer from operational difficulties related to the hard deployment during plant operation and navigating constraints during variations of pipe configuration like elbow, and step change, they are still applicable and effective during the installation of new pipelines or in plant shutdown. To enlarge the working domain of the insect-scale robot to a new era, we study the possibility of merging the robot with an adhesive mechanism to perform other inspection tasks. In general, wall climbing robots can navigate along vertical walls with certain loads to perform various tasks, such as urban reconnaissance, an inspection of nuclear power plants, and window cleaning [110–112]. Climbing robots combine mobile technologies with different adhesion mechanisms. A wall climbing robot can overcome large obstacles by walking up and over them, or it can access high vantage places by ascending vertically [113]. A compact, climbing robot can outmaneuver a large robot in tight spaces and surmount obstacles that the large robots cannot climb. When size and efficiency are critical, a lightweight structure with minimum complexity is more adequate.

4.1 Basic Design Requirements of Climbing Robots

Climbing robots are mainly used to carry out risky tasks in hazardous environments, so they require certain basic characteristics, such as functionality, a lightweight structure, fast climbing speed, high safety, strong environmental adaptability, and the ability to climb objects without damaging their surfaces. These requirements can be detailed as follows:

- Functionality: This is the primary consideration in climbing robot design, it refers to the capabilities of climbing robots to perform the intended design purpose with robustness and efficiency.
- Lightweight structure: Climbing is an energy-intensive process, a lot of energy is required to propel a robot against gravity. Therefore, climbing robot prototypes should be as light as possible to minimize their size and energy consumption.
- Fast climbing speed: Robots are mainly used to replace skilled workers to conduct tasks that are difficult, hazardous, or boring, so their work efficiency must be higher than that of humans. In general, the continuous-moving pole climbing robot, i.e. using rotating wheels, is faster and lighter than the step-moving pole climbing robot.
- Good environmental adaptability: As climbing is performed on different shapes and materials, climbing robots need good environmental adaptability to be able to climb objects of various diameters, lengths, materials, shapes, tilt angles, and surface roughness.
- Obstacle negotiation ability: The surfaces of climbed objects are not always flat and smooth. Some have bulges, pits, steps, or forks, which requires robots to have good obstacle negotiation abilities. That includes the ability to perform Surface-to-surface transitions between oriented surfaces.
- Working safely and reliably: During the climbing process, a robot can experience a power failure, jammed mechanism, or other faults. This requires robots to have a self-protection ability so that they will not fall from height in the case of a power failure or can be safely recovered in case of jamming. In other words, the robot must retain adhesive forces in case of power failure.
- A high payload capacity: Climbing robots should have a high payload capacity as carrying multiple tools and sensors would eventually expand their functional range.
- Other factors to be considered include adhesive techniques, cost, energy supply mode, and size. Some working spaces are limited, necessitating a small robot. Robots incorporated with claws or spins as an adhesive mechanism may be unsuitable for soft climbed objects. In addition, manufacturing costs must be considered; accordingly, components and modules that can be bought online should be preferred.

4.2 Miniaturization of Climbing Robots

Although various climbing prototypes have been seen since the 1980s, the design and prototyping of insect-scale climbing robots have not started until recently. One of the main reasons is the fabrication limitation for the actuation systems and the lack of proper adhesive technology. It means that the full locomotion capability of such robots is still under development. For example, Harvard Ambulatory Microrobot (HAMR) can climb on incline surfaces using gecko-like dry adhesive legs [114]. Surprisingly, another prototype of the HAMR succeeded to climb inverted and vertical walls using electro-adhesion technology [115]. Using simple adhesive pads is also effective for climbing robots less than 100 mm [116], [117]. These insect-scale climbing robots demonstrate excellent locomotion on a flat surface but show less ability to overcome obstacles and steps.

The proper selection of adhesion method, locomotion mechanism, and actuation mechanism should enable climbing robots to have a structure as thin and light as possible. In this section, we will study the possibility of combining the insect-scale climbing robot with a low-cost dry adhesive technology to address climbing challenges, such as surface-to-surface transitions, vertical and inverted locomotion, and high payload capability. The design principles adapted from the caterpillar allow the robot to achieve transitions such as movements at right-angle corners. Moreover, the high torque-to-weight ratio achieved by the two micro-geared ultrasonic motors also permits vertical and inverted locomotion along with high payload capacity. The resulting robot is the smallest insect-scale robot that can reliably climb walls vertically and invertedly while carrying extra payloads and performing various surface-to-surface transitions by using only adhesive wheels.

4.3 Basic Climbing Skills of the Prototype

4.3.1 Vertical and Inverted Climbing

By integrating an adhesive mechanism into the caterpillar-inspired insect-scale robot, its motion range and working domain can be extended. The strong grip allows caterpillars to attach themselves to arbitrarily oriented objects. The alternation of fastening between the front and rear legs generates linear locomotion. This pattern allows caterpillars to climb vertical surfaces as stationary legs provide anchoring force to hold their weight [118]. The same pattern is followed by our prototypes, by integrating the front and rear wheels with an adhesive mechanism, the robot can cover all the intended motion range efficiently.

The biologically inspired climbing robot is designed to navigate three-dimensional structures and to manipulate objects. The basic manipulation skills we have developed are vertical and inverted locomotion and propelling itself on arbitrarily oriented surfaces in an online fashion, in the absence of geometric models and independent of the direction of gravity. The robot can achieve forward and backward movements freely on different wall surfaces, as it is designed to move on horizontal, curved, vertical, and inverted surfaces.

4.3.2 Surface-to-Surface Transition

Overcoming obstacles is not only a necessary function but also a tough problem for climbing robots. Transitioning from one surface to an intersecting one is considered as a typical example to be overcome. To discuss whether the robot can achieve the transitions between surfaces that form right angles, we define the angles with 90 and 270 degrees as concave (inner) and convex (outer) corners, respectively, as shown in Fig. 4.1(a). This issue has been addressed by several regular-sized robots that consist of several modules connected in series by joints [119–121]. They achieved concave and convex transitions successfully, but such a combination of multiple modules enlarged their size. At a small scale where adhesion forces dominate, miniature robots overcome obstacles with relatively simpler methodologies than those of large robots. We show how the proposed caterpillar-inspired robot achieves concave and convex transitions.

4.3.2.1 Concave Transitions

Fig. 4.1(b) shows the motion strategy to make a concave transition. The robot starts by moving its front wheels to the new surface, bringing its rear wheels close to the corner, extending its front wheels further on the surface to make room for the back wheels, and moving the back wheels to the new surface. At the corner, the wheels adhere to both perpendicular surfaces at the same time, providing an instantly adhesive force to anchor the robot's weight on the vertical surface. This strategy allows the robot to move from horizontal to vertical surfaces or from a vertical surface to an inverted one.

4.3.2.2 Convex Transitions

The criteria are more complicated than concave transitions. Figs. 4.1(c) and (d) show a normal climbing robot without a pivot joint and a caterpillar-like robot at the convex transition, respectively. First, let us observe the motion of the normal wheeled robot shown in Fig. 4.1(c). It can climb on the wall with an appropriate adhesion force regardless of the pivot joint. However, after reaching the convex corner, the front wheels cannot progress on the horizontal surface without the pivot joint. From this situation, when the rear wheels generate torque, the front wheels disengage from the corner and make the robot's body flip over. Imitating the motion of caterpillars enables the transition at the convex corners where the normal robots cannot overcome [122]. As shown in Fig. 4.1(d), after the front wheels reach the corner, the rear wheels also are controlled to approach the corner by using the pivot joint. This posture allows the front wheels to transit

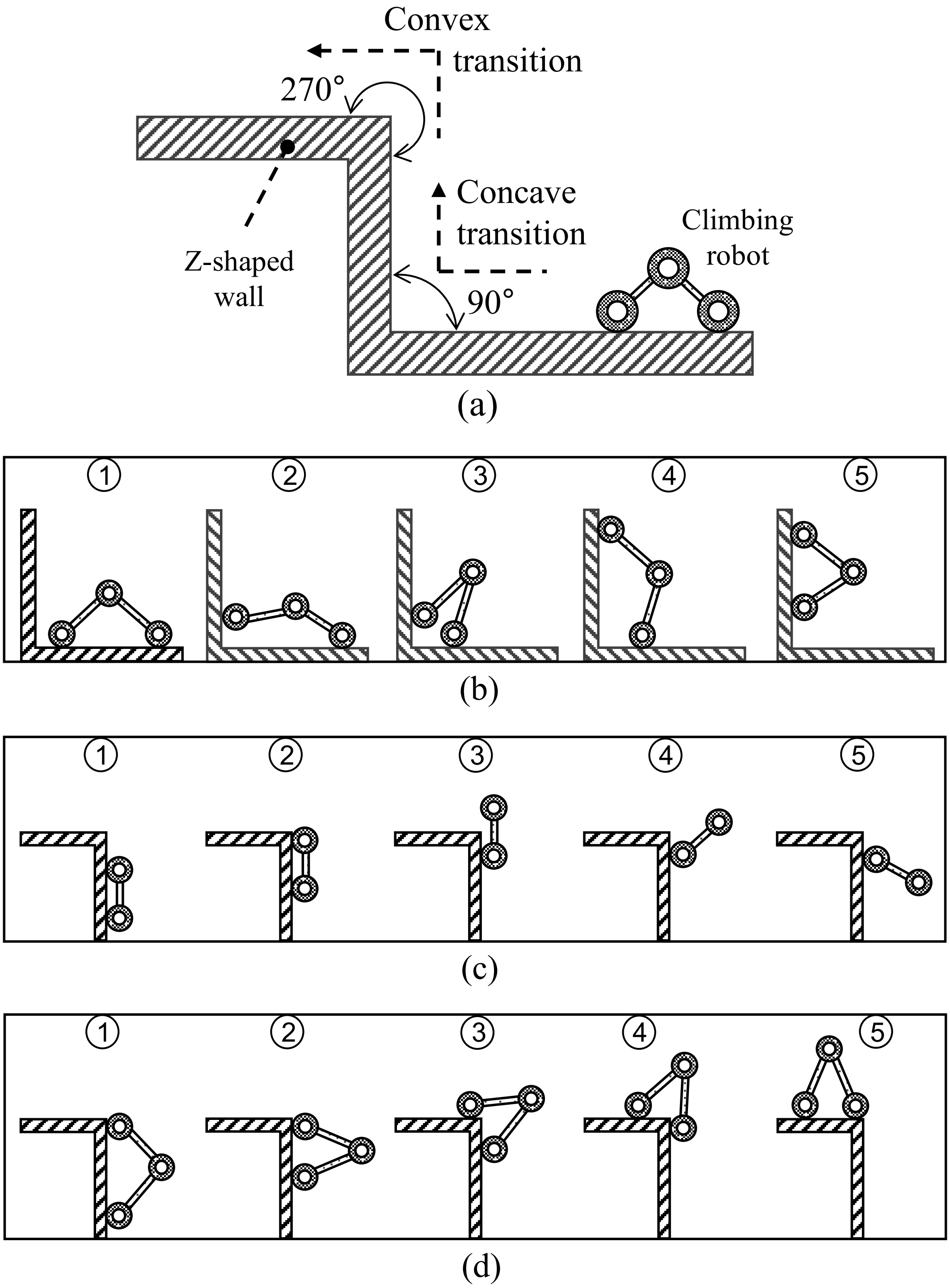
Convex
transition
270°
Concave
transition
Climbing
robot
Z-shaped
wall
90°
(a)
① ② ③ ④ ⑤
(b)
① ② ③ ④ ⑤
(c)
① ② ③ ④ ⑤
(d)

FIGURE 4.1: (a) Demonstration of concave and convex corners. (b) Motion strategy to make a concave transition. (c) and (d) a Comparison between two design approaches for a convex transition; (c) A normal wheeled robot and (d) a caterpillar-like robot.

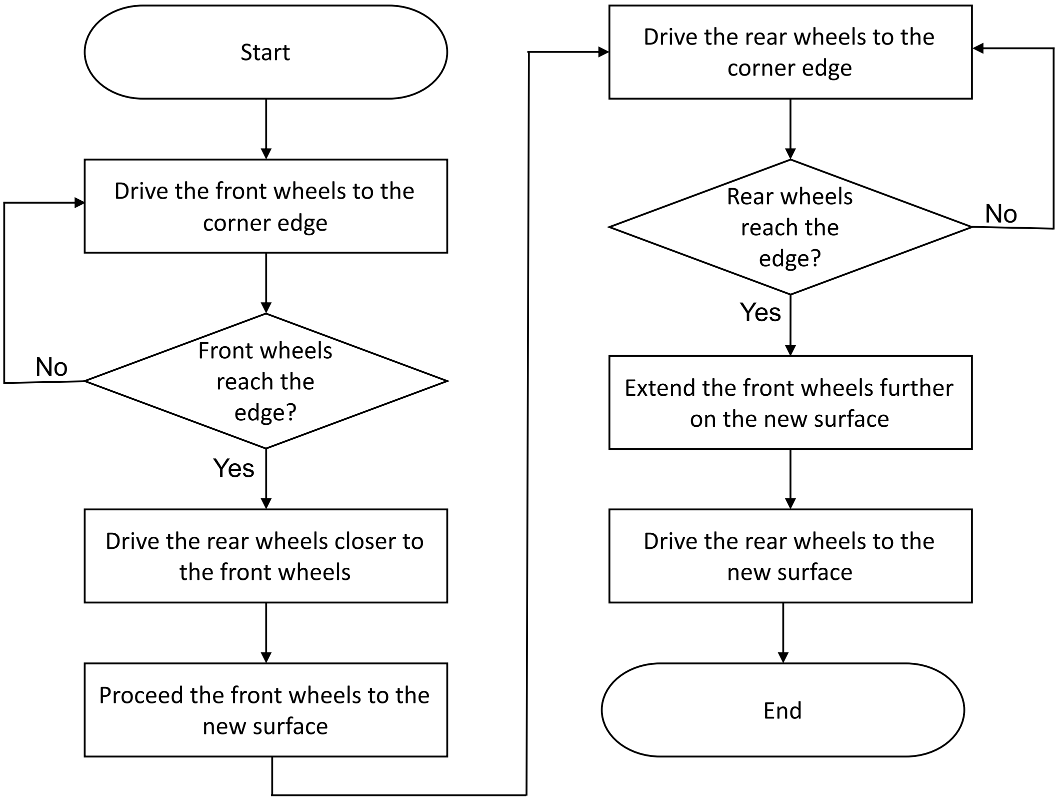
Start
Drive the front wheels to the corner edge
Front wheels reach the edge?
No
Yes
Drive the rear wheels closer to the front wheels
Proceed the front wheels to the new surface
Drive the rear wheels to the corner edge
Rear wheels reach the edge?
No
Yes
Extend the front wheels further on the new surface
Drive the rear wheels to the new surface
End

FIGURE 4.2: Motion strategy for the caterpillar-like robot to make the convex transition.

the corner and move to the next surface horizontally. As with the front wheels, the rear wheels also can overcome the convex corner without detachment. The motion strategy for the convex transition is explained in Fig. 4.2.

4.4 Adhesive Technology

Adhesives for climbing robots face a challenging requirement in terms of the unpredictable or wide-ranging terrains that the robots are expected to walk/climb on. There are several types of adhesion techniques realized. It is worth saying that the adhesion method has become a bottleneck in the development and application of wall climbing robots, so there has been a sustained interest in pursuing novel adhesion methods, which can benefit from the simplicity, lightweight, and work stability of the latest climbing robots. Commonly used adhesion methods previously reported include magnetic adsorption, air pressure adsorption, clamping adhesion, claw grasping, electrostatic adsorption, and biological adhesion adopted by nature. The last one has been inspiring researchers on the development of bio-mimetic robots over the past few years. In the following subsections, we will report the most common adhesive techniques, then a comparative discussion will be conducted to point out the best approach for our prototype.

4.4.1 Magnetic Adsorption

The magnetic adsorption method adopts a permanent magnet or electromagnet (or a combination) to retain contact on the wall, its applicable range is only limited to ferromagnetic objects. A permanent magnet is one of the most common magnetic adsorption methods. It can be divided into contact and non-contact types according to whether the magnet is in contact with the surface of the climbed object. Contact permanent magnet adsorption involves a combination of a permanent magnet and a moving mechanism. For instance, a rotating magnetic wheel with fourteen magnets that are arranged in a circumferential layout is shown in Fig. 4.3. As the wheel rotates, two or three magnets always act on the pole to keep the adhesive forces almost constant. Omnidirectional magnetic wheels were also presented in [123, 124], ring magnets and magnetic rollers were used as magnetization elements which allow the prototypes to perform bi-directional climbing. Although contact permanent magnet systems have a compact structure, some contact wear problems were reported in the long term. On the other hand, a non-contact magnetic system has a separate layout for magnetization apart from the locomotion mechanism, which leaves a gap in the surface. The magnetic modules are fixed to the chassis of the robot with an adjustable mechanism to dynamically adjust the adsorption force while climbing [125]. This scheme not only achieves higher magnetic energy utilization than magnetic tracks or magnetic wheels but also has the flexibility of magnetic wheel technology. In the case of climbing irregular or large-radius surfaces, position sensors are integrated into the magnetization system to maintain the heading between the magnet and the climbed surface via servo motors to keep the adsorption force stable as shown in Fig. 4.4. In permanent magnet adsorption, the magnetic force is fixed. While energy is not required to maintain the magnetic force, it cannot be turned off. To solve this problem, switchable permanent magnets have been used in some prototypes as depicted in [126]. However, this device can only switch the magnetic force on or off and cannot adjust its strength.

Electromagnetic adsorption uses the electromagnetic principle to energize an internal coil to generate a magnetic force. Electromagnetic adsorption has also been used in climbing robots because it can be used to switch the magnetic force on and off as well as adjust its strength [129]. According to the electromagnetic adsorption principle and control requirements, a distributed control mode is used to accurately adjust the magnetic force of each part of the adsorption module. In addition to permanent magnetic adsorption and electromagnetic adsorption, hybrid magnetic adsorption devices based on their advantages have been designed. A magnetic wheel that uses electro-permanent-magnet technology was presented in [130], the wheel is composed of two permanent magnets with different magnetism, two magnetic poles, and copper-enameled coils. Such a mechanism allows the magnetic force to be controlled by simply applying a short electrical pulse to the coil winding. By controlling the amplitude of the electric pulse, the

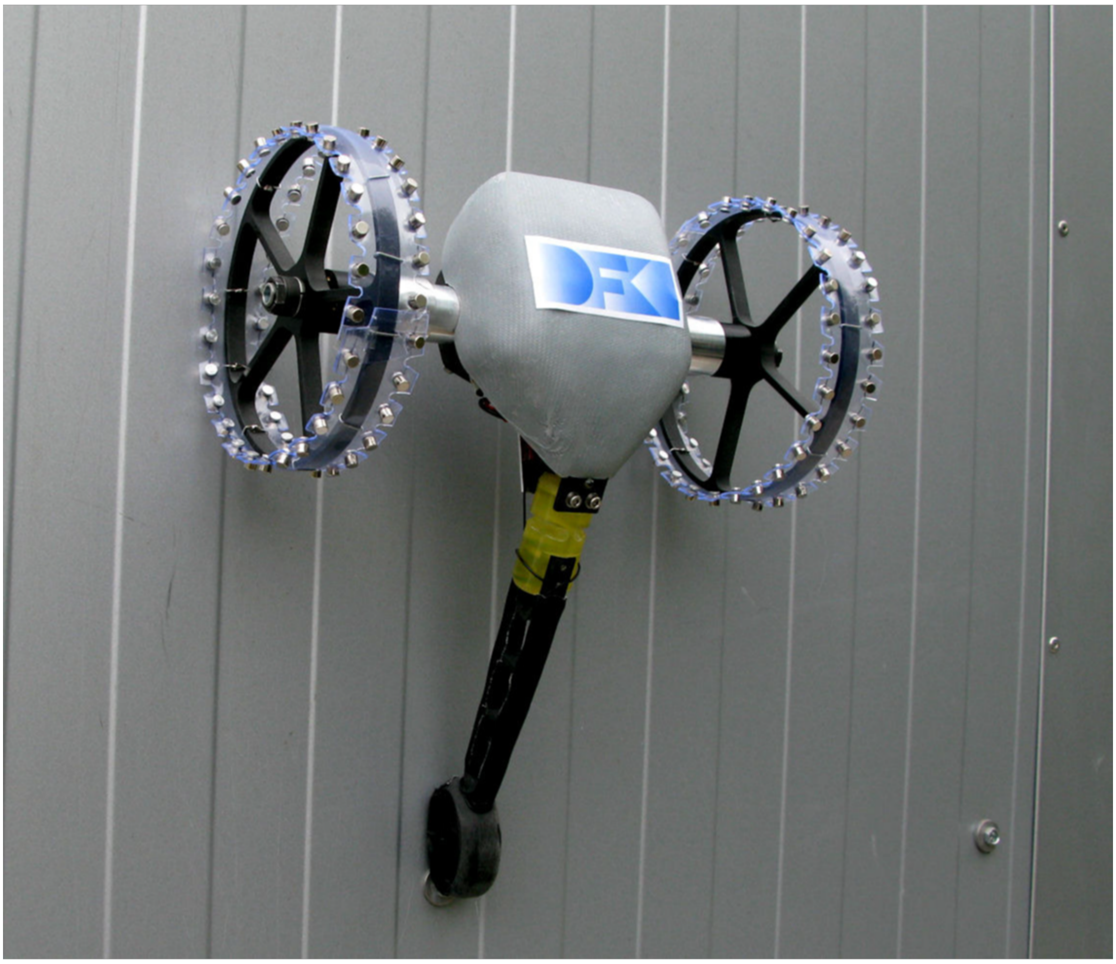

FIGURE 4.3: The MINOAS magnetic crawler uses permenant magnets on the wheels and on the tails to climb vertical walls. [127]

magnetic force can be adjusted to the required value to realize continuous changes in magnetic adhesion.

To sum up, the main advantage of magnetic adsorption methods is that their adsorption force is strong. Permanent magnets do not need additional energy or only a small amount. Electromagnets can control magnetism by switching on and off. The disadvantage of magnetic adsorption is that it is not applicable to non-ferromagnetic materials such as cement, brick, or stainless steel. Furthermore, some applications need to be electromagnetic-proof and explosion-proof. The magnetic adsorption force is related to the area of the magnet and the distance between the magnet and the metal surface. Its strength decays rapidly with distance from the object's surface. Magnets are generally heavy, which increases the weight of the robot and reduces its load-carrying capacity. For permanent magnets, the magnetic force is fixed and difficult to eliminate. Electromagnets need an uninterrupted power supply. When power is lost, the magnetic force will disappear, posing certain safety risks.

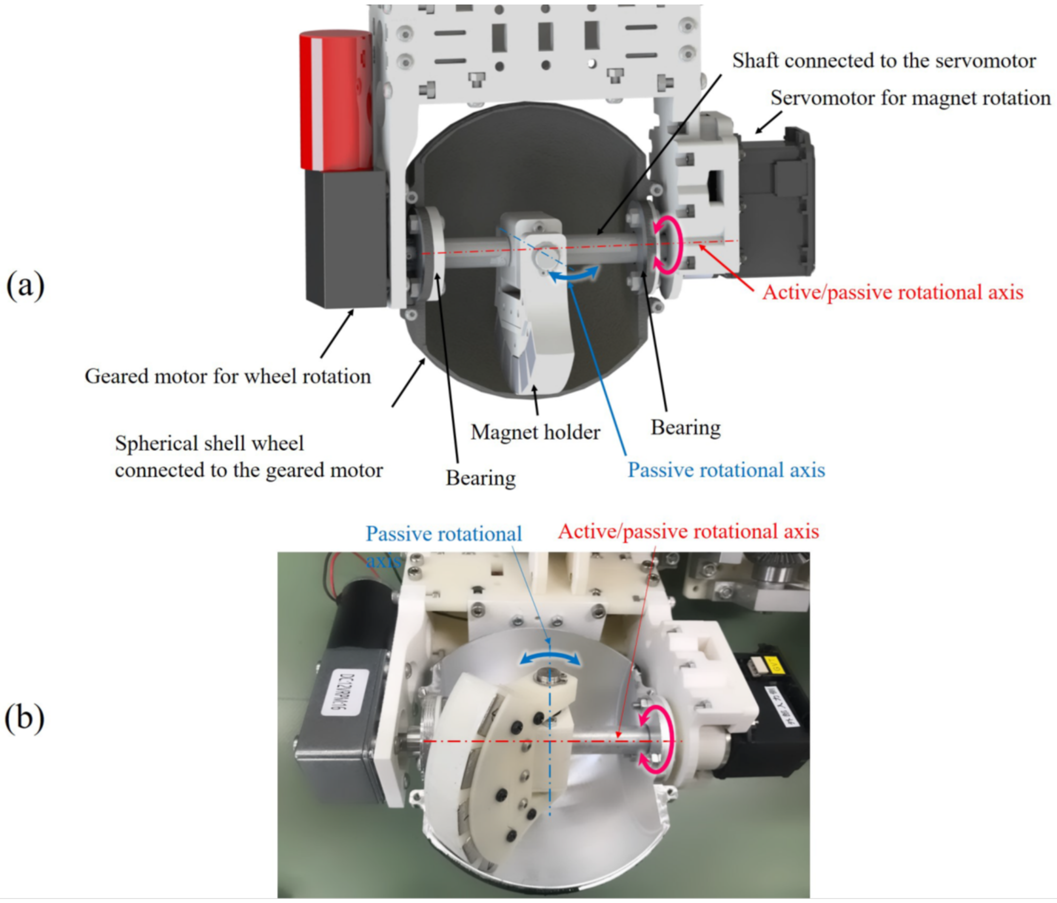
(a)
Shaft connected to the servomotor
Servomotor for magnet rotation
Active/passive rotational axis
Geared motor for wheel rotation
Spherical shell wheel
connected to the geared motor
Magnet holder
Bearing
Bearing
Passive rotational axis
(b)
Passive rotational axis
Active/passive rotational axis

FIGURE 4.4: Two servo motors are controlling the heading direction of a magnet to maintain magnetization force with irregular surfaces; (a) Design of the magnetic spherical wheel. (b) Actual prototype of the wheel. [128]

4.4.2 Air Pressure Adsorption

On large and flat surfaces, climbing robots often use air pressure adsorption, which can be classified as active or passive systems. while active adsorption uses a vacuum, negative pressure, or positive pressure, passive adsorption uses suction cups without additional power-operated vacuum pumps or negative-pressure chambers.

As a general design, passive adsorption uses multiple suction cups to alternately engage and disengage, so that the robot can attach to a flat surface as shown in Fig. 4.5. Passive adsorption systems are lightweight and quiet because they do not require a vacuum pump or a propeller [131]. The attachment mechanism involves multiple passive suction cups that are fixed on the outer surface of the crawler at equal intervals and rotate with the crawler. Under the action of a guide rail, the cups can be attached to the wall and then pressed and separated. Despite its advantages, its applicable work domain is limited to exquisite surfaces as the adhesive force is not guaranteed.

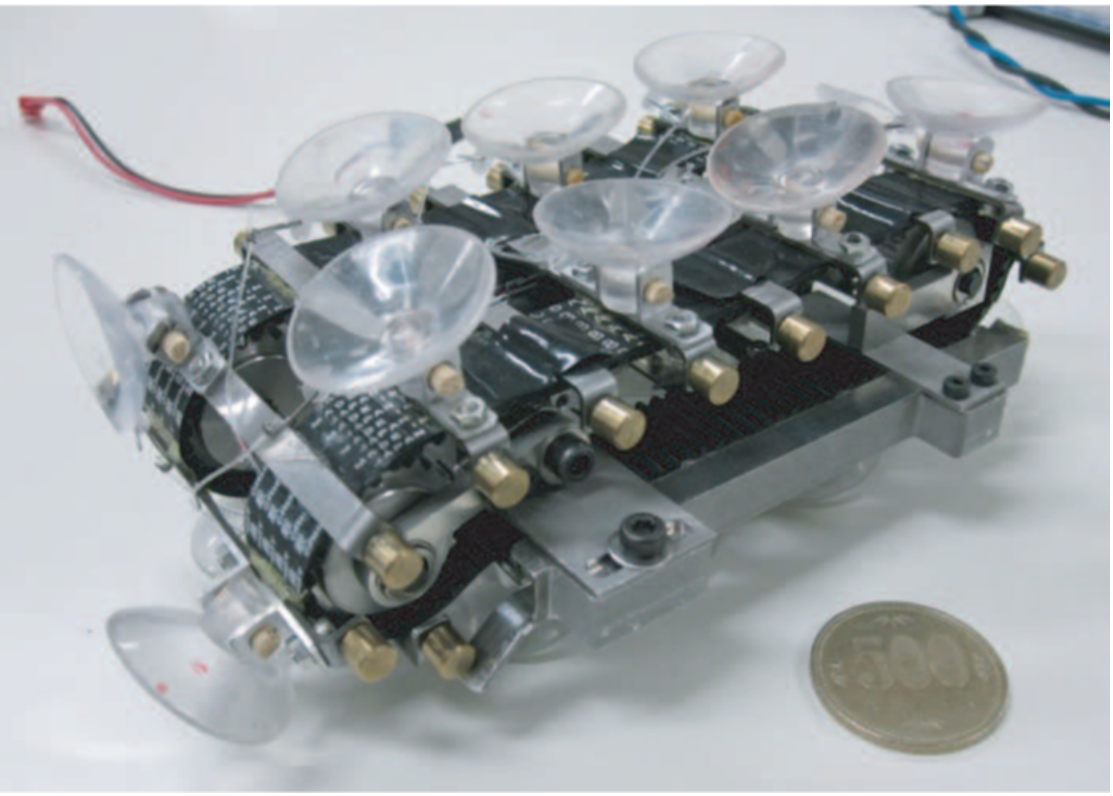

FIGURE 4.5: A climbing robot employs multiple passive suction cups to climb vertical walls. [133]

The design is improved by using active suction cups, where a vacuum suction mechanism exhausts the air from a suction cup using a vacuum pump to adhere to the climbed surface [132]. Vacuum adsorption is easy to control and has a high load capacity. It is not limited by the surface material but by its quality and generally works efficiently on smooth surfaces. The strength of its adsorption force is related to the pressure difference and adsorption area. If there are holes or gaps in the surface, the suction force will be likely reduced due to leaks. In addition, vacuum adsorption requires a vacuum pump and a good sealing chamber, which increases the energy consumption, complexity, weight, and noise level of the robot.

Negative-pressure adsorption uses the adsorption force generated by an impeller or eddy current to fix the robot to a surface [134]. An eddy current can cause local negative pressure via a rapidly spirally rotating airflow in a closed cavity, which is somewhat similar to the tornado effect. The adsorption mechanism consists of a vacuum chamber, an impeller with a motor, and a double-layer sealing device. When the motor drives the impeller, the air in the vacuum chamber is expelled, creating a pressure difference between the environment and the vacuum chamber, so that the robot adheres to the surface [135]. Eddy's current adsorption does not require suction cups, so it can adapt to rough surfaces and obstacles. Although negative-pressure techniques improve the capability of air pressure adsorption compared to suction cups, they require a considerable amount of electrical energy to perch on the wall.

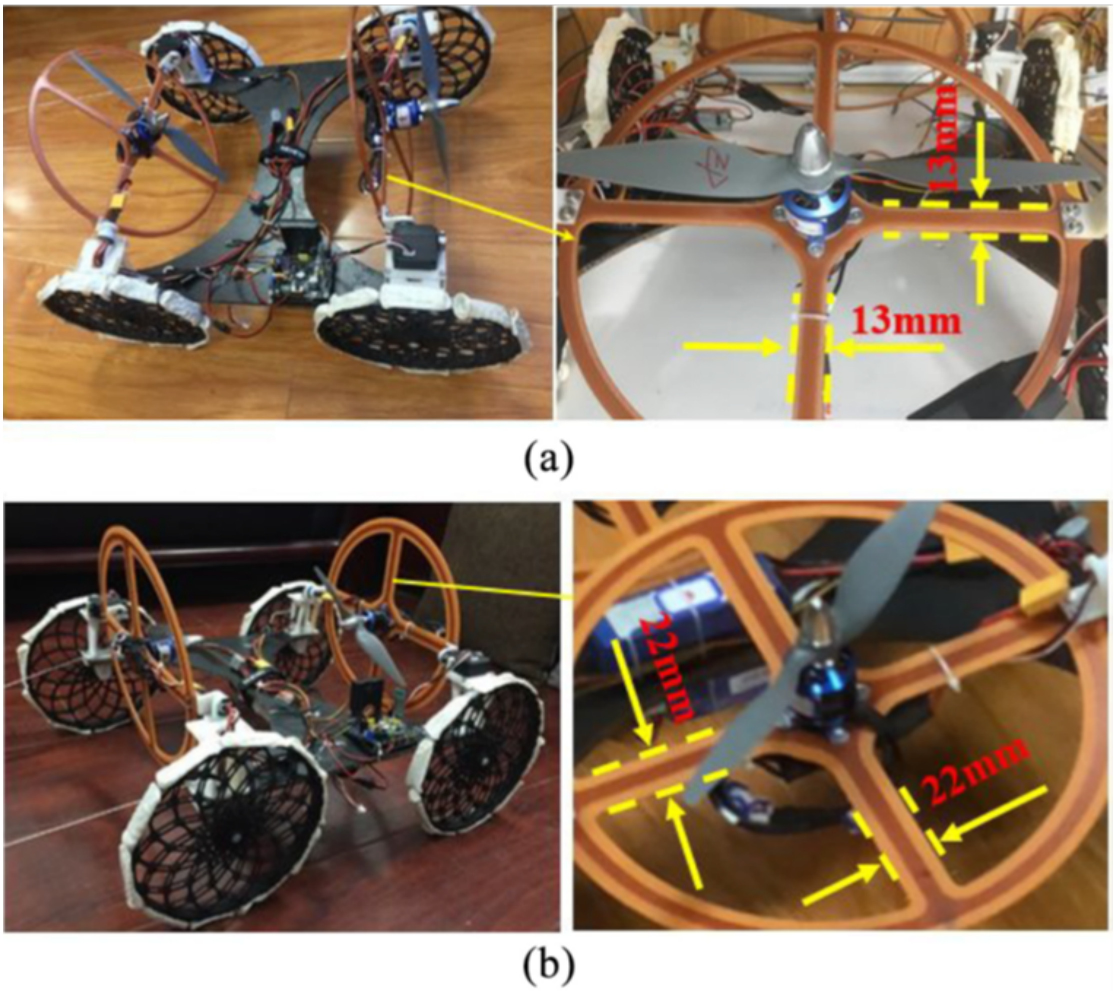

FIGURE 4.6: A climbing robot employs a movable double propellers design to propel the robot on horizontal and vertical surfaces; (a) and (b) different sizes of propellers were investigated in the research. [137]

On the contrary, positive-pressure adsorption employs the wind force generated by a propeller to push a robot to a surface, allowing it to adapt to surfaces of various shapes. The propellers create a pressure difference which results in creating a downward thrust that keeps the robot attached to a surface. The propellers are usually fitted by an angle adjustment mechanism to adapt the robot to various climbing conditions and the orientation of the robot as presented in Fig. 4.6. The system has good environmental adaptability as it can be applied on non-smooth surfaces, while its main drawback is related to the excessive power needed to keep adequate adhesion. To improve the adsorption effect, air pressure adsorption systems can be combined. For example, vacuum and positive adsorption are used simultaneously in the Rise-Rover wall-climbing robot design so that the robot can adhere to smooth surfaces and also span grooves [136].

4.4.3 Mechanical Grasping Attachments

At present, the bionic adsorption wall-climbing robot can walk on clean and smooth glass or wall surfaces, but when moving on rough and complex wall surfaces, this requires the dry glue adhesive to be resistant to foreign objects such as dust and oil. In this case, It can mimic other biological mechanisms such as flexible claws and spines.

Inspired by insects and arthropods, mechanical grasping systems employ various attachment mechanisms such as claws, spines, or grippers to anchor a robot to a structure. On the one hand, the claw grasping method is a bionic attachment method that uses a claw horn structure to anchor to the surfaces of relatively rough objects, such as brick walls, tree trunks, and rock walls [138]. The claw grasping can be applied as cockroach-like barbed feet to climb hard and flat surfaces as employed by Spinybot robot [139]. Advanced mobility like stair climbing and curb mounting were presented by Recon Scout XT, a commercially available platform sold by ReconRobotics. It is made with a titanium body and polyurethane wheels fitted with flexible spines as shown in Fig. 4.7.

On the other hand, clamping systems use grippers or other encircling mechanisms to attach a robot to a structure. According to the way, the clamping force is generated, clamping methods can be divided into several forms, such as pneumatic clamping, electric clamping, spring clamping, mechanical clamping, and serpentine winding [140]. Fig. 4.8 shows a prototype that uses mechanical grippers to climb tree branches by accumulating elastic energy in its soft body. Under the action of the linear motor and spring, a robot fitted with grippers can climb various tree species and can clamp the surface of an object using a spring without requiring electricity, providing a good energy-saving effect. Generally, grippers can be easily adapted to slender rod-shaped objects, such as beams, columns, pipes, and trees. However, it is not suitable for flat objects [141].

To sum up, mechanical grasping attachments have been successful on rough surfaces, but they either leave damaging marks on the surfaces or can penetrate the object being climbed in case of penetrable surfaces.

4.4.4 Electrostatic Adsorption

When an object with static electricity approaches another surface, charges of opposite polarity will accumulate on the surface based on the principle of electrostatic induction, which will lead to electric attraction. Therefore, attachment and detachment of the robot on the surface are realized by adding and cutting off the voltage to the electro-adsorption mechanism. The first generation of prototypes using this technique could only achieve movement on clean glass surfaces with limited maneuverability [144].

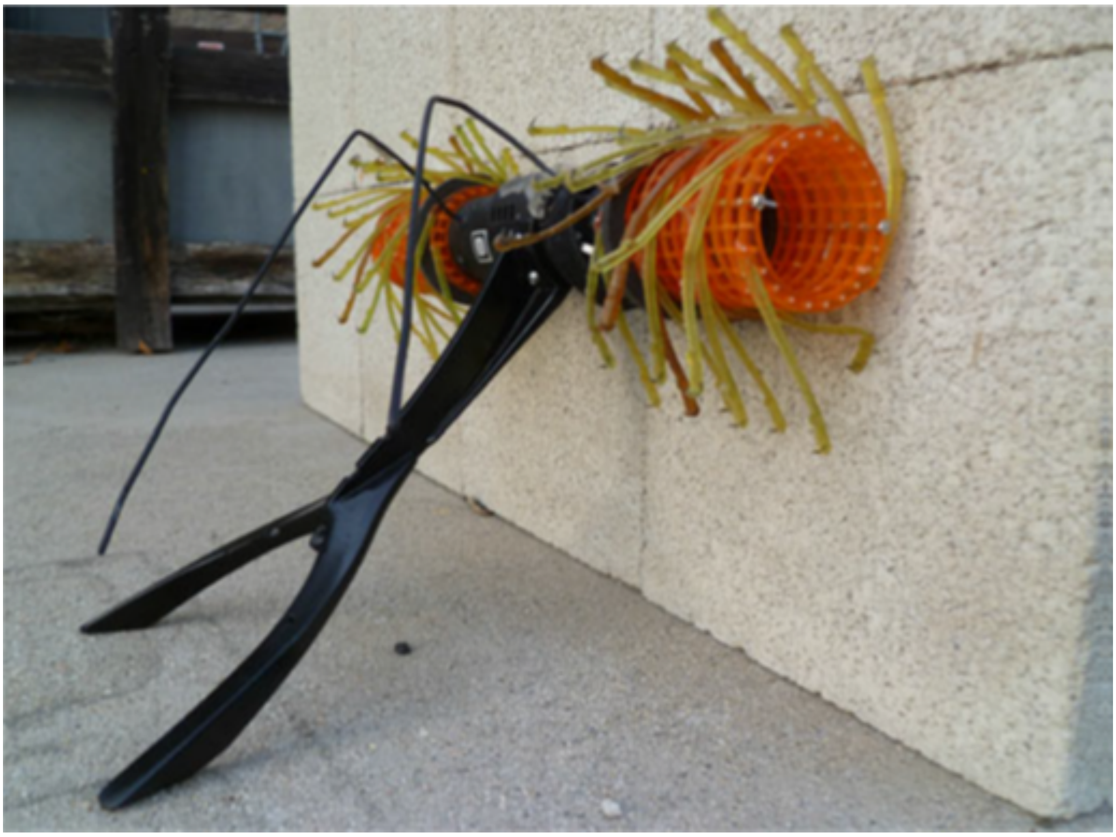

FIGURE 4.7: Recon Scout XT robot uses rotary microspine wheels to achieve advanced mobility like stair climbing and curb mounting on rough surfaces. [142]

Continuous research on electrostatic adsorption materials and technologies over the years has improved the electrostatic adsorption capacity, and therefore, its application in wall-climbing robots is also increasing. The advantage of that improved methodology is that it uses very little power and exhibits the ability to repeatedly adsorb on walls heavily covered with dust or other debris [145]. Fig. 4.9 shows an insect-scale climbing robot ”HAMR-E” fitted with electro-adhesion pads navigates invertedly on curved surfaces. Combined with a novel multi-stage manufacturing process of layered hybrid adhesives, the robot could climb vertical and inverted surfaces with a maximum speed of 3.1, 0.026, and 0.1 body-length/s on horizontal, vertical, and inverted surfaces respectively.

To sum up, electrostatic adsorption can make the wall-climbing robot lightweight, integrated, and miniaturized. Moreover, electrostatic adsorption has lower requirements on the wall surface. It can be applied on the smooth wall surface of glass material or the rock wall surface with high surface roughness as long as a high load capacity is not required. However, the concern of using electrostatic force lies in its continuous high operating voltage to keep adhesion force.

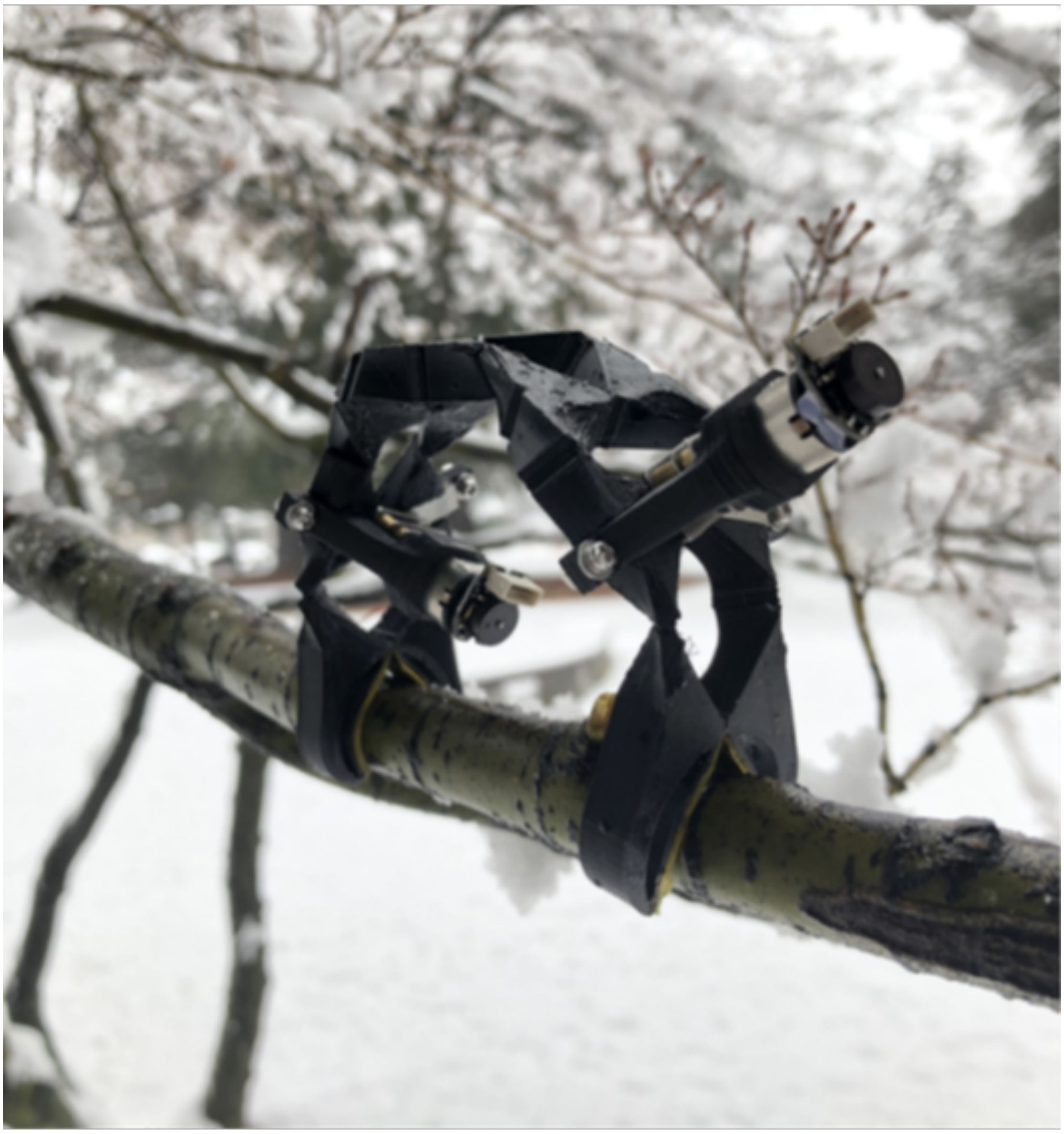

FIGURE 4.8: The Brachiation robot using elastic energy stored in its soft body and mechanical grippers to climb tree branches [143]

4.4.5 Bio-Inspired Adhesion

Bionics and biorobots are flourishing fields of modern scientific research. This approach mimics the characteristics of living species in nature that can navigate over vertical wall surfaces. This method uses bio-inspiration as its core principle for synthesizing new artificial mechanisms for wall climbing. Since species in nature have evolved over millions of years, artificial systems mimicking their locomotion over wall surfaces have the potential to offer a high degree of efficiency. With the development of this technology, wall-climbing robots have a wide range of practical application potential. Generally, the biomimetic adsorption structures are mainly based on imitating the principle of adhesion of biological feet in nature. They are mainly divided into

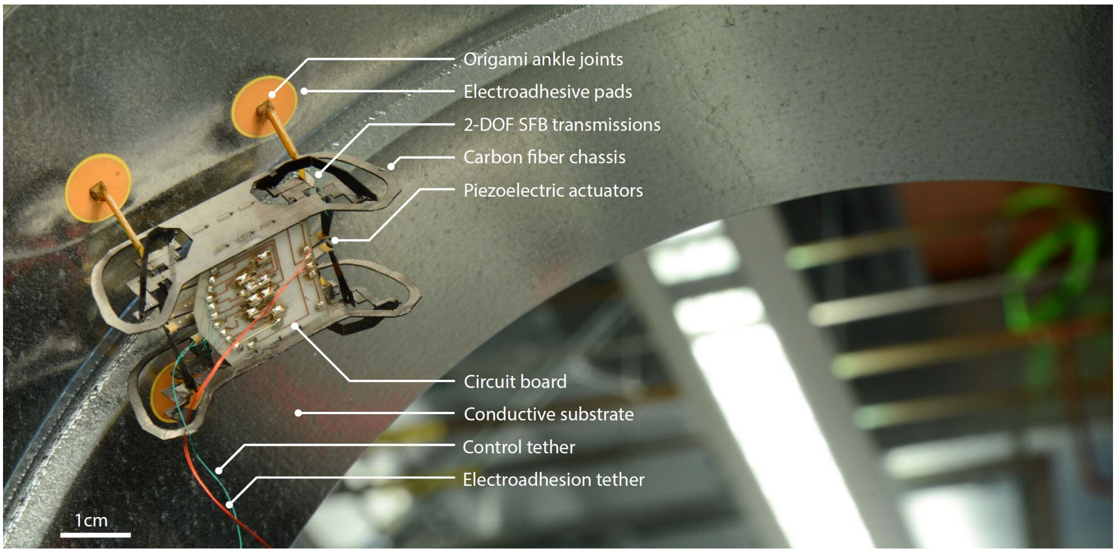

FIGURE 4.9: HAMR-E, an insect scale climbing robot, climbs inverted curved surfaces using electro-adhesion pads. [115]

dry adhesion and wet adhesion systems. Dry adhesion relies on the van der Waals force between molecules to attach the robot to a surface. Wet adhesion relies on surface tension and the capillary and viscous forces between liquids to adhere a robot to the surface of a wet object.

The history of bio-inspired adhesion started in 1965 when the biologist Rodolfo Ruibal examined a gecko's feet under an electron microscope and discovered that the ends of the bristles that looked like small hooks were split. Each bristle is divided into 100–1000 finer hairs. These hairs significantly increase the area of the gecko's soles, especially when the gecko climbs on the surface of those rough objects; these fluffs can fill the small hollow [146]. In this way, the villi on the bristles of the gecko's toes have a large contact area with the object's surface, and there is an attractive force between molecules and molecules. This force is called the van der Waals force, although the van der Waals forces between a single pair of molecules are tiny. However, if the number of interacting molecules is enormous, the accumulation of these tiny forces will be considerable [147]. Inspired by the gecko's adhesive technique, Fig. 4.10 shows a centimeter-scale prototype called Stickybot that was able to climb vertically on glass surfaces. Likewise, another prototype could climb painted interior walls and wooden surfaces using polyurethane fiber arrays inspired by geckos as attachment pads [148]. Although these prototypes show that no residue marks are left behind, the fabrication of micro hair pads is very sophisticated, in addition, dry elastomer adhesives are very sensitive to dust and moisture [149]. It is found that, in the presence of pre-existing flaws, the adhesive strength can be optimized by size reduction to the nanoscale, gradient material design, and hierarchical energy dissipation.

On the other hand, animals like beetles, blowflies, and ants have not evolved the same attachment terminals as geckos [151]. They resort to another strategy which is based more on

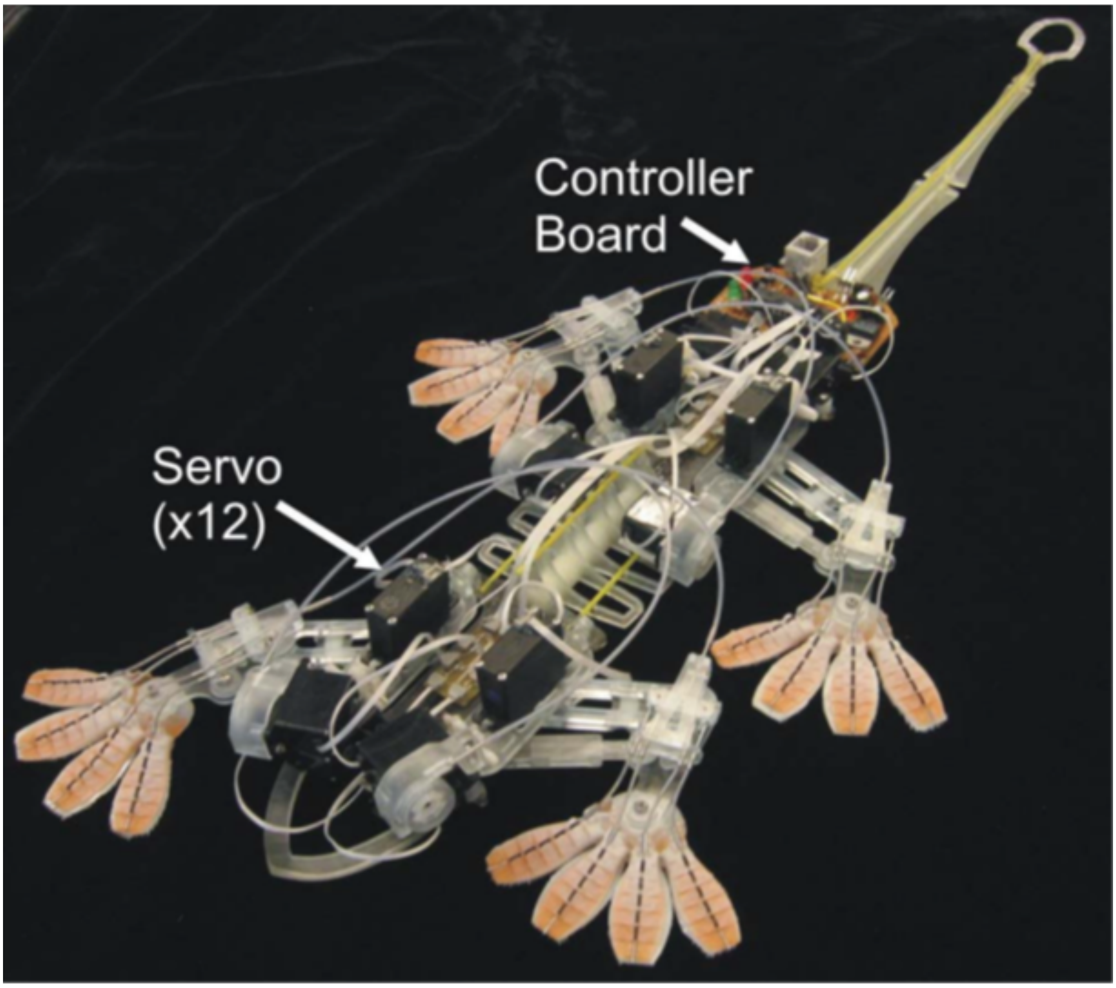

FIGURE 4.10: Stickybot, a centimeter-scale prototype that can climb on glass using gecko-inspired adhesion. [150]

wet adhesion. When they attach to surfaces, some secretory fluid is produced and delivered to the bottom of the attachment pads. The fluid footprints left behind by the animals are simply the replica pattern of their adhesive pads [152]. Recent experiments with flies have confirmed the special mechanisms for the release of secretion to individual pads. The evidence that secretion is crucial for successful attachment is provided by observations that animals appear to lose their ability to adhere to surfaces after treatments to remove secretion from their feet. There have been a number of prototypes that employed capillary adhesion due to liquid bridges in the past [153–155]. This technique is efficient for miniature climbing robots, Fig. 4.11 shows an insect-scale climbing robot navigates a circular track of 50 cm diameter by using capillary wet adhesion, the prototype only weighs 1.4 grams.

As wet adhesion depends mainly on fluid viscosity, a group of researchers proposed a novel adhesion effect based on a magnetorheological fluid [156]. Magnetorheological fluids are novel “active” or “smart” fluids composed of micron-sized iron particles suspended in an inert oil and have controllable fluidity. They exhibit low-viscosity Newtonian fluid properties in the

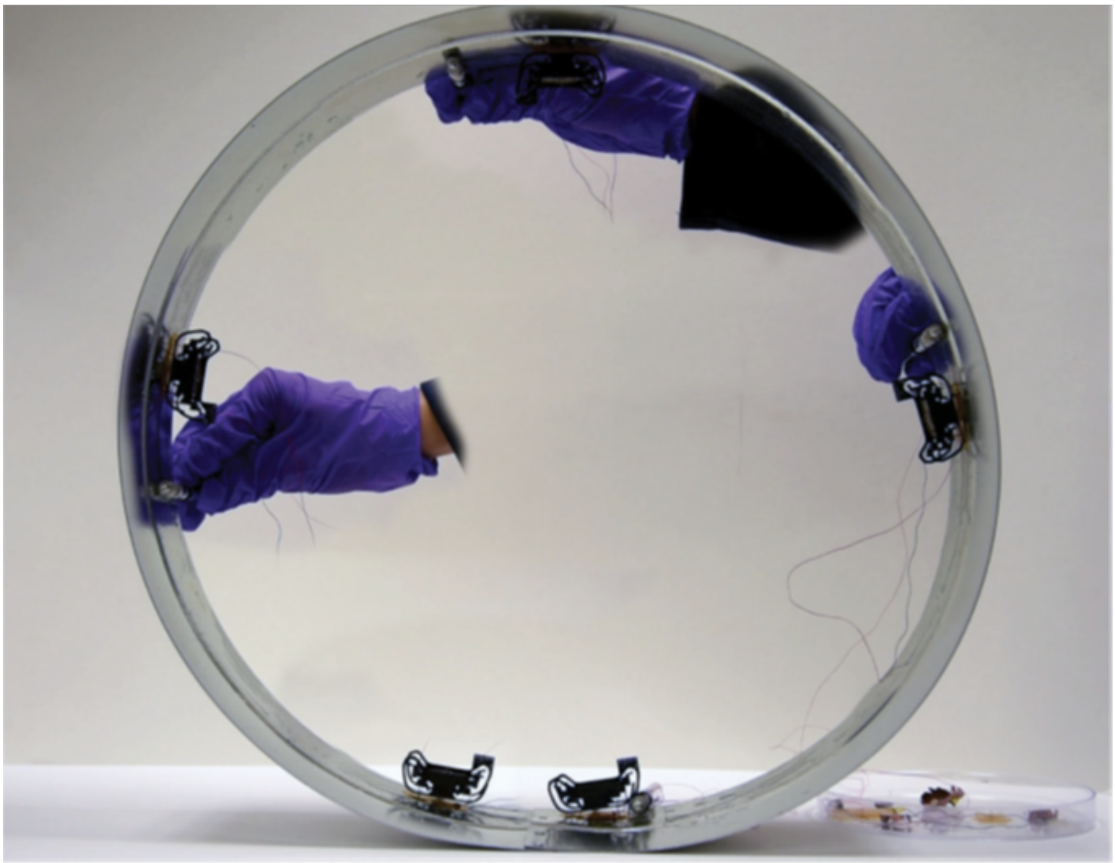

FIGURE 4.11: A 1.4 grams insect-scale prototype navigates a circular track by using capillary wet adhesion. [157]

absence of an external magnetic field, while they act as a Bingham fluid with high viscosity and low fluidity in an external magnetic field. There is a corresponding relationship between the viscosity of the liquid and the magnetic flux. This conversion consumes low amounts of energy, is easy to control, and has a rapid response to wet adhesive techniques.

In conclusion, adhesive adsorption methods, whether dry or wet, do not require an energy supply. Their disadvantage is that the adhesion force is small and, when the adhesive pad is contaminated, the adhesion effect is greatly reduced or absent, so these methods are unsuitable for outdoor use.

4.4.6 Comparative Discussion

All of the above adhesion methods have their advantages, disadvantages, and applicable scopes. Table 4.1 provides a detailed comparison among all of the reported methods.

Generally, climbing robots should be thin and light as thinner ones are harder to peel off from a vertical surface and lighter ones are more stable on the substrate compared to macro-sized robots. It is challenging and important to design a proper adhesion method guaranteeing

TABLE 4.1: Comparison of adhesive techniques

Method	Advantages	Disadvantages	Applicable Scope
Magnetic Adsorption	Large adsorption force, the permanent magnet does not need electricity	Magnets are generally heavy, which increases weight and reduces the load capacity	Ferromagnetic materials
Air Pressure Adsorption	Large adsorption force, easy to control, regardless of materials	High energy consumption, noise, large size, movement delay, poor safety	Flat, smooth non-porous and non-cracked surfaces
Mechanical Grasping	No energy consumption, no noise, high load capacity	Damages soft objects, cannot climb on inverted surfaces	Rough objects with bulges or pits
Electrostatic Adsorption	Low weight, small dimensions, low energy consumption, no noise, tunable adhesive force	Low load capacity, slow speed, sensitivity to surface conditions involving dust, requires high voltages	Uncontaminated and uncharged objects
Bio-Inspired Adhesion	No energy consumption, no noise, allows sliding adhesion	Low load capacity, slow speed, requires sophisticated control structure, needs to carry water for wet adhesion	Smooth substrate

reliable climbing on various wall surfaces whilst not sacrificing flexible mobility and large payloads. Implementing an agile and cost-effective locomotion mechanism is another significant issue associated with climbing robots. The miniaturization of designs has made climbing robots advantageous because the adhesion force with the wall becomes more dominant than the gravitational force at a small scale. That has led to a demand for an alternative adhesive as the footpad of robots, with primary requirements of minimizing energy expenditure and satisfying performance and operational scenarios such as surveillance, an inspection of large machines, and reconnaissance in multi-sort structures.

Inspired by nature, the dry adhesive concept as seen in climbing insects such as the gecko has drawn significant interest from researchers. Adhesion in geckos is attributed to micro/-nanofibrils found on its feet that rely on van der Waals forces to adhere to a surface, hence the terminology of dry adhesive. While immense progress has been made in the design and fabrication of multiscale hierarchical adhesive structures, the robustness, durability, and endurance (ability to adhere to surfaces for an extended period of time) of gecko-foot mimetic dry adhesives still lag behind their biological counterparts. In this thesis, we highlight the design considerations for the development of robust and durable cost-effective dry adhesive structures that can be used for insect-scale climbing robots.

4.5 Adhesive Material Testing and Selection

The adhesion method is a key technology for the development and application of wall climbing robots, so there has been a sustained interest in pursuing novel adhesion methods, which can benefit from their simplicity, lightweightness, and work stability. To satisfy these requirements, we employ a cost-effective approach based on using commercially available dry adhesive tapes, unlike a gecko-like dry adhesion that requires special fabrications. These tapes can provide sufficient adhesion for inverted and vertical locomotion to our robot while retaining horizontal running capabilities. The selection of adhesive material is to determine the range in which the robot moves smoothly. In other words, a too-small adhesion force cannot retain the contact between the wall and the wheels, and a too-high adhesion force stops the rotation of the wheels. Besides, how the adhesion force relates to the payload capability is analyzed together.

4.5.1 Friction Adhesion Model

Inverted and vertical locomotions require adhesive forces to be at least equal to the weight of the robot. To satisfy these requirements, eight different tapes are tested from (Nichiban and Nitto companies) to study their adhesive characteristics. The two major considerations are the normal adhesion force F_N and the tangential (shear) adhesion force F_T. Mathematically, the frictional adhesion model is given by

$$F_N = \frac{1}{\mu} F_T \tag{4.1}$$

where μ is the coefficient of friction. In general, adhesive forces are directly proportional to both adhesion strength and contact area. While no data are available for the dry adhesive tapes, the model can be evaluated experimentally. The tapes are evaluated on substrates made from Acrylonitrile Butadiene Styrene (ABS) material with a static friction coefficient of 0.59 printed by a 3D printer. All of the tapes are double-sided adhesives to be easily wrapped around the wheels. A pull-off force test is conducted initially to measure the normal adhesive force. Fig. 4.12(a) shows the experimental setup, the wheels of a driving axle are stuck to the substrate and pulled off by the force gauge. The experimental procedures are as follows; wheels, wrapped with a different adhesive tape at a time, are initially attached to the force gauge and loaded vertically to the substrate by their own weight. In other words, no additional preload is applied. In this case, the adhesion force between the wheels and the wall is similar to that of the robot

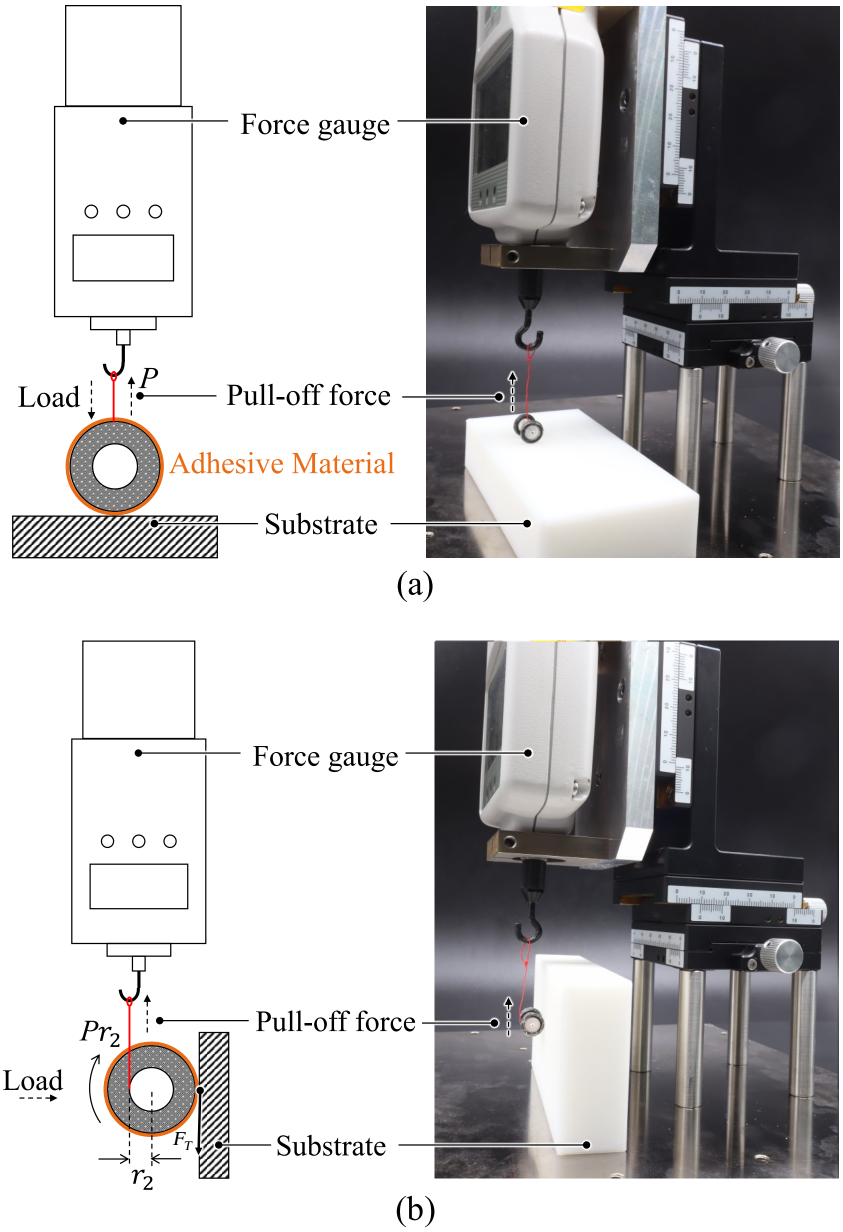
Force gauge
Load
P
Pull-off force
Adhesive Material
Substrate
Force gauge
Pull-off force
Pr_2
Load
F_T
r_2
Substrate

(a)

(b)

FIGURE 4.12: Evaluation of the friction adhesion model for the adhesive materials; (a) Normal adhesive force experiment, wheels are pulled off vertically by the force gauge until detachment from the substrate. (b) Shear adhesive force experiment, driving torque (Pr_2) is increased gradually to the point wheels start to rotate.

climbing on the wall. The force gauge, mounted on a 3-axis stage, starts then to move upward at a speed rate of 0.1 mm/s to increase the pull-off force. Maximum pull-off force P just before detachment is recorded as the normal adhesive force. Thus,

$$F_N = P \tag{4.2}$$

A test of the frictional adhesion model for the climbing robot's wheels would be to measure the ratio of F_N to F_T in actual climbing. The model can be evaluated by measuring the torque required to overcome the shear adhesive force during climbing. In this experiment, a pulley is fixed to the center of the axle, while a wire connects the pulley to a force gauge, as shown in Fig. 4.12(b). Wheels, suspended from the force gauge, are loaded on the substrate horizontally. The applied driving torque on the wheels (Pr_2) is increased gradually as the force gauge is moving upward at a speed rate of 0.2 mm/s. As a result, the wheels start to rotate. The wheel and pulley diameters are denoted as r_1 and r_2, respectively, the maximum tangential adhesive force can be calculated then using the following equation:

$$F_T = \frac{r_2}{r_1} P \tag{4.3}$$

In these experiments, when the wire is pulled upward, the wheels either rotate on the wall or detach from the wall. Thus, the slip and friction at the interface between the wheels and the wall can be ignored. The ratio of normal force to shear force is approximately 1.1:1, irrespective of the adhesive tape material. A comparison between different tapes is illustrated in Fig. 4.13.

4.5.2 Adhesive Material Durability

One notable feature in biological creatures is that they can use their adhesive techniques repeatedly without losing their adhesive performance, which allows the animal to climb surfaces for an extended period of time. The adhesive structures of biological systems have been shown in the laboratory to be reusable for over 30,000 cycles [158]. Their durability is attributed to their hierarchical design that distributes the load evenly among all setae-spatulae fibrils. This desired durability property needs to be incorporated while selecting an adhesive technique for climbing robots, allowing them to maintain their adhesive performance over numerous attachment-detachment cycles.

In contrast to biological structures, the adhesive performance of synthetic adhesives is often seen to degrade after just a few attachment-detachment cycles. The durability of an adhesive structure can be determined in most cases by evaluating its adhesive performance after repeated use and comparing it with its adhesive performance after the first attachment-detachment cycle [159]. Another approach is to examine for contamination or wear of the structures after each

Adhesive material

[a]	Nichiban NW-R15	[e]	Nitto No.5610
[b]	Nichiban NW-10	[f]	Nichiban NW-K15
[c]	Nitto No.5603	[g]	Nichiban NW-H15
[d]	Nitto No.5605	[h]	Nichiban NW-PK15

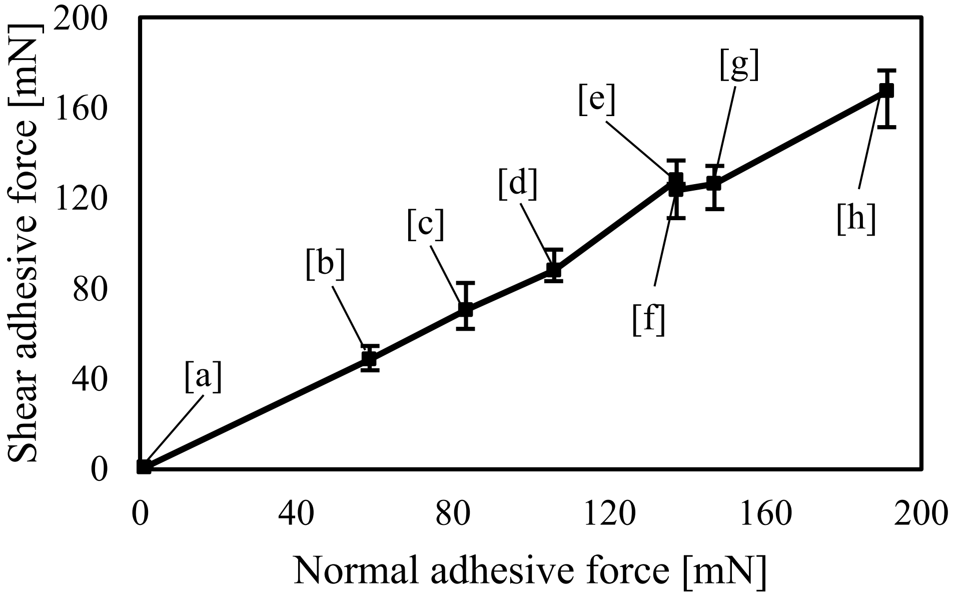

FIGURE 4.13: Adhesive forces characteristics of the tested adhesive materials. The graph shows the mean, the maximum, and the minimum data for 15 trials.

attachment-detachment cycle using a scanning electron microscope (SEM). SEM images are also taken on the target surface to determine if any residue is left over, which would suggest that the fibrils from the structures are damaged. This approach is challenging as it involves tedious analysis and difficulty in obtaining reliable data. In most cases, the degradation of the adhesive performance of synthetic structures is due to contamination and excessive preloads.

To evaluate the durability of the proposed dry adhesive materials, we employ the first durability test approach where the normal and tangential adhesive tests previously explained in the last section have been repeated consecutively for 50 cycles as depicted in Fig. 4.14. The resulting data are as follows; after 10 cycles, the adhesive forces drop around 25% and keep almost constant till 20 cycles. That is followed by a further drop of 5% for every 8 cycles for the remainder of the experimental cycles.

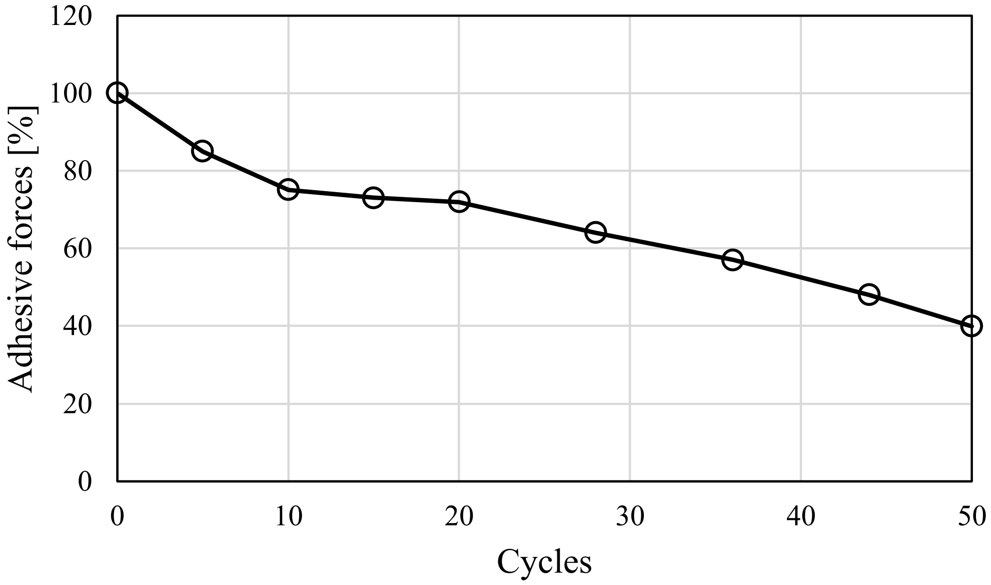

FIGURE 4.14: Durability test of the adhesive materials for 50 cycles.

4.5.3 Adhesive Material Selection

Unlike walking or running robots, a climbing robot must continually consider the control of adhesive forces whenever it is in contact with the climbing surfaces. Several parameters must be considered when the appropriate adhesive material is selected, such as the robot's weight, the amount of payload attached to the robot, the thrust force of actuators, and the tension of the wires. To enable vertical and inverted locomotion, the normal and shear adhesive forces generated by two wheels of each axle must satisfy the following conditions:

$$F_N > max\left[F_{Peel}, (\frac{m_{robot} + m_{payload}}{2})\right] \tag{4.4}$$

$$\left[\frac{m_{robot} + m_{payload}}{2}\right] < F_T < F_{thrust} \tag{4.5}$$

For the normal adhesive force (F_N), the adhesive material must withstand the extreme turnover condition while climbing (F_{Peel}) and support the total weight for inverted locomotion. The overturning moment is caused by the position of the center of gravity of the robot at a distance away from the wall, as a result, the weight of the robot tends to rotate the robot in a nose-up direction and off from the wall. Most climbing wheeled robots are fitted with a tail for countering peel moments [160], [161]. Herein, the turnover moment is controlled by synchronizing the angle between the two links with the climbing speed. The forces on the climbing robot with compliant adhesive wheels on a vertical wall are shown in Fig. 4.15. Point "A" is defined as the contact point between the rear wheel and the vertical wall as shown. At

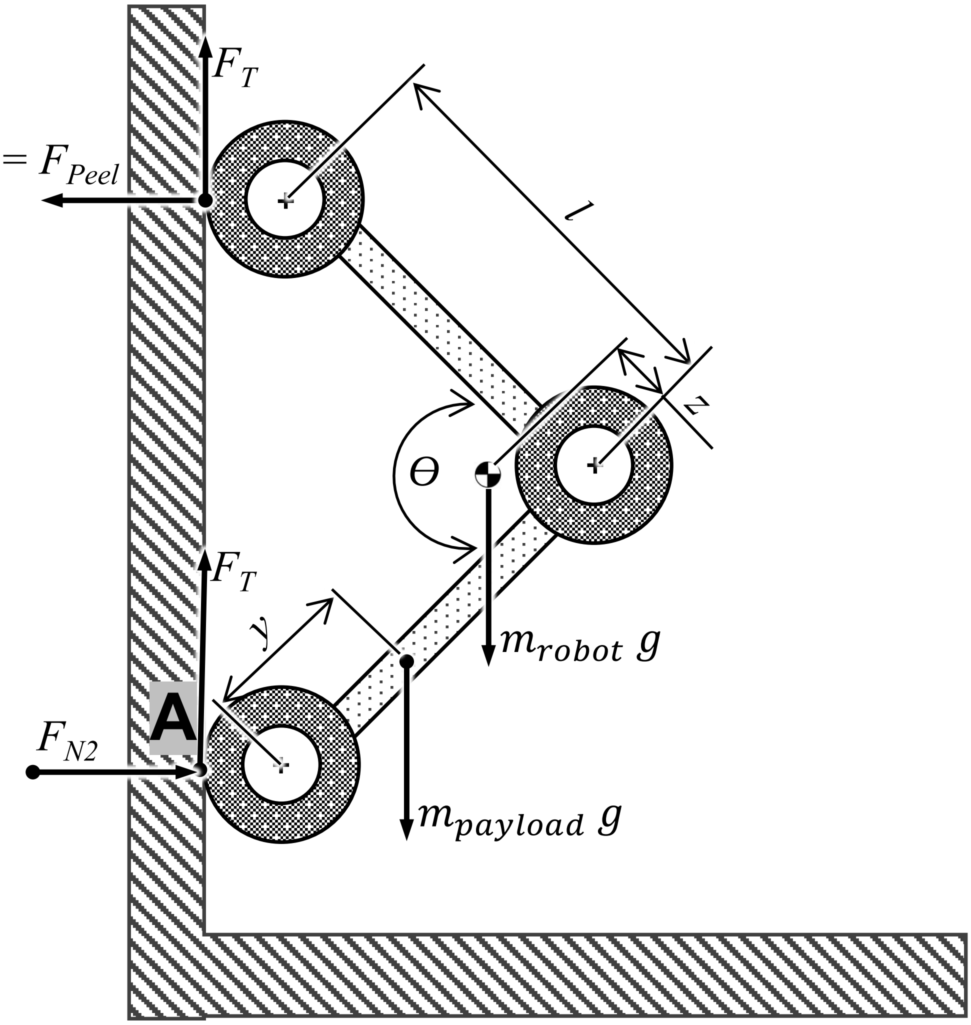

FIGURE 4.15: Schematic of the static analysis of the climbing robot in vertical navigation.

stationary, the total applied moment at point "A" can be expressed as:

$$\sum M_{\text{A}} = 0 \tag{4.6}$$

Applied moments are derived as:

$$m_{robot}\, g\, [(l - z)\cos\frac{\theta}{2} + r_1] + m_{payload}\, g\, [y\, \cos\frac{\theta}{2} + r_1] - 2\, F_{Peel}\, l\, \sin\frac{\theta}{2} = 0 \tag{4.7}$$

Where m_{robot} is the mass of the robot, $m_{payload}$ is the mass of the payload, l is the length of the link, θ is the angle between the two links, r_1 is the robot's wheel radius, y is the position of the payload along with the rear link, z is the distance between the pivot joint and the center of gravity (CG) along with the front link, and F_{Peel} is the normal adhesive force between the front wheels and the vertical wall. Thus, the minimum adhesive force to resist peel moments can be

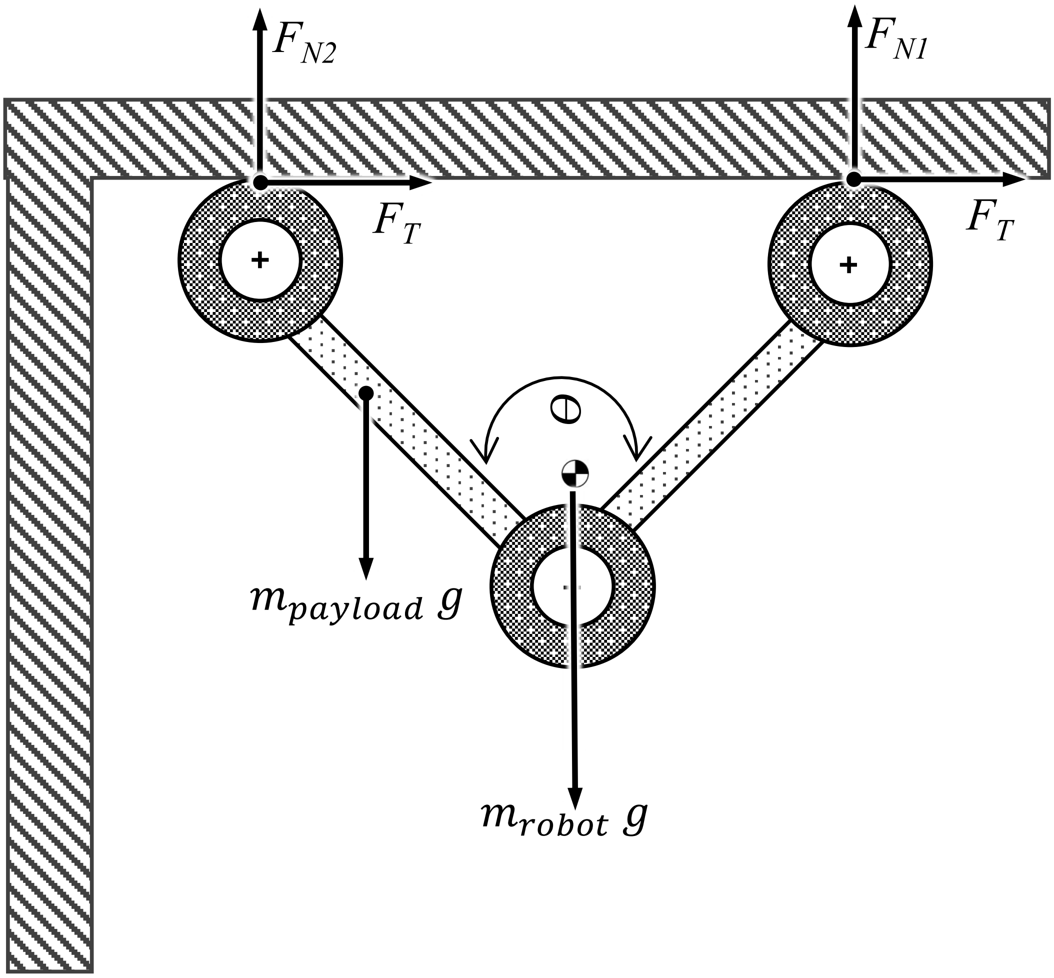

FIGURE 4.16: Schematic of the static analysis of the climbing robot in inverted navigation.

calculated as:

$$F_{Peel} > \frac{m_{robot}\, g\, [(l-z)\cos\frac{\theta}{2} + r_1] + m_{payload}\, g\, [y\ \cos\frac{\theta}{2} + r_1]}{2\, l\ \sin\frac{\theta}{2}} \tag{4.8}$$

This equation predicts that a larger θ (less folding angle) will improve the chances of success, which is compliant with the analysis in[162] which indicates that a robot with a higher body length to height ratio requires less adhesive force. Moreover, in inverted navigation as shown in Fig. 4.16, one pair of wheels must provide adhesive forces to support half of the total weight of the robot, which includes any additional payloads. By computing all of the design parameters and design constraints of a minimum folding angle (θ) of 30° in Eq. (4.8), F_N should exceed 35 mN for a zero payload. Since this calculation is derived for a stationary climbing robot, in order to compensate for the dynamic forces during locomotion, such as the wire tension, a safety factor of 2 is incorporated.

For the tangential (shear) force (F_T), the adhesive material must be larger than the robot's total weight to prevent slippage while climbing, and still, it must be less than the maximum thrust force generated by the actuators to facilitate locomotion. The thrust force can be calculated as follows:

$$F_{thrust} = \frac{T}{r_1} \tag{4.9}$$

Where T is the output torque of the geared micromotor. While the ultrasonic motor should ideally provide a maximum torque of 60 μNm, the actual thrust force was calculated in Chapter 3-Section 3.2.1, and it was found to be 95 mN. While a static analysis does not consider the inherent acceleration in the robot's motion, the selection of an adhesive material that covers the minimum condition would provide good acceleration.
Considering the two aspects (F_N and F_T), two adhesive tapes (Nitto No. 5603 and Nitto No. 5605) can be used efficiently for all the designated range of motion of the robot.

4.5.4 Lifespan Prediction of Adhesive Materials

Although in Subsection 4.5.2 the degradation of the adhesive forces was measured experimentally, it is hard to perform the same experiments while the robot is climbing in real-life scenarios. Therefore, another indication of the severe degradation of adhesive forces is needed to estimate when the climbing would fail and protect the robot from falling down. We think that there is a strong relationship between the propelling speed of the robot and the degradation of the adhesive materials, in other words, as the adhesive material starts to fail, the rolling resistance between the wheels and the surface decreases as a consequence, and that will lead to a rise in the robot's propelling speed.

To confirm our thoughts, we conduct an experiment to determine the maximum traveling distance the robot can achieve in vertical climbing on a flat surface while we closely monitored its propelling speed. The propelling speed is measured by transforming the feedback angular Velocity signal of the TMR sensor mounted on the micro-geared ultrasonic motors. The propelling speed can be computed using the following equation while assuming that no wheel slippage occurs:

$$V = \frac{\mathit{\Omega} * r_1}{G_1} \tag{4.10}$$

Where $\mathit{\Omega}$ is the angular velocity of the micro-ultrasonic motor, r_1 is the robot's wheel radius, and G_1 represents the gearbox ratio. Fig. 4.17 shows the experimental setup, the robot is initially placed on the vertical surface while all of the wheels were covered by the same adhesive material at a time. The robot starts to move upward at its full speed until the adhesive material fails. In this experiment, only the selected adhesive tapes (Nitto No. 5603 and Nitto No. 5605) are analyzed. A ruler is also attached to confirm the accuracy of the measured speed. Fig. 4.18 shows the final experimental data, the robot succeeds to navigate vertically for an approximate

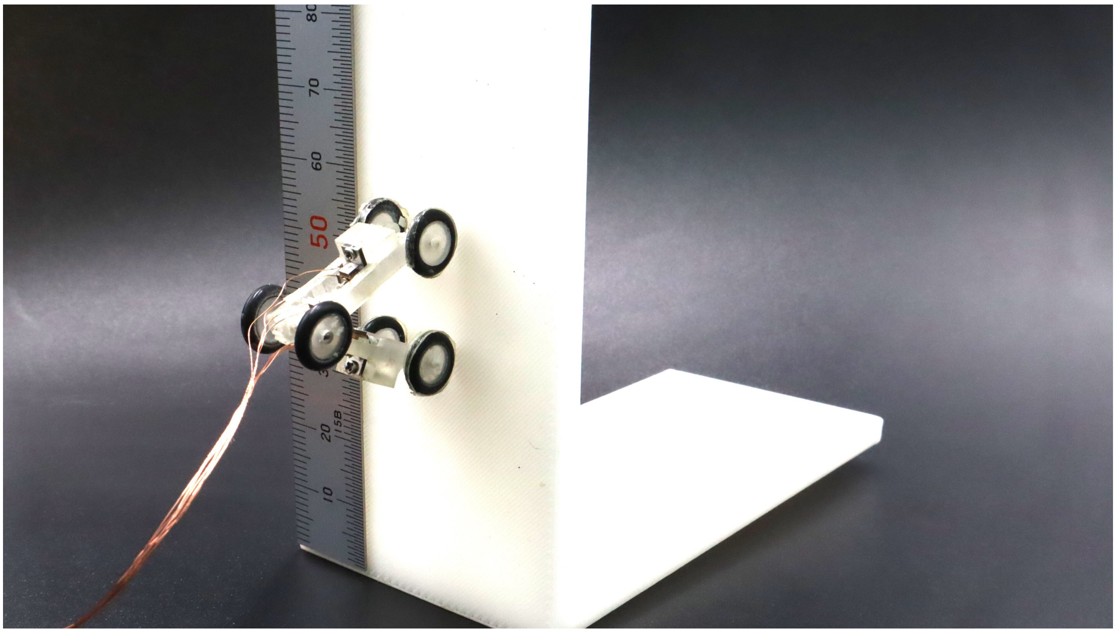

FIGURE 4.17: Experimental setup to measure the relationship between propelling speed and the degradation of adhesive forces with the traveling distance.

distance of 1600 mm when Nitto No. 5603 is used. The propelling speed increases from 4.3 to 5.9 mm/s in a linear layout as the adhesive material's forces degraded with traveling distance as expected, which represents an increment of more than 35%. The performance is slightly better when the wheels are covered by Nitto No. 5605 adhesive material as the robot could climb for 2500 mm before falling down. In this experiment, the recorded speed increases from 2.8 to 4.15 mm/s which represents an increment of almost 50%.

From the previous data, we can conclude that the propelling speed of the robot can be a good feedback indication of the degradation of the adhesive forces. As a safety measure, a new set of adhesive tapes should be fitted if the speed increases by more than 30% compared to the initial speed of the robot.

4.6 Experiments

To validate the proposed adhesion technique and the new design, several experiments are conducted to quantitatively assess different aspects of the approach including repeatability of the adhesive material, locomotion performance on multiple oriented surfaces, climbing speed, and payload capacity. All of the experimental structures are made from Acrylonitrile Butadiene Styrene (ABS) material, the same material used in the evaluation of the adhesive materials in Section 4.5. The position of the electric wires is adjusted periodically to minimize their influence.

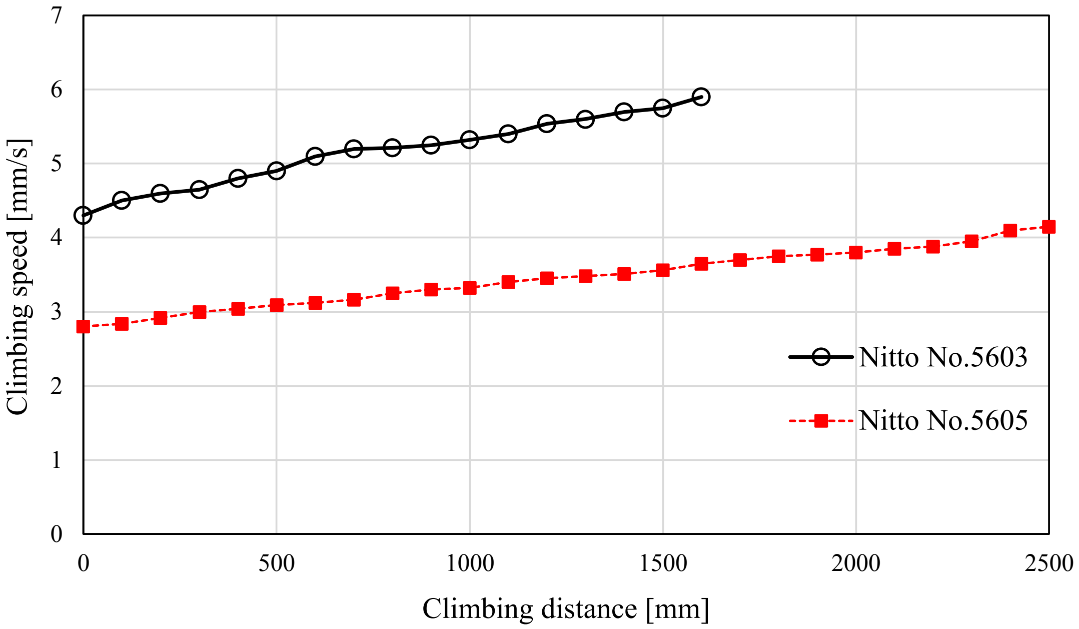

FIGURE 4.18: Variation of vertical climbing speed as the adhesive material degraded with traveling distance.

4.6.1 Climbing and Surface-to-Surface Transitions

These experiments demonstrate the design features of the climbing robot to successfully navigate complex structures. Fig. 4.19 shows snapshots of the robot's horizontal, vertical, and inverted locomotion while performing three different surface-to-surface transitions; a convex transition between vertical and horizontal surfaces, a concave transition between horizontal and vertical surfaces, and a concave transition between vertical and inverted surfaces. In the experiments, wheels are covered with Nitto No. 5603 adhesive material. The robot navigates smoothly over all the surfaces and performs all the intended transitions at an average speed of 2 mm/s without falling. Although it can go faster, we curtail the speed to prevent overheating in the actuators.

We note that, during vertical and inverted locomotion, the forces acting on the robot from the wires are quite large. This problem causes the robot to tilt around the longitudinal axis sometimes, in other words, the wheels at one side lose contact with the surface. Using a stronger adhesive material is an option, but that will affect the climbing speed for sure. Through experimental tests, one set of adhesive materials is used from the start to the finish point for every experiment. The lifespan of the adhesive materials in actual climbing matches the degradation of the adhesive forces curve generated from the repetitive testing cycles in Section 4.5. This agreement proves the potential of low-cost dry adhesive materials in the field of miniature climbing robots.

Convex transition (vertical to horizontal surfaces)

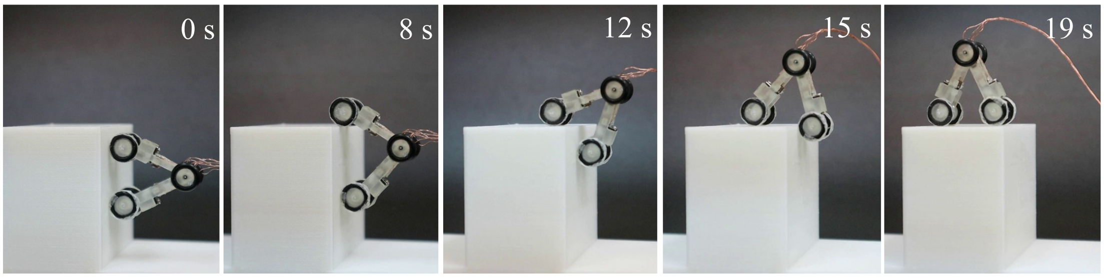

Concave transition (horizontal to vertical surfaces)

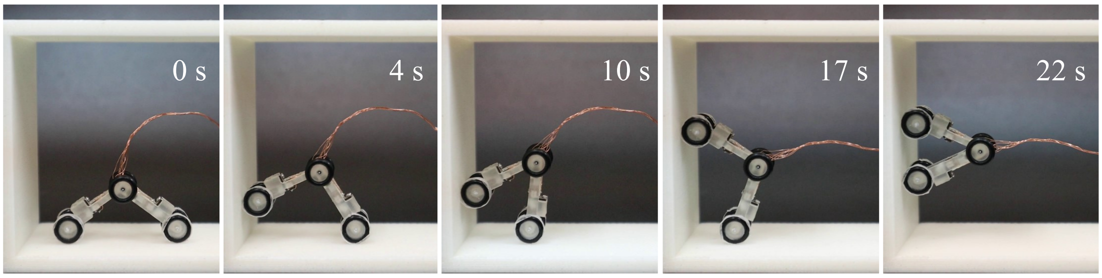

Concave transition (vertical to inverted surfaces)

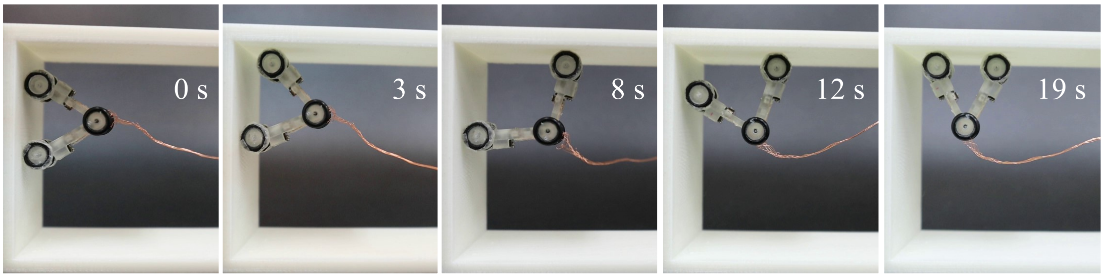

FIGURE 4.19: Demonstration of vertical and inverted climbing along with 3 different cases of surface-to-surface transitions.

These experiments outperform the performance of our previous insect-scale wheeled robot, the prototype of which is one of the smallest wheeled robots [163]. The previous prototype could climb a slope of 45°, but its design features didn't allow the merit to climb or transition between oriented surfaces.

4.6.2 Payload Capacity

The payload capacity is very promising for the climbing robot, as it demonstrates high torque density along with the adhesion material's reliability in the previous experiments. In general, the maximum payload a robot can carry while climbing is constrained mainly by the torque of the actuators and is scalable to the bonding material. Therefore, The adhesive forces in Section

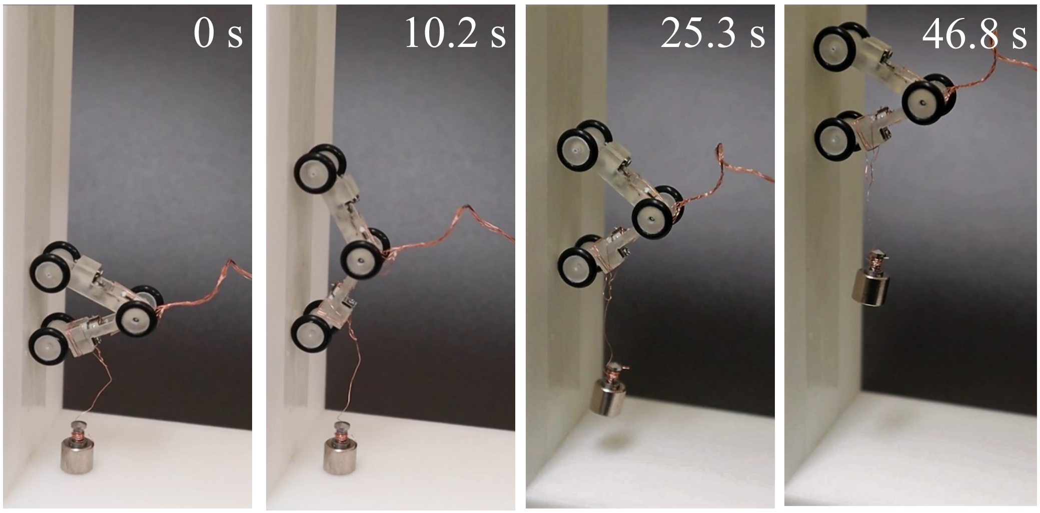

FIGURE 4.20: Demonstration of the vertical navigation of the prototype while a payload of 2 g is attached to it.

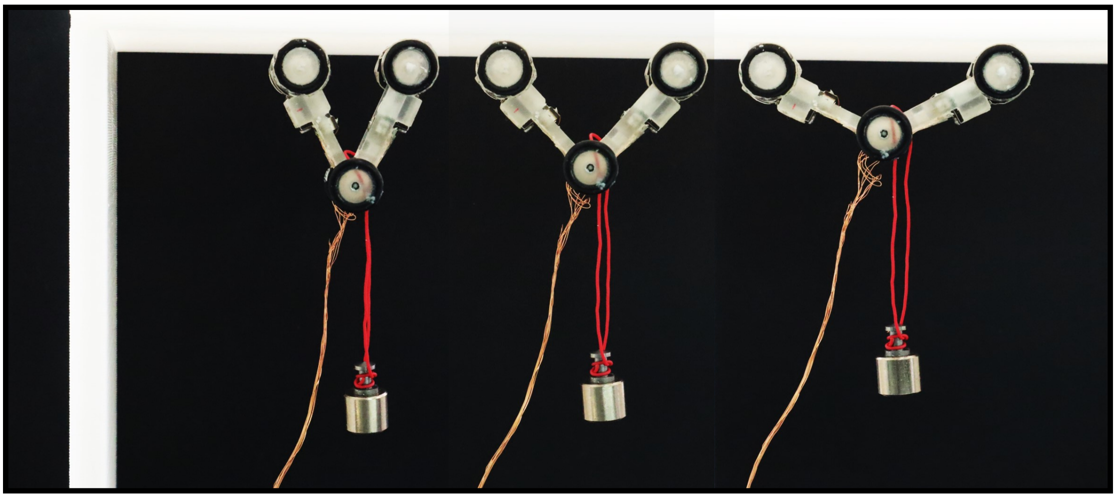

FIGURE 4.21: Snapshots of the robot in inverted navigation while carrying an extra payload, the robot finishes the task successfully.

4.5 are re-evaluated based on the payloads, and Nitto No. 5605 is selected. Fig. 4.20 shows snapshots of the robot climbing on a flat surface with an extra payload of 2 g representing 120% of its body mass. Payloads are attached to the robot at the point close to the wall to minimize turnover moment. However, the uncontrollable swing motion of the suspended weight causes the wire to interface with the adhesive material wrapped around the rear wheels. Therefore, we attach the adhesive material to the wall itself. This problem did not occur in the inverted locomotion with a payload experiment (Fig. 4.21), as gravity pulls the weights away from the adhesive wheels.

The climbing speed depends mainly on the weight of the payload. Fig. 4.22 summarizes the climbing velocity of the robot with respect to the payload capacity while the same experimental

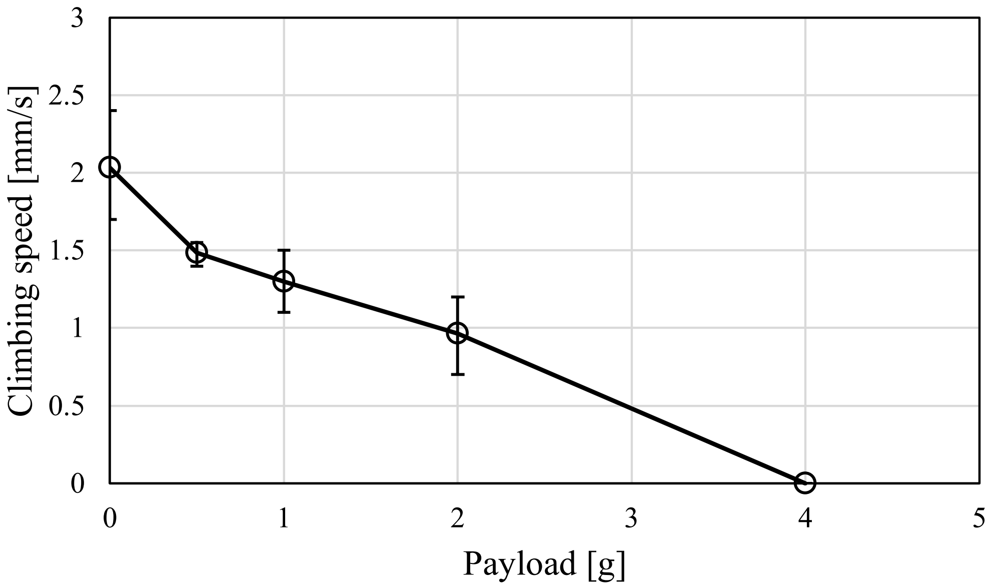

FIGURE 4.22: Variation of vertical climbing speed based on the payload weight. The graph shows the mean, the maximum, and the minimum data for 6 trials.

conditions are applied. Throughout all the experiments, the robot is reliable and requires no maintenance.

4.7 Performance Evaluation

Finally, a typical benchmark is to compare the performance of the climbing robots with similar prototypes previously reported by other researchers. Actually, only a few comparable insect-scale robots have been shown in the past 10 years. Most of them employ legged design as their mobility structures. Table 4.2 summarizes the size, mass, operating voltages, operating incline range, maximum velocity for the given incline, transitioning capabilities, and payload capacity of the prototypes. With a more compact size, Table 4.2 demonstrates the superiority of the proposed robot over all comparable prototypes in terms of overall size, transitioning capabilities, and payload capacity.

4.8 Conclusion

Climbing robots have good application potential in scenarios that are difficult or dangerous for humans to work in. The proposed approach for an insect-scale climbing robot using dry adhesives offers significant advantages due to its extraordinary performance for miniature climbing robots using simple solutions. A platform was developed for the prototype, and its fundamental characteristics were investigated experimentally. In addition, different dry adhesive materials

TABLE 4.2: Comparison between the climbing capabilities of the proposed insect-scale robot with similar prototypes.

Reference	Size [mm^3]	Mass [g]	Op. volts [V_{p-p}]	Incline range [°]	Maximum velocity [BL/s]	Trans. capabilities	Payload capacity*[%]
Greuter et al. [164]	40× 43 × 14	10	3.7	0-90	90°:0.08	N/A	N/A
Breckwoldt et al. [165]	47× N/A × N/A	22	3.7	0-180	90°:1.6 180°:1.8	Concave	25
D. de Rivaz et al.[115]	45 × 40 × 20	1.48	250	0-180	0°:3.1 90°:0.026 180°:0.1	N/A	N/A
This work	40× 10 × 7	1.7	120	0-180	0°:0.3 90°:0.1 180°:0.05	Concave/ Convex	120

*Payload capacity = (payload mass/robot mass)×100.

were analyzed and the selection criteria for the appropriate adhesive material to cover the full range of motion were also demonstrated.

In the experiments, the prototype proved its viability to navigate complex structures (vertically and invertedly) while performing different cases of surface-to-surface transitions. A payload-mass ratio of 120% was achieved while climbing on a vertical surface. Despite gravitational force, the high torque-to-weight ratio enables the proposed robot to do new tasks using simple solutions. The ability to complete these tasks proves the functionality of the design and the effectiveness of low-cost dry adhesive materials, as it demonstrates an unprecedented mobility performance for an insect-scale climbing robot.

Chapter 5

Conclusion and Future Work

5.1 Conclusion

In this thesis, we introduced the next generation of borescopic inspection tools for complex machines. The main problem with the current borescopes is that they are extrinsically manually actuated by an operator, which makes it hard to point their tips to a specific spot. One of the main reasons is the absence of a powerful actuator in a micro-scale to be fitted in the borescope tip. Many researchers believed that a miniature mobile robot capable of navigating inside narrow tubes and pipelines efficiently could be the next generation of borescopes. This thesis outlined some of the challenges related to the development and implementation of an insect-scale in-pipe robot and presented solutions that lead to extending the working domain of the robot to a new era.

The first challenge is the driving mechanism, downsizing an actuator to a micro size comes with a lot of problems. Piezoelectric ultrasonic motors outperform electromagnetic actuators at such a scale because of their high power density and good machinability. However, despite their great scalability, they have obvious nonlinear and time-varying characteristics that deteriorate their performance in prolonged operations. We investigated that problem by studying the effectiveness of the motor's internal parameter changes, such as a temperature rise and the resonant frequency variation. For that, a mathematical model was derived from scratch to model the non-linear temperature-dependent characteristics of ultrasonic motors followed by several experiments to verify the hypothesis experimentally. The model and the experiments confirmed that the internal losses of the motor could raise the temperature of the motor which results in some deviation in the motor's parameters such as the natural frequency. The experiments also prove that such deviation affected the motor performance by enlarging its steady-state error with time. To solve this dilemma, we introduced a model-free, real-time-adaptive extremum-seeking controller (ESC) that can coop with the non-linear characteristics of the motor. To build the control structure, we constructed the smallest rotary actuator-sensor system in the world consisting of a micro-ultrasonic motor, a tiny TMR sensor, and a tiny magnet. The resulting system was assembled into a size with a height of 3.2 mm, a width of 3.2 mm, and a length of 5 mm. Several experiments that involve constant and variable speed commands show that the controller succeeded in driving the motor at the desired angular velocity with a minimum steady-state error by continuously tracking and localizing the optimum driving frequency.

The second challenge is the design itself of the robot. An inspection robot is expected to reach inaccessible areas by navigation in confined places including inside narrow tubes and pipelines in harsh working environments. To fulfill these requirements, we have taken design principles adapted from the caterpillar. The caterpillar's prowess is due to a combination of design features that work together to permit rapid and smooth locomotion. The alternation of fastening between the front and rear legs generates linear locomotion. This functionality is achieved by the proposed robot by a light rigid structure made of 2 links connected by an active pivot joint that allows the climbing robot to extend and flex. The robot has six wheels in total, a pair of active wheels at each end to drive the robot, while two passive wheels are attached to the pivot joint. The pivot joint enables the robot to navigate inside a wide range of pipelines from 12 to 25 mm by changing its height. The joint also allows the robot to exert a force against the upper walls for holding the robot inside the pipes, which can be treated as an integrated holding force mechanism. The tire's stiffness is advantageous to increase the contact area and the traction force of the robot without any extra equipment. On a flat surface, the robot moves at a maximum speed of 12.3 mm/s when 120 $\mathrm{V_{p-p}}$ input voltages are applied at the resonant frequency. The robot demonstrated its high mobility power by pulling 10 g of weight (six times its own weight) at a speed of 4 mm/s. In addition, two locomotion modes to propel inside pipelines are presented, and a proposed motion strategy to navigate complex pipe configurations, including vertical and bent pipes, is presented and validated by a series of experiments.

To extend the working domain of the inspection robot, we study the possibility of merging the robot with an adhesion mechanism to perform more challenging tasks such as replacing manual inspection at heights. For that, numerous adhesion methods were investigated until we came up with an approach of using low-cost dry adhesive materials to address climbing challenges, including surface-to-surface transitions, and vertical and inverted locomotion with high payload capacity. This idea was inspired by the climbing action of caterpillars on vertical surfaces as stationary legs provide anchoring force to hold their weight. In addition, different dry adhesive materials were analyzed and the selection criteria for the appropriate adhesive material to cover the full range of motion were also demonstrated. Final experiments prove the viability of the insect-scale robot to navigate complex structures (vertically and invertedly) while performing different cases of surface-to-surface transitions. A payload-mass ratio of 120% was also achieved while climbing on vertical and inverted surfaces.

The findings of this thesis prove the functionality of the insect-scale robot for various maintenance tasks and it also demonstrates the potential of low-cost dry adhesive materials in the field of miniature climbing robots. Using the concept of mimicking the locomotion pattern of biological creatures results in an unprecedented mobility performance for an insect-scale robot.

5.2 Future Work

There are opportunities for further research and development for the insect-scale robot. For example, the optimum performance of the micro-ultrasonic motors has not yet been fully achieved. Still, we have achieved one step ahead in fully controlling the nonlinear characteristics of ultrasonic motors. Future work will address new potential causes for the performance deterioration and will also study the effect of combining input voltages and frequency as the control parameters for the ESC, a system well known as the hybrid or dual control approach. Other model-free adaptive control strategies can be also investigated for the proposed system in the future. Longer operating periods will also be considered, and that will cover other operating factors affected by the temperature such as the coefficient of friction at stator-rotor interference. Other non-linear properties of ultrasonic motors such as hysteresis will be also investigated for more performance improvement.

Another opportunity for improvement is the design of the insect-scale robot itself. The current design showed limitations in some experiments that's why we plan to fit the front wheels with a steering system to change the robot's heading direction. We will also consider using foldable links that allow longitudinal rotation to minimize the tilt problem caused by the electric wires in some experiments. Finally, the practical usage of the robot in real in-pipe and out-pipe inspection tasks demands the development of a recognition system that consists of a micro camera for self-navigation capabilities.

References

[1] Chao Tang, Boyuan Du, Songwen Jiang, Qi Shao, Xuguang Dong, Xin-Jun Liu, and Huichan Zhao. A pipeline inspection robot for navigating tubular environments in the sub-centimeter scale. *Science Robotics*, 7(66):eabm8597, 2022.

[2] Mohd Zamzuri Ab Rashid, Mohd Fitri Mohd Yakub, Sheikh Ahmad Zaki bin Shaikh Salim, Normaisharah Mamat, Sharifah Munawwarah Syed Mohd Putra, and Shairatul Akma Roslan. Modeling of the in-pipe inspection robot: A comprehensive review. *Ocean Engineering*, 203:107206, 2020.

[3] Ata Jahangir Moshayedi, Saeed Safara Fard, Liefa Liao, and Seyed Ali Eftekhari. Design and development of pipe inspection robot meant for resizable pipe lines. *International Journal of Robotics and Control*, 2(1):25–35, 2019.

[4] André Cid, Mateus Nazário, Mauricio Sathler, Frederico Martins, Jaco Domingues, Mário Delunardo, Paulo Alves, Rodrigo Teotônio, Luiz Guilherme Barros, Adriano Rezende, et al. A simulated environment for the development and validation of an inspection robot for confined spaces. *2020 Latin American Robotics Symposium, 2020 Brazilian Symposium on Robotics and 2020 Workshop on Robotics in Education,* 1–6, 2020.

[5] Ankush Verma, Ayush Kaiwart, Nikhil Dhar Dubey, Farman Naseer, and Swastik Pradhan. A review on various types of in-pipe inspection robot. *Materials Today*, 50:1425–1434, 2022.

[6] Wen Zhao, Mitsuhiro Kamezaki, Kaoru Yamaguchi, Minoru Konno, Akihiko Onuki, and Shigeki Sugano. A wheeled robot chain control system for underground facilities inspection using visible light communication and solar panel receivers. *IEEE/ASME Transactions on Mechatronics*, 27(1):180–189, 2021.

[7] Jose Luis Otegui. Challenges to the integrity of old pipelines buried in stable ground. *Engineering Failure Analysis*, 42:311–323, 2014.

[8] Keichi Kusunose, Tetsuya Akagi, Shujiro Dohta, Wataru Kobayashi, and Kengo Nakagawa. Development of pipe holding mechanism and bending unit using extension type

flexible actuator for flexible pipe inspection robot. *International Journal of Mechanical Engineering and Robotics Research*, 8(1):129–134, 2019.

[9] Kavel Visrodia and Bret T Petersen. Borescope examination: Is there value in visual assessment of endoscope channels? *Gastrointestinal Endoscopy*, 88(4):620–623, 2018.

[10] Jonas Aust and Dirk Pons. Bowtie methodology for risk analysis of visual borescope inspection during aircraft engine maintenance. *Aerospace*, 6(10):110, 2019.

[11] George H Mills, Andrew E Jackson, and Robert C Richardson. Advances in the inspection of unpiggable pipelines. *Robotics*, 6(4):36, 2017.

[12] Wasim MF Al-Masri, Mamoun F Abdel-Hafez, and Mohammad A Jaradat. Inertial navigation system of pipeline inspection gauge. *IEEE Transactions on Control Systems Technology*, 28(2):609–616, 2018.

[13] Chang Liu, Yungang Wei, Yuguang Cao, Shihua Zhang, and Yongtai Sun. Traveling ability of pipeline inspection gauge (PIG) in elbow under different friction coefficients by 3d fem. *Journal of Natural Gas Science and Engineering*, 75:103134, 2020.

[14] Website of rico-gmbh corporation. https://www.rico-gmbh.de/kempten/en/fw150s/. Accessed: 2023-04-27 [Online].

[15] Website of forbest corporation. https://www.forbestusa.com/blogs/resources/the-weasel-1-full-scope-robotic-inspection-crawler. Accessed: 2023-04-28 [Online].

[16] Dongtian Zheng, Haishu Tan, and Fuqiang Zhou. A design of endoscopic imaging system for hyper long pipeline based on wheeled pipe robot. *American Institute of Physics Conference,* 1820(1):060001, 2017.

[17] Zhipeng Wu, Yao Wu, Siyu He, and Xiaohui Xiao. Hierarchical fuzzy control based on spatial posture for a support-tracked type in-pipe robot. *Transactions of the Canadian Society for Mechanical Engineering*, 44(1):133–147, 2019.

[18] Michał Ciszewski, Tomasz Buratowski, and Mariusz Giergiel. Modeling, simulation and control of a pipe inspection mobile robot with an active adaptation system. *IFAC-PapersOnLine*, 51(22):132–137, 2018.

[19] Vanni Consumi, Jeref Merlin, Lukas Lindenroth, Danail Stoyanov, and Agostino Stilli. A novel soft shape-shifting robot with track-based locomotion for in-pipe inspection. *ArXiv Preprint*, 2022.

[20] Sergei Savin and Ludmila Vorochaeva. Footstep planning for a six-legged in-pipe robot moving in spatially curved pipes. *International Siberian Conference on Control and Communications,* 1–6, 2017.

[21] Sergei Savin, Sergey Jatsun, and Ludmila Vorochaeva. State observer design for a walking in-pipe robot. *MATEC Web of Conferences,* 161:03012, 2018.

[22] Koutaro Hayashi, Tetsuya Akagi, Shujiro Dohta, Wataru Kobayashi, Takashi Shinohara, Keichi Kusunose, and Mohd Aliff. Improvement of pipe holding mechanism and inchworm type flexible pipe inspection robot. *International Journal of Mechanical Engineering and Robotics Research*, 9(6):894–899, 2020.

[23] K Kusunose, T Akagi, S Dohta, W Kobayashi, T Shinohara, Y Hane, K Hayashi, and M Aliff. Development of inchworm type pipe inspection robot using extension type flexible pneumatic actuators. *International Journal of Automotive and Mechanical Engineering*, 17(2):8019–8028, 2020.

[24] Tomonari Yamamoto, Masashi Konyo, and Satoshi Tadokoro. A high-speed locomotion mechanism using pneumatic hollow-shaft actuators for in-pipe robots. *IEEE/RSJ International Conference on Intelligent Robots and Systems,* 4724–4730, 2015.

[25] Tomonari Yamamoto, Masashi Konyo, Kenjiro Tadakuma, and Satoshi Tadokoro. High-speed sliding-inchworm motion mechanism with expansion-type pneumatic hollow-shaft actuators for in-pipe inspections. *Mechatronics*, 56:101–114, 2018.

[26] Jinwan Lim, Hyunjun Park, Jaemin An, Yeh-Sun Hong, Byungkyu Kim, and Byung-Ju Yi. One pneumatic line based inchworm-like micro robot for half-inch pipe inspection. *Mechatronics*, 18(7):315–322, 2008.

[27] Minoru Takagi, Kazunari Yoshida, Hiroyuki Hoshino, Riichiro Tadakuma, Yoshiyuki Suzuri, and Hidemitsu Furukawa. Sliding walk with friction control of double-network gel on feet of inchworm robot. *Frontiers in Mechanical Engineering,* 5:44, 2019.

[28] Hami Tourajizadeh, Vahid Boomeri, M Rezaei, and A Sedigh. Dynamic optimization of a steerable screw in-pipe inspection robot using HJB and turbine installation. *Robotica*, 38(11):2001–2022, 2020.

[29] Tao Ren, Yin Zhang, Yujia Li, Yonghua Chen, and Qingyou Liu. Driving mechanisms, motion, and mechanics of screw drive in-pipe robots: A review. *Applied Sciences*, 9(12): 2514, 2019.

[30] Hami Tourajizadeh, M Rezaei, and AH Sedigh. Optimal control of screw in-pipe inspection robot with controllable pitch rate. *Journal of Intelligent & Robotic Systems*, 90: 269–286, 2018.

[31] Toshio Takayama, Hirozumi Takeshima, Tomoyuki Hori, and Toru Omata. A twisted bundled tube locomotive device proposed for in-pipe mobile robot. *IEEE/ASME Transactions on Mechatronics*, 20(6):2915–2923, 2015.

[32] George H Mills, Jason HW Liu, Bilal Y Kaddouh, Andrew E Jackson, and Robert C. Richardson. Miniature magnetic robots for in-pipe locomotion. *Robotics Transforming the Future: Proceedings of CLAWAR 2018: The 21st International Conference on Climbing and Walking Robots and the Support Technologies for Mobile Machines,* 289–300, 2018.

[33] Hoon Lim, Jae Youn Choi, Young Sik Kwon, Eui-Jung Jung, and Byung-Ju Yi. Slam in indoor pipelines with 15mm diameter. *IEEE International Conference on Robotics and Automation,* 4005–4011, 2008.

[34] Masashi Kamata, Shota Yamazaki, Yuki Tanise, Yasuyuki Yamada, and Taro Nakamura. Development of pneumatically driven peristaltic-type robot for long distance inspection in half-inch pipes. *IEEE International Conference on Advanced Intelligent Mechatronics,* 309–314, 2017.

[35] Tao Zheng, Xiang Wang, Hui Li, Chuan Zhao, Zhihong Jiang, Qiang Huang, and Marco Ceccarelli. Design of a robot for inspecting the multishape pipeline systems. *IEEE/ASME Transactions on Mechatronics*, 27(6):4608–4618, 2022.

[36] Edward P Furlani. Permanent magnet and electromechanical devices: materials, analysis, and applications. *Academic Press*, San Diego, CA 2001.

[37] K. Dermitzakis, J. P. Carbajal, and J. H. Marden. Scaling laws in robotics. *Procedia Computer Science*, 7:250–252, 2011.

[38] T. Morita. Miniature piezoelectric motors. *Sensors and Actuators A: Physical*, 103(3): 291–300, 2003.

[39] Weihao Ren, Lin Yang, Chengcheng Ma, Xiaoniu Li, and Jiaojiao Zhang. Output performance simulation and contact analysis of traveling wave rotary ultrasonic motor based on adina. *Computers & Structures*, 216:15–25, 2019.

[40] Toshiiku Sashida and Takashi Kenjo. Introduction to ultrasonic motors. United States, 1993.

[41] Kenji Uchino. Piezoelectric ultrasonic motors: Overview. *Smart Materials and Structures*, 7(3):273–285, 1998.

[42] Yuxin Peng, Yulong Peng, Xiaoyi Gu, Jian Wang, and Haoyong Yu. A review of long range piezoelectric motors using frequency leveraged method. *Sensors and Actuators A: Physical*, 235:240–255, 2015.

[43] Tobias Hemsel and Jörg Wallaschek. Survey of the present state of the art of piezoelectric linear motors. *Ultrasonics*, 38(1-8):37–40, 2000.

[44] Chunsheng Zhao. *Ultrasonic motors: Technologies and applications*. Springer Science & Business Media, 2011.

[45] K Uchino, S Cagatay, B Koc, S Dong, P Bouchilloux, and M Strauss. Micro piezoelectric ultrasonic motors. *Journal of Electroceramics*, 13:393–401, 2004.

[46] Tien-Chi Chen, Chih-Hsien Yu, and Mi-Ching Tsai. A new driver based on dual-mode frequency and phase control for traveling-wave type ultrasonic motor. *Energy Conversion and Management*, 49(10):2767–2775, 2008.

[47] Yunlai Shi and Chunsheng Zhao. A new standing-wave-type linear ultrasonic motor based on in-plane modes. *Ultrasonics*, 51(4):397–404, 2011.

[48] Takuma Nishimura, Hiroshi Hosaka, and Takeshi Morita. Resonant-type smooth impact drive mechanism (SIDM) actuator using a bolt-clamped langevin transducer. *Ultrasonics*, 52(1):75–80, 2012.

[49] Qiao Sheng Pan, Liang Guo He, Cheng Liang Pan, Guang Jun Xiao, and Zhi Hua Feng. Resonant-type inertia linear motor based on the harmonic vibration synthesis of piezoelectric bending actuator. *Sensors and Actuators A: Physical*, 209:169–174, 2014.

[50] Xiaoyan Hou, Heow Pueh Lee, Chong Jin Ong, and Siak Piang Lim. Development and numerical characterization of a new standing wave ultrasonic motor operating in the 30–40 kHz frequency range. *Ultrasonics*, 53(5):928–934, 2013.

[51] Zhen Liu, Qianwei Fu, Peng Yang, Zhiyan Dong, Lihua Zhang, and Zhiyuan Yao. Design and performance evaluation of a miniature i-shaped linear ultrasonic motor with two vibrators. *Ultrasonics*, 131:106965, 2023.

[52] Jörg Wallaschek. Contact mechanics of piezoelectric ultrasonic motors. *Smart Materials and Structures*, 7(3):369–381, 1998.

[53] Shiyang Li, Wenchu Ou, Ming Yang, Chao Guo, Cunyue Lu, and Junhui Hu. Temperature evaluation of traveling-wave ultrasonic motor considering interaction between temperature rise and motor parameters. *Ultrasonics*, 57:159–166, 2015.

[54] Qibao Lv, Zhiyuan Yao, Lifeng Zhou, and Lingyong Pan. Effect of temperature rise on characteristics of a standing wave ultrasonic motor. *Journal of Intelligent Material Systems and Structures*, 30(6):855–868, 2019.

[55] Shiyang Li, Deyue Li, Ming Yang, and Wenwu Cao. Parameters identification and contact analysis of traveling wave ultrasonic motor based on measured force and feedback voltage. *Sensors and Actuators A: Physical*, 284:201–208, 2018.

[56] Jinbang Li, Shuaishuai Zeng, Shuo Liu, Ningning Zhou, and Tao Qing. Tribological properties of textured stator and ptfe-based material in travelling wave ultrasonic motors. *Friction*, 8(2):301–310, 2020.

[57] Singiresu S Rao and Fook Fah Yap. Mechanical vibrations, 5th eddition, 2010.

[58] Zheng Li, Hui Zhao, Shuai Che, Xuetong Chen, and Hexu Sun. Analysis of preload of three-stator ultrasonic motor. *Micromachines*, 13(1):5, 2021.

[59] Wenchu Ou, Ming Yang, Fan Meng, Zihao Xu, Xiaoqi Zhuang, and Shiyang Li. Continuous high-performance drive of rotary traveling-wave ultrasonic motor with water cooling. *Sensors and Actuators A: Physical*, 222:220–227, 2015.

[60] S W. Chung, KT Chau. Servo speed control of traveling-wave ultrasonic motors using pulse width modulation. *Electric Power Components and Systems*, 29(8):707–722, 2001.

[61] IA Renteria Marquez and V Bolborici. A dynamic model of the piezoelectric traveling wave rotary ultrasonic motor stator with the finite volume method. *Ultrasonics*, 77:69–78, 2017.

[62] Thomas Sattel. Dynamics of ultrasonic motors. PhD thesis, Technische Universität Darmstadt, Germany, 2002.

[63] T. Mashimo and K. Terashima. Dynamic analysis of an ultrasonic motor using point contact model. *Sensors and Actuators A: Physical*, 233:15–21, 2015.

[64] S. Furuya, T. Maruhashi, Y. Izuno, and M. Nakaoka. Load-adaptive frequency tracking control implementation of two-phase resonant inverter for ultrasonic motor. *IEEE Transactions on Power Electronics*, 7(3):542–550, 1992.

[65] Wenyu Liang, Jun Ma, Cailin Ng, Qinyuan Ren, Sunan Huang, and Kok Kiong Tan. Optimal and intelligent motion control scheme for an ultrasonic-motor-driven xy stage. *Mechatronics*, 59:127–139, 2019.

[66] Zhiwei Fang, Tianyue Yang, Yuanfei Zhu, Shiyang Li, and Ming Yang. Velocity control of traveling-wave ultrasonic motors based on stator vibration amplitude. *Sensors*, 19(23):5326, 2019.

[67] Sarah Makarem, Bülent Delibas, and Burhanettin Koc. Data-driven tuning of pid controlled piezoelectric ultrasonic motor. *Actuators*, 10(7):148, 2021.

[68] Shi Jingzhuo, Huang Wenwen, and Zhou Ying. T–S fuzzy control of travelling-wave ultrasonic motor. *Journal of Control, Automation and Electrical Systems*, 31(2):319–328, 2020.

[69] Fatima Zohra Kebbab, Djamel Eddine Chouaib Belkhiat, Dalel Jabri, and Saâd Belkhiat. Frequency speed control of rotary travelling wave ultrasonic motor using fuzzy controller. *Engineering, Technology & Applied Science Research*, 8(4):3276–3281, 2018.

[70] Abdullah Mustafa, Tatsuki Sasamura, and Takeshi Morita. Robust speed control of ultrasonic motors based on deep reinforcement learning of a lyapunov function. *IEEE Access*, 10:46895–46910, 2022.

[71] Shi Jingzhuo and Wenwen Huang. Model reference adaptive iterative learning speed control for ultrasonic motor. *IEEE Access*, 8:181815–181824, 2020.

[72] Gangfeng Yan. Design of adaptive sliding mode controller applied to ultrasonic motor. *Assembly Automation*, 42(1):147–154, 2021.

[73] Darryl DeHaan and Martin Guay. Extremum-seeking control of state-constrained nonlinear systems. *Automatica*, 41(9):1567–1574, 2005.

[74] Jorge I Poveda and Miroslav Krstić. Nonsmooth extremum seeking control with user-prescribed fixed-time convergence. *IEEE Transactions on Automatic Control*, 66(12): 6156–6163, 2021.

[75] Gerardo Lara-Cisneros, Denis Dochain, and José Alvarez-Ramírez. Model based extremum-seeking controller via modelling-error compensation approach. *Journal of Process Control*, 80:193–201, 2019.

[76] Martin Guay and Denis Dochain. A proportional-integral extremum-seeking controller design technique. *Automatica*, 77:61–67, 2017.

[77] Denis Dochain, Michel Perrier, and Martin Guay. Extremum seeking control and its application to process and reaction systems: A survey. *Mathematics and Computers in Simulation*, 82(3):369–380, 2011.

[78] Ying Tan, William H Moase, Chris Manzie, Dragan Nešić, and Iven MY Mareels. Extremum seeking from 1922 to 2010. *29th Chinese Control Conference*, 14–26, 2020.

[79] Dragan Nesic, Alireza Mohammadi, and Chris Manzie. A framework for extremum seeking control of systems with parameter uncertainties. *IEEE Transactions on Automatic Control*, 58(2):435–448, 2012.

[80] Miroslav Krstić. Performance improvement and limitations in extremum seeking control. *Systems & Control Letters*, 39(5):313–326, 2000.

[81] Erkin Dinçmen, Bilin Aksun Güvenç, and Tankut Acarman. Extremum-seeking control of abs braking in road vehicles with lateral force improvement. *IEEE Transactions on Control Systems Technology*, 22(1):230–237, 2012.

[82] Dobrivoje Popovic, Mrdjan Jankovic, Steve Magner, and Andrew R Teel. Extremum seeking methods for optimization of variable cam timing engine operation. *IEEE Transactions on Control Systems Technology*, 14(3):398–407, 2006.

[83] Milos S Stankovic and Dusan M Stipanovic. Stochastic extremum seeking with applications to mobile sensor networks. *American Control Conference*, 5622–5627, 2009.

[84] Nicu Bizon. On tracking robustness in adaptive extremum seeking control of the fuel cell power plants. *Applied Energy*, 87(10):3115–3130, 2010.

[85] Takefumi Kanda, Hiraku Maeda, and Koichi Suzumori. A micro ultrasonic motor controlled by using a built-in micro magnetic encoder. *IEEE/ASME International Conference on Advanced Intelligent Mechatronics*, 1029–1034, 2010.

[86] S Toyama and U Nishizawa. Mesh robot developed by micro ultrasonic motor. *ACTUATOR 2018; 16th International Conference on New Actuators*, 1–4, 2018.

[87] Website of new scale technologies. https://www.newscaletech.com/micro-motion-modules/m3-rs-rotary-smart-stages/. Accessed: 2023-01-18 [online].

[88] Ryan St. Pierre and Sarah Bergbreiter. Toward autonomy in sub-gram terrestrial robots. *Annual Review of Control, Robotics, and Autonomous Systems*, 2:231–252, 2019.

[89] Robert J Wood. The first takeoff of a biologically inspired at-scale robotic insect. *IEEE Transactions on Robotics*, 24(2):341–347, 2008.

[90] Dario Floreano and Robert J Wood. Science, technology and the future of small autonomous drones. *Nature*, 521(7553):460–466, 2015.

[91] C Zhang and C Rossi. A review of compliant transmission mechanisms for bio-inspired flapping-wing micro air vehicles. *Bioinspiration & Biomimetics*, 12(2):025005, 2017.

[92] E Farrell Helbling and Robert J Wood. A review of propulsion, power, and control architectures for insect-scale flapping-wing vehicles. *Applied Mechanics Reviews*, 70(1): 010801, 2018.

[93] Michael Karpelson, Gu-Yeon Wei, and Robert J Wood. A review of actuation and power electronics options for flapping-wing robotic insects. *IEEE International Conference on Robotics and Automation*, 779–786, 2008.

[94] Chen Chen and Tianyu Zhang. A review of design and fabrication of the bionic flapping wing micro air vehicles. *Micromachines*, 10(2):144, 2019.

[95] Thorbjörn Ebefors, Johan Ulfstedt Mattsson, Edvard Kälvesten, and Göran Stemme. A walking silicon micro-robot. *Transducers' 99,*, 1202–1205, 1999.

[96] Ken Saito, Minami Takato, Yoshifumi Sekine, and Fumio Uchikoba. Biomimetics micro robot with active hardware neural networks locomotion control and insect-like switching behaviour. *International Journal of Advanced Robotic Systems*, 9(5):226, 2012.

[97] Jiaming Liang, Yichuan Wu, Justin K Yim, Huimin Chen, Zicong Miao, Hanxiao Liu, Ying Liu, Yixin Liu, Dongkai Wang, Wenying Qiu, et al. Electrostatic footpads enable agile insect-scale soft robots with trajectory control. *Science Robotics*, 6(55):eabe7906, 2021.

[98] Kaushik Jayaram, Jennifer Shum, Samantha Castellanos, E Farrell Helbling, and Robert J Wood. Scaling down an insect-size microrobot, HAMR-VI into HAMR-JR. *IEEE International Conference on Robotics and Automation*, 10305–10311, 2020.

[99] Xiufeng Yang, Longlong Chang, and Néstor O Pérez-Arancibia. An 88-milligram insect-scale autonomous crawling robot driven by a catalytic artificial muscle. *Science Robotics*, 5(45):eaba0015, 2020.

[100] Gilles Caprari and Roland Siegwart. Mobile micro-robots ready to use: Alice. *IEEE/RSJ International Conference on Intelligent Robots and Systems*, 3295–3300, 2005.

[101] David L Christensen, Elliot W Hawkes, Srinivasan A Suresh, Karen Ladenheim, and Mark R Cutkosky. μtugs: Enabling microrobots to deliver macro forces with controllable adhesives. *IEEE International Conference on Robotics and Automation*, 4048–4055, 2015.

[102] Palak Bhushan and Claire Tomlin. An insect-scale self-sufficient rolling microrobot. *IEEE Robotics and Automation Letters*, 5(1):167–172, 2019.

[103] Eric Tan Kai Chiang, Takateru Urakubo, and Tomoaki Mashimo. Lift generation by a miniature piezoelectric ultrasonic motor-driven rotary-wing for pico air vehicles. *IEEE Access*, 10:13210–13218, 2022.

[104] Brett Watson, James Friend, and Leslie Yeo. Piezoelectric ultrasonic micro/milli-scale actuators. *Sensors and Actuators A: Physical*, 152(2):219–233, 2009.

[105] Daniel Kuang-Chen Liu, James Friend, and Leslie Yeo. A brief review of actuation at the micro-scale using electrostatics, electromagnetics and piezoelectric ultrasonics. *Acoustical Science and Technology*, 31(2):115–123, 2010.

[106] Tomoaki Mashimo and Shunsuke Izuhara. Recent advances in micromotors. *IEEE Access*, 8:213489–213501, 2020.

[107] Akihiro Iino, Kenji Suzuki, Masao Kasuga, Makoto Suzuki, and Takashi Yamanaka. Development of a self-oscillating ultrasonic micro-motor and its application to a watch. *Ultrasonics*, 38(1-8):54–59, 2000.

[108] Yosuke Nakagawa, Akira Saito, and Takashi Maeno. Nonlinear dynamic analysis of traveling wave-type ultrasonic motors. *IEEE Transactions on Ultrasonics, Ferroelectrics, and Frequency Control*, 55(3):717–725, 2008.

[109] Tomoaki Mashimo, Takateru Urakubo, and Yukiharu Shimizu. Micro geared ultrasonic motor. *IEEE/ASME Transactions on Mechatronics*, 23(2):781–787, 2018.

[110] Daewon Kim, Yun-Sam Kim, Kyoungyong Noh, Misuk Jang, and Seoungrae Kim. Wall-climbing robot with active sealing for radiation safety of nuclear power plants. *Nuclear Science and Engineering*, 194(12):1162–1174, 2020.

[111] Weimin Shen, Jason Gu, and Yanjun Shen. Proposed wall climbing robot with permanent magnetic tracks for inspecting oil tanks. *IEEE International Conference Mechatronics and Automation*, 4:2072–2077, 2005.

[112] Nazim Mir-Nasiri, Hudyjaya Siswoyo, and Md Hazrat Ali. Portable autonomous window cleaning robot. *Procedia Computer Science*, 133:197–204, 2018.

[113] Kathryn A Daltorio, Andrew D Horchler, Stanislav Gorb, Roy E Ritzmann, and Roger D Quinn. A small wall-walking robot with compliant, adhesive feet. *IEEE/RSJ International Conference on Intelligent Robots and Systems*, 3648–3653, 2005.

[114] Benedikt F Seitz, Benjamin Goldberg, Neel Doshi, Onur Ozcan, David L Christensen, Elliot W Hawkes, Mark R Cutkosky, and Robert J Wood. Bio-inspired mechanisms for inclined locomotion in a legged insect-scale robot. *IEEE International Conference on Robotics and Biomimetics*, 791–796, 2014.

[115] Sébastien D de Rivaz, Benjamin Goldberg, Neel Doshi, Kaushik Jayaram, Jack Zhou, and Robert J Wood. Inverted and vertical climbing of a quadrupedal microrobot using electroadhesion. *Science Robotics*, 3(25):eaau3038, 2018.

[116] Michael P Murphy and Metin Sitti. Waalbot: An agile small-scale wall-climbing robot utilizing dry elastomer adhesives. *IEEE/ASME Transactions on Mechatronics*, 12(3): 330–338, 2007.

[117] Kenji Suzuki, Shusuke Nemoto, Takahiro Fukuda, Hideaki Takanobu, and Hirofumi Miura. Insect-inspired wall-climbing robots utilizing surface tension forces. *Journal of Advanced Mechanical Design, Systems, and Manufacturing*, 4(1):383–390, 2010.

[118] Chuanwu Cai, Haifei Zhu, Li Jiang, Yisheng Guan, Xianmin Zhang, and Hong Zhang. A biologically inspired miniature biped climbing robot. *International Conference on Mechatronics and Automation*, 2653–2658, 2009.

[119] Kathryn A Daltorio, Timothy C Witushynsky, Gregory D Wile, Luther R Palmer, Anas Ab Malek, Mohd Rasyid Ahmad, Lori Southard, Stanislav N Gorb, Roy E Ritzmann, and Roger D Quinn. A body joint improves vertical to horizontal transitions of a wall-climbing robot. *International Conference on Mechatronics and Automation*, 3046–3051, 2008.

[120] Giuk Lee, Hwang Kim, Kunchan Seo, Jongwon Kim, and Hong Seok Kim. Multitrack: A multi-linked track robot with suction adhesion for climbing and transition. *Robotics and Autonomous Systems*, 72:207–216, 2015.

[121] TaeWon Seo and Metin Sitti. Tank-like module-based climbing robot using passive compliant joints. *IEEE/ASME Transactions on Mechatronics*, 18(1):397–408, 2012.

[122] J Krahn, Y Liu, A Sadeghi, and C Menon. A tailless timing belt climbing platform utilizing dry adhesives with mushroom caps. *Smart Materials and Structures*, 20(11): 115021, 2011.

[123] Mahmoud Tavakoli, Carlos Viegas, Lino Marques, J Norberto Pires, and AníBal T De Almeida. Omniclimbers: Omni-directional magnetic wheeled climbing robots for inspection of ferromagnetic structures. *Robotics and Autonomous Systems*, 61(9):997–1007, 2013.

[124] Mahmoud Tavakoli and Carlos Viegas. Analysis and application of dual-row omnidirectional wheels for climbing robots. *Mechatronics*, 24(5):436–448, 2014.

[125] Chenfei Yan, Zhenguo Sun, Wenzeng Zhang, and Qiang Chen. Design of novel multi-directional magnetized permanent magnetic adsorption device for wall-climbing robots. *International Journal of Precision Engineering and Manufacturing*, 17:871–878, 2016.

[126] Mahmoud Tavakoli, Joao Lourenco, Carlos Viegas, Pedro Neto, and Anibal T de Almeida. The hybrid omniclimber robot: Wheel based climbing, arm based plane transition, and switchable magnet adhesion. *Mechatronics*, 36:136–146, 2016.

[127] Markus Eich and Thomas Vögele. Design and control of a lightweight magnetic climbing robot for vessel inspection. *19th Mediterranean Conference on Control & Automation*, 1200–1205, 2011.

[128] Haruhiko Eto and H Harry Asada. Development of a wheeled wall-climbing robot with a shape-adaptive magnetic adhesion mechanism. *IEEE International Conference on Robotics and Automation*, 9329–9335, 2020.

[129] Zhiqiang Bi, Yisheng Guan, Shizhong Chen, Haifei Zhu, and Hong Zhang. A miniature biped wall-climbing robot for inspection of magnetic metal surfaces. *IEEE International Conference on Robotics and Biomimetics*, 324–329, 2012.

[130] Francisco Ochoa-Cardenas and Tony J Dodd. Design of an active magnetic wheel with a varying electro-permanent magnet adhesion mechanism. *IEEE/RSJ International Conference on Intelligent Robots and Systems*, 3340–3345, 2015.

[131] Dingxin Ge, Yongchen Tang, Shugen Ma, Takahiro Matsuno, and Chao Ren. A pressing attachment approach for a wall-climbing robot utilizing passive suction cups. *Robotics*, 9(2):26, 2020.

[132] TC Apostolescu, C Udrea, D Duminica, G Ionascu, L Bogatu, Laurenţiu Adrian Cartal, et al. Development of a climbing robot with vacuum attachment cups. *International Conference On Innovations, Recent Trends And Challenges In Mechatronics, Mechanical Engineering And New High-Tech Products Development, MECAHITECH' 11*, 3258–267, 2011.

[133] Yu Yoshida and Shugen Ma. Design of a wall-climbing robot with passive suction cups. *IEEE International Conference on Robotics and Biomimetics*, 1513–1518, 2010.

[134] Ayato Kanada, Fabio Giardina, Toby Howison, Tomoaki Mashimo, and Fumiya Iida. Reachability improvement of a climbing robot based on large deformations induced by tri-tube soft actuators. *Soft Robotics*, 6(4):483–494, 2019.

[135] Jinfu Liu, Linsen Xu, Shouqi Chen, Hong Xu, Gaoxin Cheng, and Jiajun Xu. Development of a bio-inspired wall-climbing robot composed of spine wheels, adhesive belts and eddy suction cup. *Robotica*, 39(1):3–22, 2021.

[136] Ravindra Singh Bisht, Pushparaj Mani Pathak, and Soraj Kumar Panigrahi. Design and development of a glass façade cleaning robot. *Mechanism and Machine Theory*, 168: 104585, 2022.

[137] Peng Liang, Xueshan Gao, Qingfang Zhang, Mingkang Li, Rui Gao, and Yuxin Xu. Analysis and experimental research on motion stability of wall-climbing robot with double propellers. *Advances in Mechanical Engineering*, 13(9):1–13, 2021.

[138] Aihong Ji, Zhihui Zhao, Poramate Manoonpong, Wei Wang, Guangming Chen, and Zhendong Dai. A bio-inspired climbing robot with flexible pads and claws. *Journal of Bionic Engineering*, 15(2):368–378, 2018.

[139] Sangbae Kim, Alan T Asbeck, Mark R Cutkosky, and William R Provancher. SPINYBOTII: Climbing hard walls with compliant microspines. *International Conference on Advanced Robotics*, 601–606, 2005.

[140] Mahmoud Tavakoli, Ali Marjovi, Lino Marques, and Anibal T de Almeida. 3DCLIMBER: A climbing robot for inspection of 3d human made structures. *IEEE/RSJ International Conference on Intelligent Robots and Systems*, 4130–4135, 2008.

[141] Aaron Parness, Mathew Frost, Nitish Thatte, Jonathan P King, Kevin Witkoe, Moises Nevarez, Michael Garrett, Hrand Aghazarian, and Brett Kennedy. Gravity-independent rock-climbing robot and a sample acquisition tool with microspine grippers. *Journal of Field Robotics*, 30(6):897–915, 2013.

[142] Kalind Carpenter, Nick Wiltsie, and Aaron Parness. Rotary microspine rough surface mobility. *IEEE/ASME Transactions on Mechatronics*, 21(5):2378–2390, 2015.

[143] Kisuke Nonoyama, Masahiro Shimizu, and Takuya Umedachi. Upside-down brachiation robot using elastic energy stored through soft body deformation. *IEEE Robotics and Automation Letters*, 7(4):11291–11297, 2022.

[144] Rui Chen, Rong Liu, Jifan Chen, and Jin Zhang. A gecko inspired wall-climbing robot based on electrostatic adhesion mechanism. *IEEE International Conference on Robotics and Biomimetics*, 396–401, 2013.

[145] Harsha Prahlad, Ron Pelrine, Scott Stanford, John Marlow, and Roy Kornbluh. Electroadhesive robots—wall climbing robots enabled by a novel, robust, and electrically controllable adhesion technology. *IEEE International Conference on Robotics and Automation*, 3028–3033, 2008.

[146] Rodolfo Ruibal and Valerie Ernst. The structure of the digital setae of lizards. *Journal of Morphology*, 117(3):271–293, 1965.

[147] Kellar Autumn, Yiching A Liang, S Tonia Hsieh, Wolfgang Zesch, Wai Pang Chan, Thomas W Kenny, Ronald Fearing, and Robert J Full. Adhesive force of a single gecko foot-hair. *Nature*, 405(6787):681–685, 2000.

[148] Burak Aksak, Michael P Murphy, and Metin Sitti. Gecko inspired micro-fibrillar adhesives for wall climbing robots on micro/nanoscale rough surfaces. *IEEE International Conference on Robotics and Automation*, 3058–3063, 2008.

[149] Hemant Kumar Raut, Avinash Baji, Hassan Hussein Hariri, Hashina Parveen, Gim Song Soh, Hong Yee Low, and Kristin L Wood. Gecko-inspired dry adhesive based on micro–nanoscale hierarchical arrays for application in climbing devices. *ACS Applied Materials & Interfaces*, 10(1):1288–1296, 2018.

[150] Sangbae Kim, Matthew Spenko, Salomon Trujillo, Barrett Heyneman, Virgilio Mattoli, and Mark R Cutkosky. Whole body adhesion: Hierarchical, directional and distributed control of adhesive forces for a climbing robot. *IEEE International Conference on Robotics and Automation*, 1268–1273, 2007.

[151] Walter Federle, Werner Baumgartner, and Bert Holldobler. Biomechanics of ant adhesive pads: Frictional forces are rate-and temperature-dependent. *Journal of Experimental Biology*, 207(1):67–74, 2004.

[152] Tohru Miyake, Hidenori Ishihara, and Motoi Yoshimura. Basic studies on wet adhesion system for wall climbing robots. *International Conference on Intelligent Robots and Systems*, 1920–1925, 2007.

[153] Bin He, Zhipeng Wang, Minghe Li, Kun Wang, Runjie Shen, and Sanqing Hu. Wet adhesion inspired bionic climbing robot. *IEEE/ASME Transactions on Mechatronics*, 19 (1):312–320, 2013.

[154] Xi Liu, Lianxin Shi, Xizi Wan, Bing Dai, Man Yang, Zhen Gu, Xinghua Shi, Lei Jiang, and Shutao Wang. A spider-silk-inspired wet adhesive with supercold tolerance. *Advanced Materials*, 33(14):2007301, 2021.

[155] Ying-Chu Chen and Hongta Yang. Octopus-inspired assembly of nanosucker arrays for dry/wet adhesion. *ACS Nano*, 11(6):5332–5338, 2017.

[156] Nicholas Wiltsie, Michele Lanzetta, and Karl Iagnemma. A controllably adhesive climbing robot using magnetorheological fluid. *International Conference on Technologies for Practical Robot Applications*, 91–96, 2012.

[157] Yufeng Chen, Neel Doshi, and Robert J Wood. Inverted and inclined climbing using capillary adhesion in a quadrupedal insect-scale robot. *IEEE Robotics and Automation Letters*, 5(3):4820–4827, 2020.

[158] Aaron Parness, Daniel Soto, Noé Esparza, Nick Gravish, Matt Wilkinson, Kellar Autumn, and Mark Cutkosky. A microfabricated wedge-shaped adhesive array displaying gecko-like dynamic adhesion, directionality and long lifetime. *Journal of the Royal Society Interface*, 6(41):1223–1232, 2009.

[159] Michael Varenberg and S Gorb. Shearing of fibrillar adhesive microstructure: Friction and shear-related changes in pull-off force. *Journal of The Royal Society Interface*, 4 (15):721–725, 2007.

[160] William R Provancher, Samuel I Jensen-Segal, and Mark A Fehlberg. ROCR: An energy-efficient dynamic wall-climbing robot. *IEEE/ASME Transactions on Mechatronics*, 16 (5):897–906, 2010.

[161] Keng Huat Koh, RM Kuppan Chetty, and SG Ponnambalam. Modeling and simulation of electrostatic adhesion for wall climbing robot. *IEEE International Conference on Robotics and Biomimetics*, 2031–2036, 2011.

[162] Ausama Hadi Ahmed and Carlo Menon. On the static structural design of climbing robots: Part 1. *Robotics and Biomimetics*, 2(1):1–11, 2015.

[163] Rudolf Yoga Hutama, Mohamed M Khalil, and Tomoaki Mashimo. A millimeter-scale rolling microrobot driven by a micro-geared ultrasonic motor. *IEEE Robotics and Automation Letters*, 6(4):8158–8164, 2021.

[164] Matthias Greuter, Gaurav Shah, Gilles Caprari, Fabien Tâche, Roland Siegwart, and Metin Sitti. Toward micro wall-climbing robots using biomimetic fibrillar adhesives. *International Symposium on Autonomous Minirobots for Research and Edutainment*, 39–46, 2006.

[165] William A Breckwoldt, Kathryn A Daltorio, Lars Heepe, Andrew D Horchler, Stanislav N Gorb, and Roger D Quinn. Walking inverted on ceilings with wheel-legs and micro-structured adhesives. *IEEE/RSJ International Conference on Intelligent Robots and Systems*, 3308–3313, 2015.

List of Publications

The content of this thesis is based on four peer-reviewed publications. The content of the publications has been edited and extended to match this thesis.

Journals (peer-reviewed):

1. **Mohamed M. Khalil**, Naoya Masuda, Kotaro Takayama, and Tomoaki Mashimo, “A Closed-Loop Micro-Ultrasonic Motor Control System With Extremum Seeking,” IEEE Access, vol. 11, pp. 22329-22341, March 2023.

2. **Mohamed M. Khalil** and Tomoaki Mashimo, “Caterpillar-Inspired Insect-Scale Climbing Robot Using Dry Adhesives,” IEEE Robotics and Automation Letters (RA-L), vol. 7, no. 3, pp. 7628-7635, July 2022.
(This paper was also selected for presentation at the 2022 IEEE/RSJ International Conference on Intelligent Robots and Systems (IROS), Kyoto, Japan, 23-27 October, 2022)

3. Rudolf Yoga Hutama, **Mohamed M. Khalil**, and Tomoaki Mashimo, “A Millimeter-Scale Rolling Microrobot Driven by a Micro-Geared Ultrasonic Motor,” IEEE Robotics and Automation Letters (RA-L), vol. 6, no. 4, pp. 8158-8164, October 2021.

International Conferences (peer-reviewed):

1. **Mohamed M. Khalil**, Naoya Masuda, Kotaro Takayama, and Tomoaki Mashimo, “A Small In-Pipe Inspection Robot with Integrated Holding Force Mechanism,” 7th International Conference on Robotics and Automation Engineering (ICRAE), Singapore, pp. 247-253, November 2022.

Achievements

Awards

1. **October, 2022**: IEEE Robotics and Automation Society Japan Joint Chapter Young Award (IROS, CASE)